Doctoral Thesis

Water properties in confined geometry

a combined scattering study using X-rays, neutrons, and light

Dipl.-Phys. Maxim Erko

March 2012

Montanuniversität Leoben
Institute of Physics

Supervisor
Univ. Prof. Dr. Oskar Paris

Second Referee
ao. Univ. Prof. Dr. Julian Stangl

Date of the graduation:
April 24th 2012

«Das Prinzip aller Dinge ist das Wasser: aus Wasser ist alles und ins Wasser kehrt alles zurück.»

Thales von Milet (griechischer Naturphilosoph, Mathematiker) in Goethes Faust

Contents

Abstract

The present thesis presents a systematic study of the influence of confinement on structural properties of water at low temperatures. Mesoporous silica materials with cylindrical pores on a two-dimensional hexagonal lattice (MCM-41 and SBA-15) represent ideal model systems for analysing the phase behaviour of water in nano-confinement. Using materials with seven different pore sizes ranging between 2 - 9 nm, the low-temperature behaviour of confined water was studied by means of X-ray, neutron, and Raman scattering. The obtained results show that water confined in silica mesopores represents an exceedingly complex system. The data suggest a non-homogeneous water occupancy of the available confinement volume. At least two spatially separated water phases exist in hydrophilic mesopores, i.e. a non-freezable wall layer, and a structurally different water phase in the core of the pores. The development of a distinct tetrahedral hydrogen-bonded water network upon cooling was found only in the core part of the pores. This effect was found to result in significantly different water density values attributed to the respective phase. Moreover, the inner part of confined water was shown to undergo considerable structural changes with decreasing pore size. Additional cooling and heating measurements revealed that the liquid-solid phase transition of the inner water is accompanied by a density minimum situated at the freezing/melting temperature which depends on confinement dimensions. This density minimum was interpreted as the crossover between the anomalous density behaviour for liquid water and the normal density change with temperature for ice. The observed temperature-induced mesopore lattice deformation was described by a novel approach, introducing the negative Laplace pressure as the pressure difference between the liquid and the solid phase.

The influence of water on the mesoporous structure of the used materials was analysed within the first application of a newly developed laboratory apparatus allowing long-term *in situ* phase transition studies by means of small-angle X-ray scattering. This study revealed distinct silica matrix modification of SBA-15 material upon repeated water sorption. The obtained data suggest that pore lattice deformation occurring during water capillary condensation and evaporation irreversibly changes the silica matrix by partially enclosing water within collapsed pore regions.

Zusammenfassung

Die vorliegende Dissertation ist eine systematische Darstellung der Einflüsse der geometrischen Begrenzung auf die strukturellen Eigenschaften von Wasser bei tiefen Temperaturen. Die bei den Untersuchungen verwendeten mesoporösen Silika-Materialien MCM-41 und SBA-15 sind durch eine periodische Anordnung von zylindrischen Poren auf einem zwei-dimensionalen hexagonalem Gitter gekennzeichnet. Diese Materialien stellen ideale Modelle zur Analyse des Phasenverhaltens von Wasser in Nano-Geometrie dar. Eingeschlossen in sieben verschieden Porengrößen zwischen 2 - 9 nm wurde das Tieftemperaturverhalten von Wasser mittels Streuung von Röntgenstrahlung, Neutronen und Licht (Raman-Streuung) untersucht. Die außerordentliche Komplexität des untersuchten Systems zeigte sich vor allem durch die inhomogene Verteilung von Wassermolekülen innerhalb des Porenvolumens. Es konnte gezeigt werden, dass in hydrophilen Mesoporen mindestens zwei räumlich abgegrenzte Wasserphasen existieren. Dabei zeigt die nicht frierende Wasserschicht an der Porenwand deutliche strukturelle Unterschiede zum restlichen Wasser in der Porenmitte auf. Beim Abkühlen ist der Aufbau einer tetraedrischen Bindungsstruktur aus Wasserstoffbrücken nur für den Wasseranteil in der Porenmitte zu beobachten. Es konnte gezeigt werden, dass dieser Effekt zu deutlich unterschiedlichen Werten für die Dichte für die jeweilige Wasserphase führt. Darüber hinaus konnte ein systematischer Zusammenhang zwischen der Porengröße und der Struktur des Wassers in der Porenmitte gezeigt werden. Die temperaturbedingte Dichteänderung des Porenwassers ist durch Minimalwerte genau an den Frier- und Schmelztemperaturen gekennzeichnet, welche wiederum von der gewählten Porengröße abhängen. Diese Eigenschaft wird durch den Übergang zwischen dem anomalen Temperaturverhalten der Dichte für das flüssige Wasser und dem normalen für das Eis interpretiert. Die temperaturbedingte Porengitterverzerrung wurde durch einen neuen Ansatz beschrieben. Dieser beinhaltet die Einführung des negativen Laplace-Drucks als die Druckdifferenz zwischen der flüssigen und der festen Phase in teilweise gefrorenen Mesoporen.

Der Einfluss von Wasser auf die mesoporöse Struktur der benutzten Materialien wurde mit Hilfe eines neu entwickelten Laborinstruments untersucht. Diese Apparatur erlaubt *in situ* Langzeit-Untersuchungen von Phasenübergängen mittels Röntgen-Kleinwinkelstreuung. Im Laufe wiederholter Sorptionszyklen von Wasser in SBA-15 wurden deutliche Veränderungen des porösen Materials offenbart. Anhand der Streudaten konnte die irreversible Modifikation der Porenmatrix durch die Veränderung der Porenoberfläche, sowie durch das Zurückbleiben von Wasser in teilweise kollabierten Porenbereichen erklärt werden.

1 Motivation

Studies of liquid water are essential for numerous scientific fields aiming at the understanding of the fundamentals of life. The unique structural behaviour of water is regarded to be even more pronounced upon strong supercooling. A number of recent computer simulation studies of liquid water suggest the existence of a liquid–liquid phase transition between a low-density and a high-density water phase. Unfortunately, homogeneous nucleation of ice prevents experimental studies of bulk liquid water at temperatures below 235 K. Thus, no direct validation of this phenomenon within the inaccessible temperature region, the so-called ‘‘no man’s land’’, are possible. Confining water into very narrow pores was shown to considerably extend the temperature region for liquid water towards lower temperatures. The presence of hydrophilic pore walls was shown to strongly modify the thermodynamic properties of water, such as the condensation pressure, and the melting temperature. Thus, confining water into nanopores is regarded as a ‘‘trick’’ to experimentally assess bulk water properties within the inaccessible low-temperature region.

The aim of this thesis is to investigate the influence of confinement on the structure and the density of water at low-temperatures. To this end, following experimental approaches were performed:

- the bonding structure of water molecules confined in nanopores with diameters ranging between 2 - 9 nm was studied as a function of temperature using the inelastic scattering of light (Raman scattering)
- the corresponding water density values were extracted from additional small-angle scattering experiments performed with X-rays (SAXS) and neutrons (SANS)
- these small-angle experiments were corroborated by measurements of the water ordering structure from independent wide-angle X-ray scattering experiment (WAXS)
- beyond this, the reverse question about the influence of water on the structure of the confining matrix was studied by the analysis of repeated water sorption in SBA-15 material using a newly developed apparatus, which allows *in situ* phase transition studies by means of SAXS

The theoretical background of the fundamental concepts which are important for the thesis is presented in chapter 2. An introduction of the basic water properties is given in section 2.1. This general description of water is accompanied by the literature background summarising the current state of research in the fields of glassy, supercooled, and confined water. A basic thermodynamic description of phase transitions, introducing the concept of fluid sorption is provided in section 2.2. The porous materials MCM-41 and SBA-15, which were used as confining matrices are introduced in section 2.3. Fundamental concepts of the scattering theory, including the elastic scattering of X-rays and neutrons, and the inelastic scattering of light (Raman scattering) are given in section 2.4.

Chapter 3 presents details about the experimental conditions of the measurements performed within this thesis. The setup conditions of the scattering experiments are presented in section 3.1 (Raman scattering), and in section 3.2 (SAXS, SANS, and WAXS). Section 3.3 describes the experimental setup for the study of repeated water sorption in SBA-15. This section also includes a detailed presentation of the newly developed apparatus for *in situ* SAXS studies of phase transitions in confinement.

Results from all experiments performed within this thesis are presented and discussed in chapter 4. The Raman scattering study of the binding structure of confined water at different temperatures is presented and discussed in section 4.1. The temperature behaviour of the density of confined water, obtained from the combined data analysis of the performed SAXS, SANS, and WAXS experiments is presented and discussed in section 4.2. Analysis of the observed temperature-induced pore lattice deformation is presented and discussed in section 4.3. Results from the study of repeated water sorption in SBA-15 are presented and discussed in section 4.4.

Chapter 5 contains a general summary and discussion of the obtained results, including further suggestions of possible expansion of the performed studies.

2 Fundamentals

2.1 Water

The important role of water for life on Earth is apparent. It is involved in all components of the climate system, including the atmosphere, the hydrosphere, the cryosphere, the land surface and the biosphere [Bates, 2008]. The majority of water is located in oceans (97.3 %). The remaining water is located in glaciers (2.1 %), ground water (0.6 %), and lakes and rivers (below 0.01%) [EET, 2012]. In general, for the development of a living organism, a liquid medium is needed in order to enable transport of molecules which are necessary for its existence [Impey, 2011]. For life on Earth, this liquid medium is water, it dissolves a wide variety of materials and simultaneously assists molecular transport within the cells. Water can also act as a protection shield against harmful ultraviolet (UV) radiation. In the history of early Earth the first forms of life are regarded to have developed in deep water [Impey, 2011]. The key role of water in human history is visible along the entire time line including Egyptian, Greek, Roman, Chinese and other cultures. The understanding of the unique properties of water has played a central role in science since millenia [Franks, 2000]. Going back to Plato's and Aristotle's classical four element theory, water has long time been regarded as a single element, even after earth, fire and air had been recognised for what they actually were. Water science has always been interdisciplinary. Its influence on developments in numerous scientific fields is immense. In this way, water properties often constituted significant defining parameters in history of new discoveries, such as in studies of optical science by Roger Bacon, or in development of hydrostatics and fluid dynamics by Blaise Pascal and later by Leonhard Euler, or in understanding of tides by Galileo Galilei and Johannes Kepler, only mentioning some of them. A contemporary scientific point of view about water properties can be found in Leonardo da Vinci's "Del moto e misura dell'acqua". The image of water as a single element remained unchanged until the end of the 18^{th} century, when Antoine de Lavoisier and Joseph Priestley demonstrated water to be a "mixture" of elements.

2.1.1 General properties

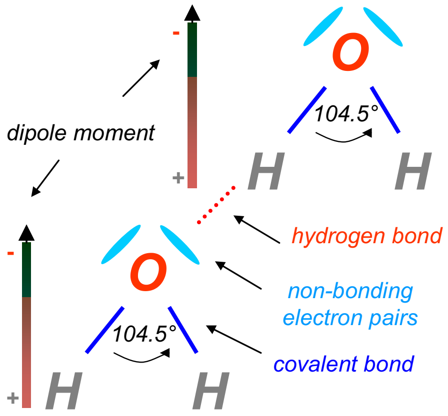

Figure 2.1: Hydrogen-bonded water molecules.

The key-role of water in shaping our living environment is based on its unique physical properties together with its essential influence in the course of chemical reactions. Although water is one of the most “common” substance in our daily life, many of its properties are still regarded as unusual and counterintuitive. For instance, liquid water expands if it is sufficiently cold and becomes more compressible with further cooling, and it gets less viscous by compression. There are more than 14 different forms of crystalline ice which have been identified so far [Petrenko & Whitworth, 1999]. At least nine of those are stable over some range of temperature and pressure and other forms are metastable [Debenedetti & Stanley, 2003].

In a water molecule the central oxygen atom is covalently bound to each of the two hydrogen atoms by a shared pair of electrons (see Figure 2.1). However, only two of the six outer-shell electrons of oxygen are used for the covalent bonds, leaving two non-bonding electron pairs. In order to minimise the repulsion, the two negative charged electron clouds together with the hydrogen atom arrange themselves in a tetrahedral geometry with the oxygen atom in the centre (Figure 2.2). The angle resulting from a tetrahedral structure is 109.5°. However, for H_2O the two non-bonding electron pairs exert a stronger repulsion against the bonding ones, thus the two hydrogen atoms are closer together. This leads to the distorted tetrahedral bond angle of 104.5° which is characteristic for a water molecule. Although a water molecule is electrically neutral, the charge distribution is not uniform. The negative charge of the oxygen atom on the one side and the positive of the two hydrogen atoms on the other, generate an electric dipole moment.

A partially positive hydrogen atom of the one water molecule is electrostatically attracted to the partially negative oxygen atom of a neighbouring water molecule, resulting in a so-called *hydrogen bond* (HB) (see Figure 2.1). The development of large hydrogen bonded clusters into stable networks is responsible for some of the anomalous characteristics of water at low temperatures. Remarkably, water is one of the few known condensed matter systems whose solid form is less dense than the liquid. The volume change of water in the temperature range between 200 - 320 K is shown in Figure 2.3. The large density decrease of about 9 % on freezing explains why ice floats on water and why water-filled bottles burst when they freeze. Ordinary hexagonal ice is characterised by fully developed tetrahedral HB network lattice which implies larger atomic distances than for liquid water (see Figure 2.4).

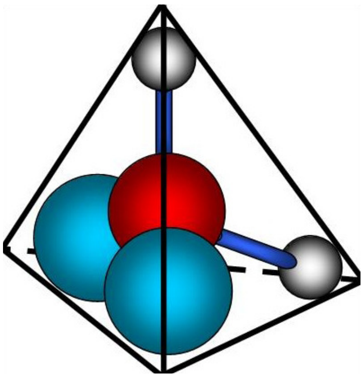

Figure 2.2: Tetrahedral structure of a water molecule. White spheres indicate the hydrogen atoms, red sphere is the oxygen atom. Nonbonding electron clouds are shown in cyan.

At atmospheric pressure, the hexagonal ice is stable between 72 and 273 K [Debenedetti, 1996]. However, water can also be found in its liquid phase inside the crystalline domain of stability. Liquid water in this metastable state is called *supercooled*. Particularly, in this temperature region the unusual behaviour of water becomes most pronounced. Even minor perturbations of this labile equilibrium trigger the sudden transition into the stable crystalline phase. Dissolved and suspended impurities or mechanical perturbations can lead to the spontaneous water freezing. At ambient pressure, and without assistance of impurities or surfaces the limit of water supercooling, the so-called temperature of *homogeneous ice nucleation*, is around $T_h \approx 231$ K (see subsection 2.2.3). Once frozen, the heating process of ice does not exhibit any metastability in this temperature region, thus at ambient pressure the melting point of ice is a well-defined parameter and is situated at $T_m = 273.16$ K. For higher temperatures, liquid water density first increases due to further distortion of the HB structure and reaches a maximum at 4° C at ambient pressure (TDM - temperature of density maximum). For temperatures above TDM the thermal expansion predominates and the “normal” density change with temperature is observed.

2.1.2 Water polyamorphism

If water is cooled fast enough (cooling rates around 10^6 K/s), crystallisation can be avoided, and water then becomes an amorphous solid - a glass. Glassy water is thought to be the most spread water form in the universe [Debenedetti & Stanley, 2003]. It is observed as a frost on interstellar dust, constitutes the bulk of matter in comets, and is thought to play an important role in the phenomena associated with planetary activity [Jenniskens & Blake, 1994]. Although glassy water is a solid, its structure exhibits a disordered liquid-like arrangement [Mishima & Stanley, 1998]. Three forms of amorphous solid water have been described so far. The existence of low-density amorphous ice (LDA) was reported 75 years ago for the first time by Burton and Oliver [Burton & Oliver, 1936]. Almost 50 years later a second kind of amorphous ice, high-density amorphous ice (HDA) with ~ 25% higher density was discovered [Mishima, 1984, Heide, 1984]. A pressure-induced fist-order transition between these two glassy water states was suggested one year later [Mishima, 1985]. The nature and type of this transition is however questioned by several scientific groups until today [Tse, 1992, Sastry, 1996, Angell, 2008]. The LDA-HDA transition includes a rapid water compression up to several kbar

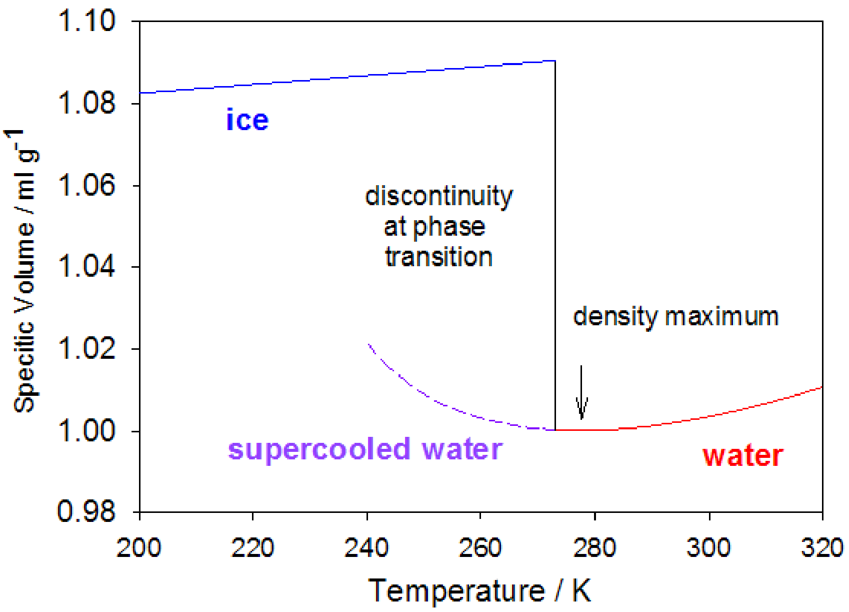

Figure 2.3: Water specific volume change with temperature. Data taken from [Landolt & Boernstein, 1977, Hare & Sorensen, 1987].

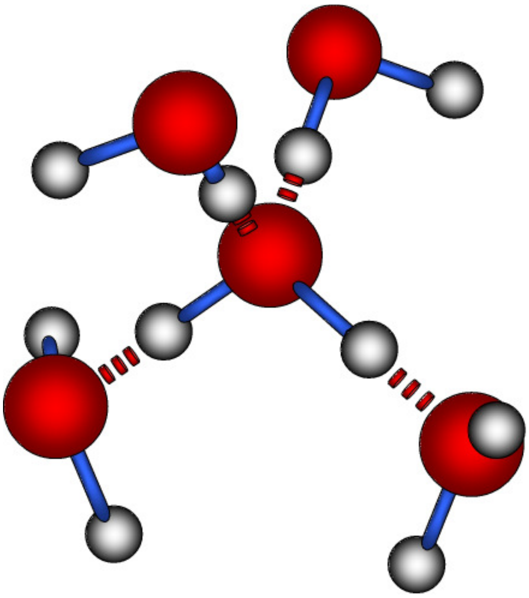

Figure 2.4: Five-molecule HB structure of water. Bond types are indicated in Figure 2.1. Figure adapted from [Walrafen, 1964].

at temperatures around 130 - 140 K [Mishima, 1994]. Recently, very-high-density amorphous ice (VHDA) has been proposed as a third, distinct form of glassy water [Loerting, 2001, Finney, 2002]. This multiplicity of different glassy water states constitutes the so-called *polyamorphism* of water [Poole, 1995]. It implies different structures and different bulk properties, such as the density for the tree glassy water states. Figure 2.5 shows routes for the formation of LDA, HDA and VHDA, respectively.

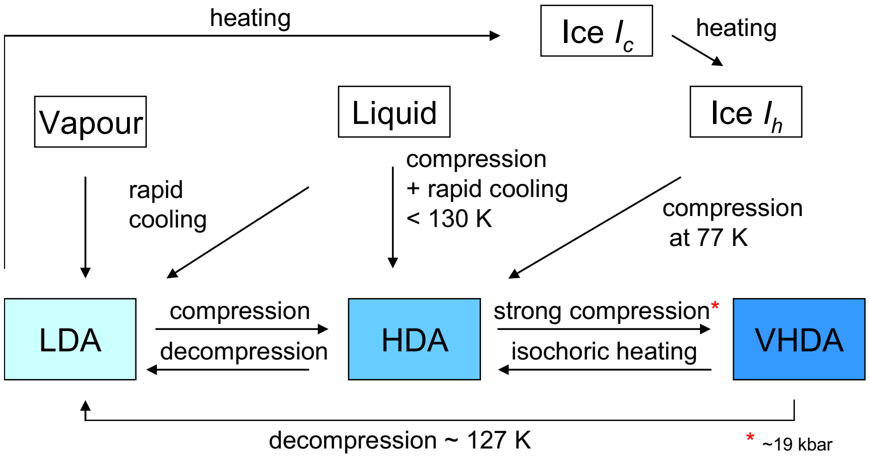

Figure 2.5: Formation of low-density (LDA), high-density (HDA) and very-high-density (VHDA) amorphous ice. Cubic and hexagonal ice are denoted as I_c and I_h, respectively. Figure adapted from [Debenedetti & Stanley, 2003].

The exact value for the water glass transition temperature T_g is difficult to determine experimentally. Only indirect extrapolation of the measured parameters, such as the heat capacity c_p obtained either at very low or at very high temperatures, gives hints about the water glass transition temperature. Thermodynamic parameters like the thermal expansion coefficient $(\partial V/\partial T)_p$ or the isobaric heat capacity $(\partial H/\partial T)_p$ change abruptly but continuously at T_g. Defining a glass transition from dynamic measurements implies an extrapolation of the characteristic molecular relaxation time to the value of 100 s [Debenedetti & Stillinger, 2001]. For water the commonly accepted value at ambient pressure is $T_g = 136$ K [Debenedetti & Stanley, 2003]. The working group around Angell observed in the course of heating of LDA the beginning of the thermal relaxation at sufficiently higher T/T_g values compared to other glass-forming liquids [Velikov, 2001]. Angell and co-workers argue $T_g = 165$ K to be the true value. This reassignment is controversial. Spontaneous crystallization of LDA into cubic ice I_c is found to occur around 150 K [Debenedetti & Stanley, 2003]. A number of different experimental parameters, such as sample preparation or the experimental heating rate, seem to have considerable influence on the reported results [Angell, 2008]. This phenomenon is visualised in Figure 2.6. At a slow heating rate the glass transition is observed at a lower temperature than for faster heating rates. Thus, alternative values for the transformation from LDA to crystalline cubic ice have been reported so far, ranging between 132 K and 160 K [Handa & Klug, 1988, Angell, 2002, Kohl, 2005].

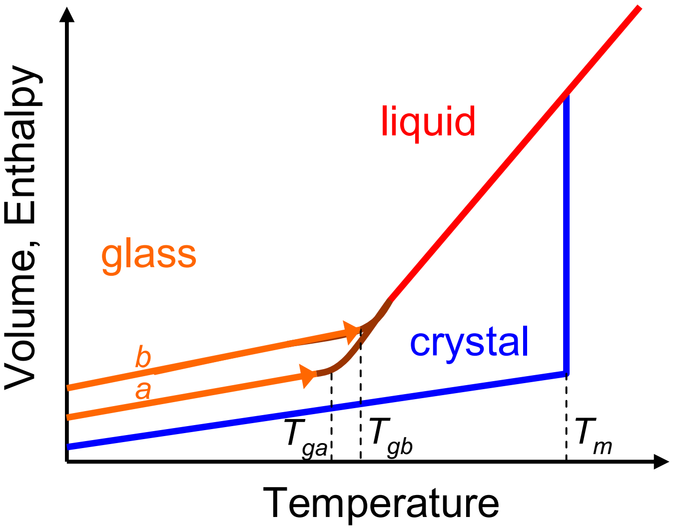

Figure 2.6: Temperature dependence of the volume or enthalpy of a (normal) liquid at constant pressure. T_m is the melting temperature. Paths of slow and fast heating rates are denoted by a and b, respectively. The corresponding glass transition temperatures are T_{ga} and T_{gb}. Figure adapted from [Debenedetti & Stillinger, 2001].

These experiments illustrate that the exact temperature behaviour of water around the temperatures of the glass transition T_g and around the temperature of homogeneous nucleation T_h is difficult to probe experimentally. However, experimental results reported on water around T_g and T_h suggest singular behaviour of thermodynamic parameters, such as heat capacity in Figure 2.7. Moreover, there is a gap between T_g and T_h, the so-called "*no man's land*" [Debenedetti & Stanley, 2003], where no direct data on bulk liquid water are available.

2.1.3 Supercooled water

Within the last two decades, a new scientific topic has found remarkable interest within the worldwide water research community. In case that water would not form an open tetrahedral HB network, as in crystalline ice, the development of liquid water properties in the supercooled regime would significantly change [Angell, 2008]. The knowledge of how water behaves inside the no man's land may give a better understanding of the fundamental driving mechanisms for water outside of this region [Soper, 2008]. Thus, entering the no man's land has become a "challenge" [Angell, 2008].

The general motivation implies the search of a coherent explanation for the following experimentally observed phenomena [Debenedetti & Stanley, 2003]:

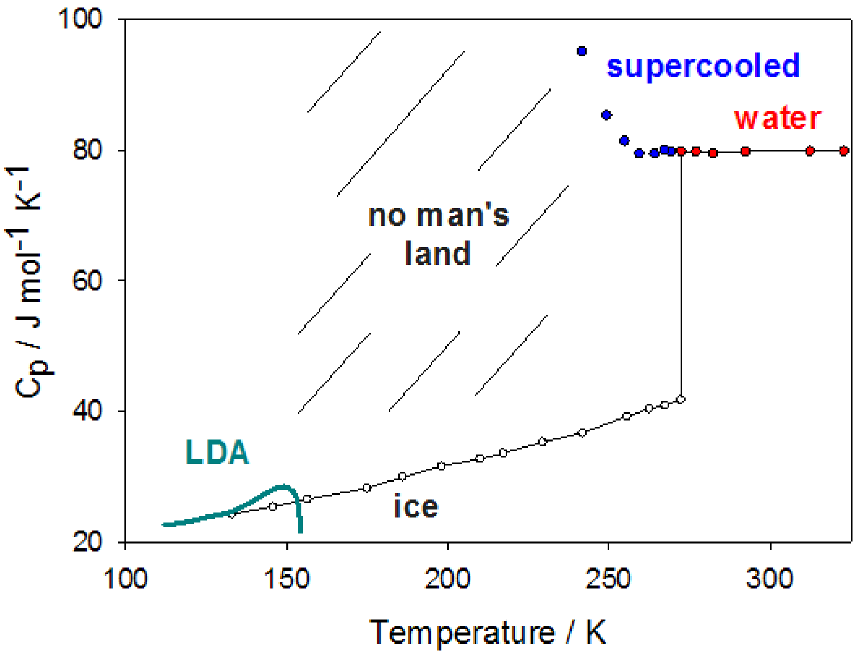

Figure 2.7: Experimental heat capacity data of water in four different states. Data taken from [Angell, 1982, Handa & Klug, 1988, Hofer, 1991, Tombari, 1999, Kohl, 2005].

- the sharp increase in isothermal compressibility, the thermal expansion coefficient and the isobaric heat capacity upon supercooling (see Figure 2.7)
- the nature of transition between LDA and HDA
- the relationship between a number of similar properties of supercooled and glassy water

The unusual behaviour of bulk water has already been described by many “classic explanations” [Bernal & Fowler, 1933, Lennard-Jones & Pople, 1951, Eisenberg & Kauzmann, 1969], including a simple two-state model dating back to Röntgen [Roentgen, 1892]. Since direct measurements inside the no man’s land are largely not feasible, only the application of thermodynamic principles on data measured on both edges of the gap is possible [Starr, 2003]. Four hypotheses are under current discussion [Mishima & Stanley, 1998, Stanley, 2009, Stanley, 2011]:

1. The *stability limit hypothesis*: A continuous stability limit line $p_s(T)$ within the pressure-temperature phase diagram is defined by the thermodynamic condition $(\partial p/\partial V) \rightarrow 0$ as $p \rightarrow p_s(T)$. Starting from the critical point at high temperatures it bounds the superheated, stretched, and supercooled states. The response functions (response of density ρ or entropy S to change in temperature T or pressure p) diverge approaching the line of stability. Particularly, the shape of the $p_s(T)$ line is responsible for the thermodynamic anomalies of

water. For more detailed information about the stability limit hypothesis see Ref. [Speedy, 1982].

2. The *singularity-free hypothesis* considers the possibility that the observed poly-amorphic water transitions are essentially relaxation phenomena resembling a genuine first-order transition. Thus, the observed rapid rise of response functions does not compulsory imply a singularity behaviour. In terms of the *percolation theory* water is described as a locally structured transient gel with water molecules forming the continuous phase linked by the HB network [Stanley & Teixeira, 1980]. The number of HBs increase with decreasing temperature locally forming “patches” or bonded subdomains [Geiger & Stanley, 1982], and thus leading to enhanced fluctuations of specific volume and entropy. The detailed description of this hypothesis is given in Ref. [Sastry, 1996].
3. The *liquid-liquid phase transition hypothesis* is based on molecular dynamics (MD) studies of water structure and of the equation of state of supercooled water [Poole, 1992]. This hypothesis presumes a first-order phase transition between LDA and HDA. These two vitreous water forms are claimed to be the low-temperature expressions of two different phases of liquid water, i.e. low-density liquid (LDL) and high-density liquid (HDL). The two water phases are separated by a phase transition line ending in a *second critical point* (see Figure 2.8). Similar to the situation near the known high-temperature critical point (see subsection 2.2.1), bulk water near the liquid-liquid critical point is described as a fluctuating mixture of the two different local structure phases. While in the former case the two structures resemble the liquid and gas phases, in the latter one the local water structures correspond to those of LDL and HDL. The two particular phases are indistinguishable beyond the corresponding critical point which is located around 1.4 kbar and 200 K in the water phase diagram [Poole, 1992]. The dramatic increase in response functions observed in supercooled bulk water is described in terms of critical fluctuation arising beyond the second critical point [Debenedetti & Stanley, 2003].
4. The *critical-point free* hypothesis proposes an order-disorder transition, similar to what happens in crystalline C_{60}, with the possibility of a weak first-order transition character between the two liquid water phases [Angell, 2008]. Similar to the first hypothesis, this scenario effectively predicts a continuous locus of stability limit. It does not exclude the possible existence of second critical point, but it does not require it. How this most recent suggestion relates to the full phase diagram of water remains to be determined [Soper, 2008].

The four scenarios predict fundamentally different water behaviour, although each of them has been rationalised as a consequence of the same microscopic interaction, namely the HB network [Stanley, 2011].

Particularly, the third hypothesis obtained considerable support from the expanding computer simulation community [Ponyatovskii, 1994, Poole, 1994, Borick, 1995,

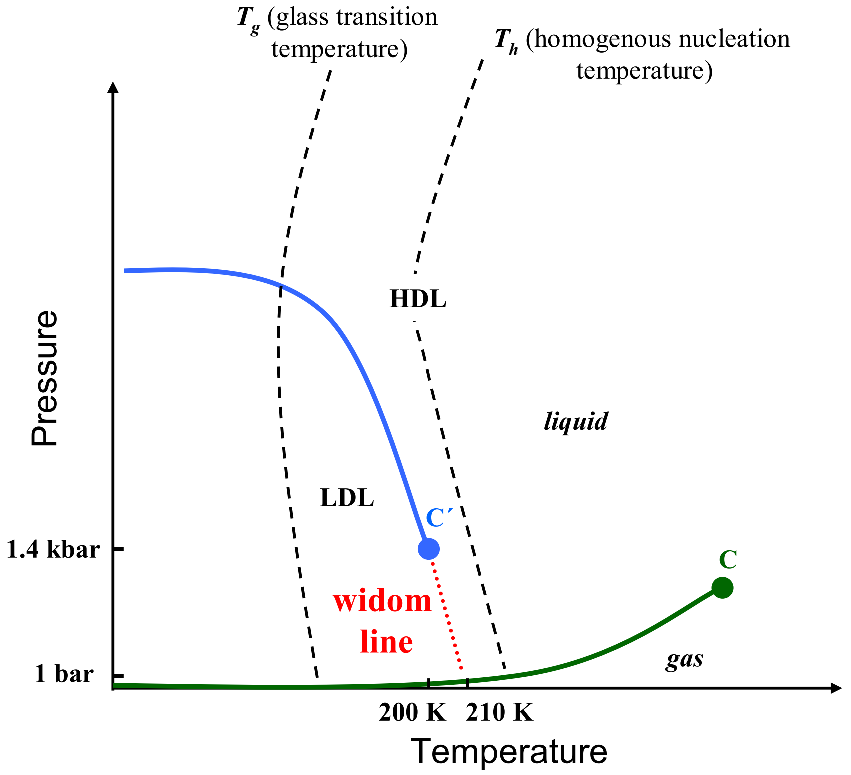

Figure 2.8: Schematic phase diagram of water adapted from [Debenedetti & Stanley, 2003]. The axes are not linear. The critical point C is situated at the end of the gas-liquid coexistence line (see also subsection 2.2.1). The second critical point C' is suggested to be situated at the end of the HDL-LDL coexistence line.

Moynihan, 1997, Tejero & Baus, 1998, Poole, 2005, Paschek, 2005]. Development in computational power has offered new opportunities in studying scientific issues by computer simulations. The question about the configuration of water molecules at very low temperatures has become “ideally suited to computational scrutiny and simulations” [Debenedetti & Stanley, 2003]. Various models of potentials for water molecules, such as ST2 [Stillinger & Rahman, 1974], TIPS2, TIP3P, TIP4P, [Jorgensen, 1983], ST2RF, SPCE [Berendsen, 1987], TIP5P [Mahoney & Jorgensen, 2000] or mW [Molinero & Moore, 2009] have been developed so far. In the simplest models, such as TIP3P and TIP4P H_2O is treated as a rigid molecule only relying on intermolecular forces. The Coulomb potential is used for the electrostatic interaction and the Lennard-Jones potential is responsible for the dispersion and repulsion forces [Stapleton, 1988]. The computational effort largely increases with the number of interaction sites included in a water model. Thus, *“none of the existing empirical water models can adequately describe the whole phase diagram of bulk water”* [Brovchenko & Oleinikova, 2008].

2.1.4 Confined water

The possible existence of a second critical point in the water phase diagram, which is claimed to trigger a "liquid-liquid phase transition" has found supporting feedback not only from the theoretical and computational studies. Recent experimental studies demonstrated the possibility to enter the water no man's land by confining water into very narrow pores [Christenson, 2001]. In order to prevent freezing, water is typically contained in thin, smooth walled silica capillaries, such as Vycor glass [Zanotti, 2005] or micellar-templated MCM-41 and SBA-15 silica [Schreiber, 2001, Oguni, 2007, Jahnert, 2008b]. Also measurements of water confined in carbon nanotubes [Mamontov, 2006] and in activated carbon pores [Bellissent-Funel, 1996, Yamaguchi, 2006] have been reported. The possibility to supercool water below the temperature of homogeneous nucleation can be described by the Gibbs-Thomson effect in confined geometry (see subsection 2.2.3). Thus, confining water into very narrow pores with sizes of only few nanometers was regarded as a "*trick to enter the no man's land*" [Mallamace, 2007b].

Recently, with a series of publications in high impact journals, such as PNAS or Nature Physics, two research groups from the Massachusetts Institute of Technology (MIT) in the United States and from the University of Messina in Italy, showed the possibility to extract low-temperature properties of bulk water from experimental studies on confined water [Xu, 2005, Chen, 2006b, Chen, 2006a, Liu, 2007, Mallamace, 2007b, Mallamace, 2008, Xu, 2009]. Confining water into pores of less than about 2.5 nm is claimed to open new possibilities to experimentally validate computer simulation results of bulk water within the inaccessible temperature region. The essential results from these experiments is that "something happens approximately 10 K below the homogeneous nucleation temperature of bulk water" [Stanley, 2009]. The observed phenomena are claimed to arise from the presence of a liquid-liquid critical point, more precisely from crossing the *widom line* [Franzese & Stanley, 2007], which is the extension of the proposed LDL-HDL coexistence line into the one-phase region (see Figure 2.8) [Chen, 2006b, Chen, 2006a, Liu, 2005, Liu, 2007, Liu, 2008, Mallamace, 2006, Mallamace, 2007b, Mallamace, 2007a, Mallamace, 2008, Xu, 2005, Xu, 2009, Zanotti, 2005, Zhang, 2009]. However, there is no general agreement on exactly how to interpret the observed results [Stanley, 2009].

The above mentioned studies present a number of pioneering results in water research. Particularly three distinct phenomena are found in experimental studies on confined water:

- The transition between two distinct water phases which are characterised by a different degree of HB network development, observed by Fourier-transform infrared (FTIR) measurements [Mallamace, 2007b, Mallamace, 2007a].
- A water density minimum at about 210 K from the temperature-induced

change of the small-angle neutron scattering (SANS) signal [Liu, 2007, Liu, 2008, Zhang, 2009].

- A crossover in the temperature dependence of the characteristic relaxation time of water molecules, including a “fragile-to-strong transition” and the “violation of Stokes-Einstein relation”, observed by various experimental techniques, such as high-resolution quasi-elastic neutron scattering (QENS) [Faraone, 2003a, Faraone, 2003b, Liu, 2004, Liu, 2005, Zanotti, 2005, Chen, 2006a, Swenson, 2005, Swenson, 2006, Hedstrom, 2007], nuclear-magnetic resonance (NMR) [Chen, 2006b, Mallamace, 2006, Mallamace, 2008] and neutron resonance spin-echo (NRSE) [Bellissent-Funel, 2000, Swenson, 2001, Yoshida, 2008].

All above phenomena are assigned to the same temperature region of ~ 210 - 225 K at ambient pressure. The corresponding experimental data were measured on water confined in pores of approximately 1.5 - 2.0 nm pore size. There is no question concerning the existence of these phenomena. Their observation is doubtless. However, the connection of these observations to the properties of bulk water is currently a matter of debate among the water community. Some scientists claim that there should be no influence of confinement other than the stabilization of the liquid phase at very low temperatures [Stanley, 2011]. Others doubt this statement, since introducing water in strong confinement, in order to prevent freezing, progressively makes water “less bulk-like, and water-substrate interactions start to influence both the structure, dynamics and thermodynamic functions” [Soper, 2008, Johari, 2009]. Accordingly, it remains an open question about the real influence of confinement on the reported water phenomena stated above.

2.2 Thermodynamics

This chapter provides a basic thermodynamic description of a transition between two phases. The difference between the two cases of a planar, and of a curved interface is discussed. The derivation of the Kelvin equation is based on the identity of the chemical potentials for a curved liquid and the vapour surrounding it. The detailed analytical derivation is based on the Ref. [Powles, 1985]. The description of melting point depression in confined geometry is presented by two different approaches. The first describes this process in terms of the classical nucleation theory suggested by [Volmer & Weber, 1926]. An alternative approach suggests a curved solid-liquid interface, and correlates the melting point depression with the reduced liquid pressure in pores [Batchelor & Foster, 1944, Everett, 1961]. Both approaches are shown to lead to the Gibbs-Thomson equation. Further, this chapter provides a basic introduction of the phenomenology of the gas sorption mechanism. Hereby, the context is oriented on general literature about gas sorption [Cohan, 1938, Sing, 1985, Zhao, 1998, Rouquerol, 1999], and on some of recently published work in this field [Schreiber, 2002, Wallacher, 2005b, Knorr, 2008, Erko, 2008].

2.2.1 Phase transition, critical point

Experience shows that many substances can exist in different phases. Some familiar examples include the gaseous, the liquid, the solid, the paramagnetic, the ferromagnetic, or the superfluidic phases [McGraw-Hill, 2005]. A transition between two phases can occur either discrete or continuously. For an arbitrary thermodynamic path a first-order phase transition is defined by a non-analytic discontinuity in the development of the first derivatives of the Gibbs' potential, or the free enthalpy $G = G(p, T, N)$:

$$G(p, T, N) = U(S, V, N) + pV - TS, \tag{2.1}$$

$$dG = -SdT + Vdp, \tag{2.2}$$

here U denotes the internal energy, T is the temperature, p is the pressure, V is the volume, N is the particle number, and S is the entropy. For higher-order transitions the old phase transforms into the new one in a continuous manner. Regarding the example of water, both, gas-liquid and liquid-solid phase transitions are characterised by a dramatic change of its physical properties. A transformation from one phase to another results in abrupt change in thermodynamic state functions, such as density and enthalpy. The liquid-gas transition of water, for instance, results in the 1600-fold density decrease [Dill & Bromberg, 2011].

The *equilibrium coexistence line* determines points within the $p-T$ diagram, where the two different phases are stable at the same time. Hence, for a given temperature a liquid is in equilibrium with its vapour state at the corresponding *saturation pressure.* In analogy, for a given pressure a phase transition occurs at the corresponding *transition temperature.* At a phase transition point the equilibrium condition requires identity of the chemical potential μ for both phases:

$$\mu_a(T,p) = \mu_b(T,p), \tag{2.3}$$

with μ_a and μ_b being the chemical potentials of phases a and b, respectively. The total differential of the above equation can be written as:

$$(\frac{\partial \mu_a}{\partial T})_p dT + (\frac{\partial \mu_a}{\partial p})_T dp = (\frac{\partial \mu_b}{\partial T})_p dT + (\frac{\partial \mu_b}{\partial p})_T dp. \tag{2.4}$$

Using the Gibbs-Duhem-Relation $Nd\mu = -SdT + Vdp$ gives:

$$(V_a - V_b)dp = (S_a - S_b)dT, \tag{2.5}$$

and one obtains the so-called *Clausius-Clapeyron equation*, which describes the slope of the equilibrium coexistence line:

$$\frac{dp}{dT} = \frac{1}{T}\frac{\Delta H}{\Delta V}. \tag{2.6}$$

The quantities $\Delta H = T\Delta S$ and ΔV indicate the differences in enthalpy (latent heat) and in volume for the two phases. As previously mentioned, the two derivatives of the Gibbs potential, i.e. the Volume $V = (\partial G/\partial p)_T$ and the entropy $S = (\partial G/\partial T)_p$ change discontinuously by crossing the phase transition line defined in Equation 2.6. Approaching the critical point, the discontinuous change in volume and entropy vanishes ($\Delta V \to 0$ and $\Delta S \to 0$). Beyond the critical point the two previously distinct phases become indistinguishable. The properties of these two phases approach one another resulting in a single one. The position of the critical point in the p-T diagram for water is $T = 647$ K and $p = 218$ bar [Tipler, 1994] (see also Figure 2.8).

2.2.2 The effect of curvature

The effect of a curved fluid surface is important for many thermodynamic systems. Water droplets in clouds, for instance, are in equilibrium with the supersaturated environment. Capillary condensation in mesopores takes place below the corresponding saturation pressure of the bulk liquid. Both effects can be related to the shape of the liquid-vapour interface.

For the case of a flat liquid-vapour interface, in equilibrium the pressure of the liquid p_l is equal to that of the vapour phase p_v. This quantity is further denoted as the bulk saturation pressure p_0. For a thermodynamic system characterised by a curved liquid-vapour interface, the equilibrium pressure of the liquid differs from that of the vapour phase $p_l \neq p_v$. For a spherical fluid droplet with radius R, the pressure difference between the two phases is determined by the surface tension σ_{lv}, representing the energy which is necessary in order to create a new unit surface of the liquid, and the curvature of the interface $1/R$. In equilibrium, a change of the droplet volume energy pdV is compensated by the change of its surface energy $\sigma_{lv} \cdot dA$, which corresponds to the energy balance $(p_l - p_v) \cdot 4\pi R^2 dR$ and $\sigma_{lv} \cdot 8\pi R dR$, respectively. Combining both quantities yields the pressure difference $\Delta p = p_l - p_v$ for a curved fluid surface:

$$\Delta p \equiv \Pi = \frac{2\sigma_{lv}}{R}. \tag{2.7}$$

Equation 2.7 is named after Thomas Young and Pierre-Simon Laplace who independently derived this equation in 1805. For an arbitrary curved interface of two arbitrary phases with the principle curvatures $1/R_1$ and $1/R_2$ the pressure difference is calculated by:

$$\Pi = \sigma_{lv}(\frac{1}{R_1} + \frac{1}{R_2}) \tag{2.8}$$

Note that the sign of Π depends on the shape of the curved interface. For convex surfaces, as for a spherical fluid droplet, the pressure difference $(p_l - p_v)$ is positive. For concave interfaces Π is negative (see Figure 2.9).

The new saturation pressure resulting from the curved fluid-vapour interface can be calculated applying the identity of the chemical potentials for the two phases in equilibrium (see Equation 2.3). The corresponding physical quantities are assigned by the index ∞ for the case of a flat surface with the infinite curvature radius. For the case of a curved surface the assignment by the index R is performed:

$$\mu_l^R - \mu_l^\infty = \mu_v^R - \mu_v^\infty. \tag{2.9}$$

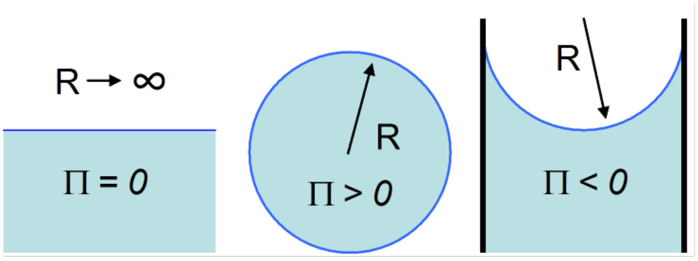

Figure 2.9: Young-Laplace pressure Π caused by a curved liquid surface. Planar interface with an infinite curvature radius (left). Fluid droplet with a convex surface (middle). Concave fluid meniscus in a mesopore (right). The liquid-vapour interface is denoted by the dark blue line.

The phases a and b from Equation 2.3 now correspond to those of the liquid and the vapour, assigned by the indices l and v, respectively. With the Gibbs-Duhem-Relation for constant temperature $Nd\mu = Vdp$ one obtains after the integration:

$$\int\limits_{p_l^{\infty}}^{p_l^R} \frac{dp}{\rho_l} = \int\limits_{p_v^{\infty}}^{p_v^R} \frac{dp}{\rho_v}, \tag{2.10}$$

here ρ_l and ρ_v denote the number density values of the two phases. As mentioned at the very beginning of this subsection, the saturation pressure p_0 for a flat fluid-vapour interface is equal to those of the liquid and the vapour phases. Hence, $p_l^{\infty} = p_v^{\infty} = p_0$. Assuming the vapour phase to be an ideal gas $p = \rho_v kT$ (assumption I), with Equation 2.7 one obtains:

$$\int\limits_{p_0}^{\frac{2\sigma_{sl}}{R}+p_v^R} \frac{1}{\rho_l} dp = \int\limits_{p_0}^{p_v^R} \frac{kT}{p} dp, \tag{2.11}$$

k is the Boltzmann constant and T is the temperature. For an incompressible liquid ($\rho_l(p) = \rho_l$) at the coexistence point (assumption II), the integration gives:

$$\frac{1}{\rho_l}(\frac{2\sigma_{lv}}{R} + p_v^R - p_0) = kTln(p_v^R/p_0). \tag{2.12}$$

Thirdly it is assumed that the Young-Laplace pressure is much larger than the pressure difference between the new saturation pressure p_v^R and that of the bulk p_0,

$2\sigma_{lv}/R \gg (p_v^R - p_0)$ (assumption III). The result is the so-called *Kelvin equation*, which gives the saturation pressure of a curved liquid:

$$p_v^R = p_0 \cdot exp(\frac{2\sigma_{lv}}{R}\frac{1}{\rho_l kT}) = p_0 \cdot exp(\Pi \frac{V_l^M}{R_G T}), \tag{2.13}$$

where V_l^M is the molar volume of the liquid phase, and R_G is the gas constant.

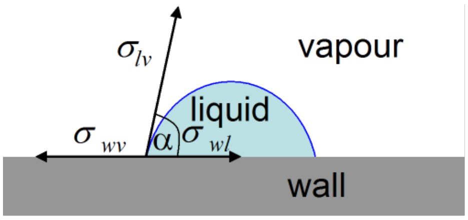

Figure 2.10: The contact angle α determines the surface wetting behaviour.

This equation shows an increase of the saturation pressure for the case of convex liquid-vapour interfaces, and its decrease for concave interfaces, as compared to flat interfaces. For a system which is characterised by a concave liquid-vapour interface, as for a liquid in a mesopore Figure 2.9, the introduction of the solid wall as a third phase is necessary. A liquid droplet on a solid surface is determined by three different specific energies of interaction (see Figure 2.10). The actual shape of the droplet depends on the particular magnitude of the values for σ_{wl}, σ_{wv} and σ_{lv}, representing the respective wall-liquid, wall-vapour and liquid-vapour specific interaction energies. The strength of interaction of the solid wall with the liquid is usually described in terms of the *contact angle* α. The relationship between the contact angle and the corresponding specific surface energies of the three phases is given by the *Young-equation* [Hunter, 2001]:

$$\sigma_{wl} + \sigma_{lv} cos\alpha - \sigma_{wv} = 0. \tag{2.14}$$

Good surface wetting implies $\sigma_{wl} < \sigma_{wv}$, giving a contact angle below $\pi/2$ (surface coverage is favoured). For a perfectly wetting surface with $\alpha = 0$ Equation 2.14 reduces to the so-called Antonow relationship $\sigma_{wv} - \sigma_{wl} = \sigma_{lv}$ [Antonow, 1907]. In contrast, for poorly or non-wetting surfaces with $\sigma_{wl} > \sigma_{wv}$ (wall-vapour interface is favoured) wetting angles between $\pi/2$ and π, are observed.

The mechanism of capillary condensation (i.e. the gas-liquid transition) in mesopores is described in terms of the formation of a hemispherical meniscus with a concave liquid-vapour interface. The nature of phase transitions in confined geometry is dependent on the interaction strength between the three phases, i.e. wall, vapour and liquid. For non-perfect wetting systems in equilibrium the radius of the curved fluid-vapour interface R is larger than that of the pore R_p, giving $R = R_p cos\alpha$ (see Figure 2.11). The Kelvin-equation is often used for the purpose of determining

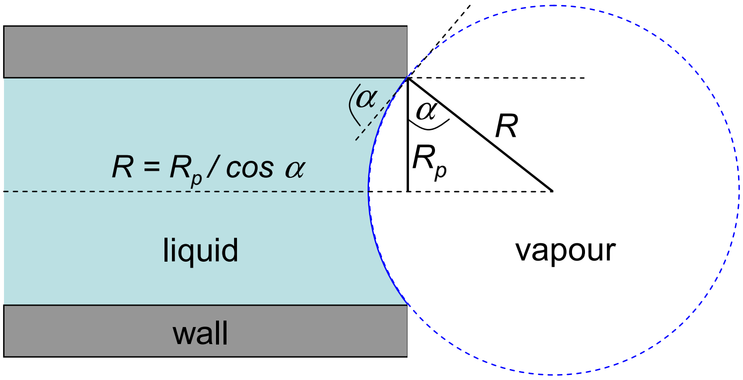

Figure 2.11: Non-perfect fluid wetting behaviour in a pore with Radius R_p. The wetting angle θ depends on the magnitudes of the different specific interface energies σ_i, determined by Equation 2.14.

the pore radius of a porous material. The equilibrium pressure p_v^R in Equation 2.13 for the formation of a curved fluid meniscus in a cylindrical pore with radius R_p leads to the following formula:

$$ln(\frac{p_v^R}{p_0}) = \frac{2\sigma_{lv} cos\alpha}{R_p} \frac{V_l^M}{R_G T}, \tag{2.15}$$

where $\sigma_{lv} cos\alpha$ is regarded as the difference of the specific surface interface energies $(\sigma_{wv} - \sigma_{wl})$ (see Equation 2.14). An important aspect can also be easily observed in Equation 2.15. In hydrophilic confinement ($\alpha < \pi/2$) the liquid-vapour phase transition is shifted to lower pressures compared to the bulk saturation pressure p_0. Consequently, water in hydrophobic confinement ($\alpha > \pi/2$) condensates at $p_v^R/p_0 > 1$. Hence, the effect of fluid curvature in mesopores is already included by the contact angle.

2.2.3 Homogeneous nucleation (Gibbs-Thomson effect)

Nucleation theory

The fist step of the vapour-liquid (or the liquid-solid) phase transition is characterised by an accumulation of gas molecules (or those of a liquid) to small droplets (or clusters) of the new phase [Schmelzer, 2005]. In the classical theory this process is described in terms of formation of a nucleus of the new phase. In analogy to the previously derived effect of curvature one uses the argument that the change of the free enthalpy (see Equation 2.1) is given by the energy balance between the spent surface energy and the gained volume energy [Volmer & Weber, 1926]:

$$\Delta G = A\sigma - VG_V, \tag{2.16}$$

where σ and G_V are the specific energies of the surface A and the volume V, respectively. For a spherical nucleus, e.g. for a liquid droplet in vapour, one obtains:

$$\Delta G = 4\pi R^2\sigma - \frac{4\pi R^3}{3}G_V, \tag{2.17}$$

where $\sigma = \sigma_{lv}$ (or $\sigma = \sigma_{sl}$) denotes the surface tension of the liquid (or the specific solid-liquid interface energy) and R is the nucleus radius. The development of the free enthalpy change ΔG with the radius of the nucleus R is visualised in Figure 2.12. It exhibits a maximum at a particular value which is the so-called *critical radius* R^*.

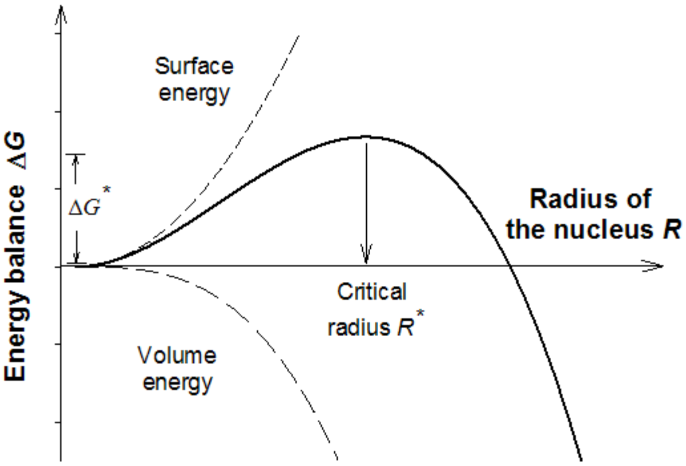

Figure 2.12: Energy balance from Equation 2.17 as a function of the nucleus radius below the bulk phase transition point.

The value for the critical radius can be calculated from taking the derivative of the energy balance in Equation 2.17. The result yields the size of the critical radius which must be formed before a droplet (or a solid crystal) is stable and begins to grow:

$$R^* = \frac{2\sigma}{G_V}. \tag{2.18}$$

Note that both, the vapour-liquid phase transition (condensation) and the liquid-solid phase transition (freezing) can be described in a similar way. Nuclei with the radius smaller than R^* are not stable and evaporate (remain in liquid state). If the nucleus radius exceeds the value of R^*, rapid growth of liquid droplets (solid clusters occurs). Inserting the critical radius into Equation 2.17 leads to the barrier height for a stable nucleus (*activation energy*):

$$\Delta G^* = \frac{16\pi\sigma^3}{3G_V^2}. \tag{2.19}$$

Combining the differential form of the free enthalpy (Equation 2.2) with the Gibbs-Duhem relation for constant temperature $Nd\mu = Vdp$ one obtains that the volume energy G_V is proportional to the difference of the chemical potentials of the two phases. In equilibrium, this difference is zero, which gives infinite values for R^* and ΔG^* exactly at the bulk phase transition point.

Gibbs-Thomson equation

The radius R^* of the stable spherical nucleus in supercooled regime can be calculated using the definition of the free enthalpy in equilibrium:

$$G_V = (\Delta H - T\Delta S)/V = 0. \tag{2.20}$$

For the liquid-solid transition the change in volume V can be neglected. Hence, one uses $\Delta S \approx \Delta S_0 = \Delta H/T_0$, with the bulk melting temperature T_0. From Equation 2.20 one obtains the volume energy for a supercooled fluid [Christenson, 2001]:

$$G_V \approx \Delta H \frac{(T_0 - T)}{T_0 V}. \tag{2.21}$$

This equation can be understood as the change of the chemical potential of the liquid in the supercooled regime ($G_V \propto (\mu - \mu_0)$, with μ_0 being the value at T_0, compare this also with Equation 2.9). Inserting this result into Equation 2.18 leads to the so-called *Gibbs-Thomson equation*, which relates the size of the stable nucleus to the corresponding degree of supercooling. Hence, the melting point suppression ΔT_m of a spherical crystal with the radius R^* is given by:

$$\Delta T_m = T_0 - T_m = \frac{2\sigma_{sl}}{R^*}\frac{V^M T_0}{\Delta H^M}. \tag{2.22}$$

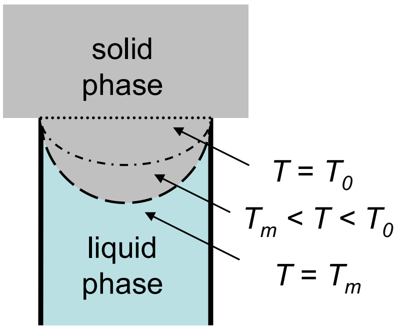

Figure 2.13: Overfilled pore with bulk solid outside and confined liquid within a pore. The curvature of the liquid meniscus changes with the temperature. Figure adapted from [Everett, 1961].

This effect is important for studies of freezing and melting processes of confined liquids. The depression of the water melting point was shown to follow Equation 2.22 by confining water into mesoporous MCM-41 and SBA-15 silica materials (see section 2.3) [Schreiber, 2001, Jahnert, 2008b]. Due to the geometrical restriction of a mesopore, a stable nucleus can only be formed at lower temperatures compared with the bulk phase.

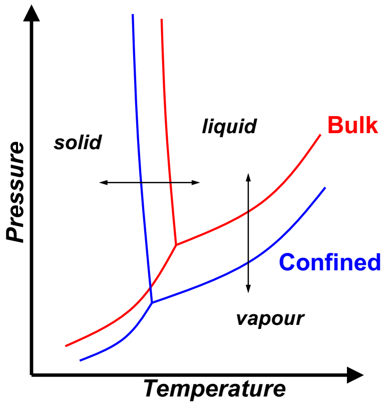

Figure 2.14: Phase diagram shift for water in confinement. The two arrows indicate two different types of measurements, i.e. isothermal pressure change (vertical) and isobaric temperature change (horizontal).

An alternative expression for the melting point depression in mesopores is given in Refs. [Batchelor & Foster, 1944, Everett, 1961, Rennie & Clifford, 1977, Christenson, 2001]. Similar to the case of previously introduced reduced saturation pressure in mesopores which is explained by the Kelvin equation, the phenomenon of melting point depression can be described aussuming the exsistence of a hemispherical concave liquid-solid meniscus.

If the liquid wets the pore walls in the presence of the solid phase, the liquid will be thermodynamically favoured in confinement [Christenson, 2001, Denoyel & Pellenq, 2002]. Consequently, the liquid phase in pores is in equilibrium with the bulk solid also at temperatures below T_0 (see Figure 2.13). Growth of an ice crystal into the pore would involve the formation of material having a higher chemical potential than the bulk ice [Everett, 1961]. Freezing of pore water in equilibrium with the bulk ice takes place by penetration of the bulk phase into the pore building a hemispherical interface [Handa, 1992, Brun, 1977, Enustun, 1978] (see

Figure 2.13). The chemical potential values of the liquid and the solid states approach each other upon the growth of the solid-liquid meniscus. The equilibrium condition is given by the generalised form of the Young-Laplace equation (replacing σ_{lv} by σ_{sl} in Equation 2.7). The quantitative dependence of the melting point depression ΔT_m on the pore radius R_p can be derived using the Kelvin equation (Equation 2.15), or the Young-Laplace equation (Equation 2.8) to correlate the pore size with the reduced saturation pressure (corresponding to the reduced chemical potential by Equation 2.9). Hereby, the specific interface energies are in the limit of complete wetting of the pore walls by the liquid phase $\sigma_{ws} - \sigma_{wl} = \sigma_{sl}$ [Schreiber, 2001, Jahnert, 2008b]. The Clausius-Clapeyron equation (Equation 2.6) is used to correlate this shift in the saturation pressure with the corresponding shift in phase transition temperature [Batchelor & Foster, 1944, Everett, 1961]. Essentially, this calculation follows the steps from Equation 2.18 to Equation 2.21, since G_V can be regarded as the pressure difference between the two phases (see the derivation of Equation 2.8). In this manner one obtains the Gibbs-Thomson equation (Equation 2.22) expressing the melting point depression in a perfectly wetting cylindrical mesopore with $R^* = R_p$, where R_p is the radius of the mesopore [Christenson, 2001]. The effects of confinement can be summarised by a shift of the liquid-vapour and solid-vapour equilibrium lines a the bulk material towards lower pressures and temperatures (see Figure 2.14) [Batchelor & Foster, 1944].

Again, regarding the Gibbs-Thomson effect, also an elevation of the liquid melting point in confinement is possible. This case presumes that the pore walls prefer solid rather than the liquid phase. Equation 2.22 then gives $\Delta T_m < 0$, which is parallel to the case of hydrophobic pore walls leading to $p_v^R/p_0 > 1$ in the Kelvin equation (Equation 2.15). The effect of melting point elevation is reported from experimental studies of organic fluids in nanoporous carbons [Alba-Simionesco, 2006, Xia, 2006].

2.2.4 Sorption

Basic concepts

The concept of adsorption generally describes an accumulation of one or more gas components (*adsorptive*) on the surface of a solid (*adsorbent*). A general adsorption process is characterised by enrichment of the adsorptive in the *adsorption space*. Material in adsorbed state is called *adsorbate*. In case that the molecules of the adsorptive penetrate through the surface layer and enter the bulk structure of the solid, the term absorption is used. In most cases it is difficult to distinguish between the two cases of adsorption and absorption. Hence, it is convenient to use the wider term *sorption* which includes both phenomena. The derived terms *sorbent*, *sorbate* and *sorptive* are then used. Within the present work the term adsorption is used to denote the process in which adsorptive molecules accumulate within the *interfacial layer*. Its counterpart, desorption, denotes the reverse process, in which the amount of adsorbed material decreases. Thus, the prefix denotes the direction of the studied sorption process.

Depending on the interaction between sorptive and sorbent the process can be classified in two different types i.e. *physisorption* and *chemisorption*. Physisorption is a general phenomenon, which occurs whenever gas molecules are mutually brought into contact with the surface of a solid. It is characterised by intermolecular Van der Waals forces giving binding energies in the order of only few kJ/mol (heat of condensation). The process of chemisorption is characterised also by strong (covalent) bonding between gas and the solid surface, chemically modifying the latter. The binding energies are thereby in the order of 50 - 500 kJ/mol, which is already in the order of chemical reactions. While for physisorption the thickness of the adsorbed film layer can reach several monolayers, chemisorption is generally regarded to be limited to the first monolayer closest to the surface.

A *soption isotherm* implies a plot of the amount of adsorbed material versus the corresponding equilibrium pressure at a fixed temperature. Different types of isotherms are discussed later within this chapter. Note, that a *hysteresis* arises when the adsorption and desorption isotherm curves do not coincide. The origin of the pressure hysteresis between filling and emptying can be attributed either to the metastability of the adsorption branch [Saam & Cole, 1975], or it can be influenced by collective phenomena such as cavitation and pore blocking [Thommes, 2006]. The third explanation implies different mean curvatures of the fluid film for the beginning of the processes of capillary condensation and evaporation, respectively [Cohan, 1938]. The transition between the vapour and the liquid phases of the experimental fluid is analytically described by the classical Kelvin equation (see subsection 2.2.3). Thus, the process of capillary condensation in hydrophilic pores takes place at a reduced vapour pressure p/p_0. Utilising an experimental sorption isotherm in order to determine the pore radius R_p for open cylindrical pores, the desorption rather than the adsorption branch, is usually used [Kruk, 2000, Kikkinides, 2003, Rigby & Fletcher, 2004]. In this case one uses Equation 2.15. According to Cohan *et al.* [Cohan, 1938] one can also use the adsorption branch for the determination of the pore radius replacing R_p by $R_p/2$ in Equation 2.15.

For the determination of the surface area of a solid by means of a sorption process it is necessary to distinguish between the *external* and the *internal* surface. The external surface is usually regarded as the envelope surrounding discrete particles or agglomerates. However, the external surface is difficult to define precisely because solid surfaces are rarely smooth on the atomic scale. A suggested convention is that the external surface includes all the prominences and also the surface of those cracks which are wider than they are deep. The internal surface then comprises the walls of all cracks, pores and cavities which are deeper than they are wide and which are accessible to the adsorptive. Note that the accessibility of pores may also depend on the size and shape of the gas molecules. Thus, the determined area and the volume enclosed by the internal surface may change for different adsorptives.

Within the context of physisorption the pores can be a classified according to their size (see Table 2.1).

50 nm $< d$	macropores
2 nm $< d <$ 50 nm	mesopores
$d <$ 2 nm	micropores

Table 2.1: Classification of pores by means of their size d.

The mechanism of pore filling depends on many parameters, including the shape of the pores. It is strongly influenced by adsorptive properties and by the adsorbent-adsorbate interactions. The limits in Table 2.1 are to some extent arbitrary. This classification can be understood in terms of different filling mechanisms. The micropore volume filling is distinct from the surface coverage which takes place on the walls of open macropores or mesopores. Micropore filling may be regarded as a primary physisorption process. On the other hand, physisorption in mesopores takes place in two more or less distinct stages, i.e. monolayer multilayer adsorption and capillary condensation (see Figure 2.15). Monolayer adsorption implies that all adsorbed molecules are in direct contact with the adsorbent surface (Figure 2.15B). If more than one layer of molecules is adsorbed, and not all adsorbed molecules are in direct contact with the solid surface, multilayer adsorption has occurred (Figure 2.15C). During capillary condensation the residual pore space is filled with condensate separated from the gas phase by a hemispherical concave meniscus (Figure 2.15D). Further process of capillary condensation is characterised by the flattening of the menisci (Figure 2.15E). As previously mentioned, the processes of capillary condensation and evaporation are often shifted in pressure forming a hysteresis.

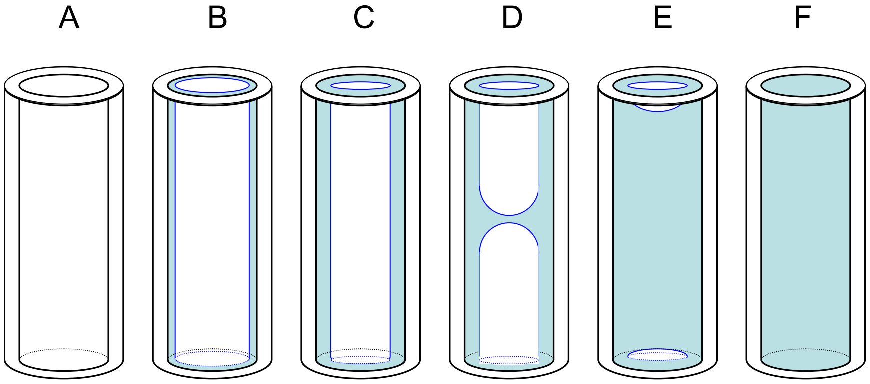

Figure 2.15: Pore filling process. Empty and filled stages of mesopores are denoted as A and F, respectively

Note that the term capillary condensation should not be used to describe micropore filling. For pores smaller than approximately 2 nm the pore filling mechanism does not proceed via the liquid-bridge formation (i.e., formation of meniscii), but rather via an axial filling mode [Grunberg, 2004]. A meniscus made up of only few molecules is hard to be defined anyway. For the description of macropore filling mechanism also gravitational effects have to be considered. Thus, the classification according to Table 2.1 is not only due to nomenclature reasons but it also has its physical basis.

The experimental methods for the determination of the adsorbed amount as a function of equilibrium pressure consists basically of two approaches which have been developed within the last decades. The *gravimetric* method applies a direct mass measurement of the adsorbed material by a proper weighting device during a sorption process. The *volumetric* method is based on determining the amount of gas which disappears from the gas phase during an adsorption step. For a given constant volume and temperature of the system the change of the gas pressure within an adsorption step is directly proportional to the amount of adsorbed material. For low pressures the calculation can be performed applying the equation of state for an ideal gas:

$$pV = nR_GT, \tag{2.23}$$

where n denotes the amount of the ideal gas in moles. The amount of adsorbed material can be calculated using Equation 2.23 which yields $\Delta n = \Delta p \cdot (V/R_GT)$ (see also subsection 3.3.1).

Types of isotherms

As previously mentioned, in order to visualise results of a sorption experiment the measured amount of adsorbed material is plotted versus the corresponding relative pressure p/p_0. Here, p_0 again indicates the saturation vapour pressure of the particular fluid at the given temperature. Additional normalisation of the adsorbed gas amount to the value of the total sample capacity gives the filling fraction of the sample. Most sorption isotherms can be classified into one of six categories (see Figure 2.16).

- Type I isotherms are the so-called reversible Langmuir isotherms. These are often characterising microporous solids which have relatively small external surfaces (e.g. activated carbons, molecular sieve zeolites and certain porous oxides). The micropore volume, rather than the internal surface area, governs the limiting uptake.
- Type II reversible isotherms are characterising low-porous or macroporous adsorbents. The shape represents a continuous monolayer-multilayer adsorption. Point B indicates the beginning of the almost linear middle section of the isotherm. This point is often taken to indicate the stage at which monolayer coverage is complete and multilayer adsorption is about to begin.

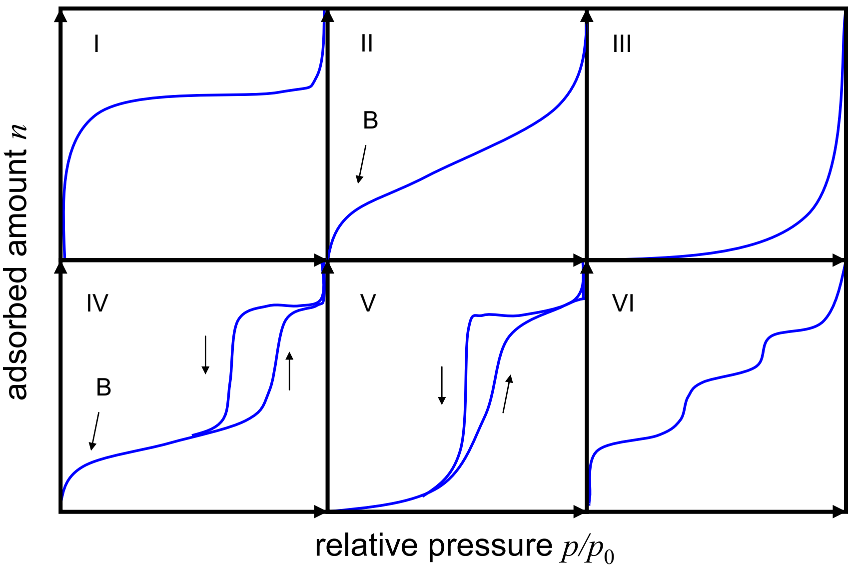

Figure 2.16: Types of isotherms, adapted from [Rouquerol, 1999]. The values for p/p_0 range between 0 and 1. The adsorbed amount n starts at zero.

- Type III represents convex reversible isotherms for which no point B can be identified. Similar as for the Type I the sorbent-sorbate interactions play an important role. There is only a few number of systems, e.g. nitrogen on polyethylene, for which isotherms of this type are observed.
- The hysteresis loop is the characteristic feature related to the isotherms of Type IV. Since the initial part follows the same path as the corresponding part of a Type II isotherm, it is attributed to monolayer-multilayer adsorption. Capillary condensation taking place in mesopores, together with the limiting uptake in the region of high relative pressures give its characteristic shape. Type IV isotherms are observed by many mesoporous industrial sorbents.
- Isotherms of the Type V are related to the Type III isotherms. The shape of the adsorption branch is going back to the weak sorbent-sorbate interaction. This type of isotherms is observed only for certain porous systems.
- The stepwise multilayer adsorption on a uniform non-porous surface characterises isotherms of Type VI. The step height gives the monolayer capacity for each adsorbed layer. In the simplest case this quantity can remain nearly constant for two or three adsorbed layers. The best examples for isotherms of this type are those obtained with argon or krypton on graphitised carbon at 77 K.

For the purposes of this work it is necessary to understand the sorption behaviour of water within mesoporpous materials. Isotherms of Type IV are those to be expected for fluid sorption experiments using MCM-41 and SBA-15 materials (see section 2.3).

2.3 Porous materials

In general, porous materials are characterised by a large surface area, compared to the case of a homogeneous solid. Their application is manifold. Porous materials can be applied for heterogeneous catalysis, sensor technology, gas storage and not least for scientific studies of adsorption processes. The term porosity is often used for the pore volume fraction of a material. It is important to distinguish between open and closed pores, which determine accessible and inaccessible volumes, respectively. In a sorption experiment only the ratio between the accessible pore volume and the total sample volume is determined. The actual values can vary for different adsorption gases (see subsection 2.2.4). In contrast to this, porosity values obtained in a scattering experiment, with X-rays for instance, can also include the pore volume which is inaccessible for the adsorption gas. First porosity studies of inorganic materials were limited only to naturally occurring minerals. However, within the last decades the chemical synthesis of ordered and disordered porous materials has developed to an own scientific and technological sector. Particularly, the synthesis of high-ordered porous materials on the basis of silica is described here in more detail.

A common aspect for all materials described in this chapter is the the presence of template structures [Hoffmann, 2006]. For the case of zeolites, for instance, the synthesis usually includes alumo-silicates in presence of alkylamines as template molecules, resulting in pore sizes in the order of only few Ångströms (micropores). These so-called molecular sieves are characterised by high-ordered pore structures [Davis, 1988]. Another important synthesis mechanism implies so-called sol-gel-processes which are applied for xerogels and high-porous aerogels. The drying process of a gel made of poly-condensed water-glass mixture results in compression of the silica-matrix by capillary forces giving porosity values of around 50 %. A supercritical drying process (see subsection 2.2.1) allows synthesis of high porous materials with porosity values reaching 99.8 % for aerogels [Burgess, 1989].

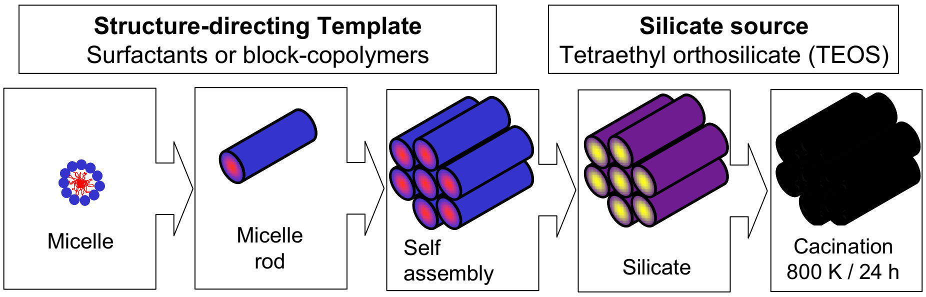

Figure 2.17: Illustration of the synthesis mechanism of MCM-41 and SBA-15 mesoporous materials.

Since 1992, synthesis of ordered mesoporous silica materials is performed by a specific template mechanism M41S [Kresge, 1992], which can be regarded as a combination of the two synthesis types, for zeolits and aerogels, respectively [Beck, 1992]. The resulting materials consist of uniform pores which are perfectly ordered on a lattice. The pores of few nanometers diameter are separated by amorphous silica walls. By means of the M41S method a number of differently structured mesoporous materials can be synthesised, including three-dimensional cubic (MCM-48), lamellar (MCM-50) and hexagonally-arranged cylindrical (MCM-41) systems. The principle of the synthesis by the template mechanism is visualised in Figure 2.17.

2.3.1 MCM-41

The name MCM is going back to Mobil Composition of Matter [Ciesla & Schuth, 1999] or Mesoporous Crystalline Material. The basic requirement for the synthesis process is the attractive interaction between the template molecules and the silica precursor. The former ones are represented by cationic surfactant molecules [Beck, 1992]. Particularly, the alkyl chain length of the used tenside determines the pore width of the final material. The concentration and the temperature are the determining parameters for the self-assembly of micelles into a two-dimensional hexagonal arrangement of elongated cylinders. These act as the template for the subsequently added tetraethyl orthosilicate (TEOS). During the subsequent drying and calcination processes around 800 K the initial surfactant molecules and water are extracted from the composite material [Findenegg, 2008].

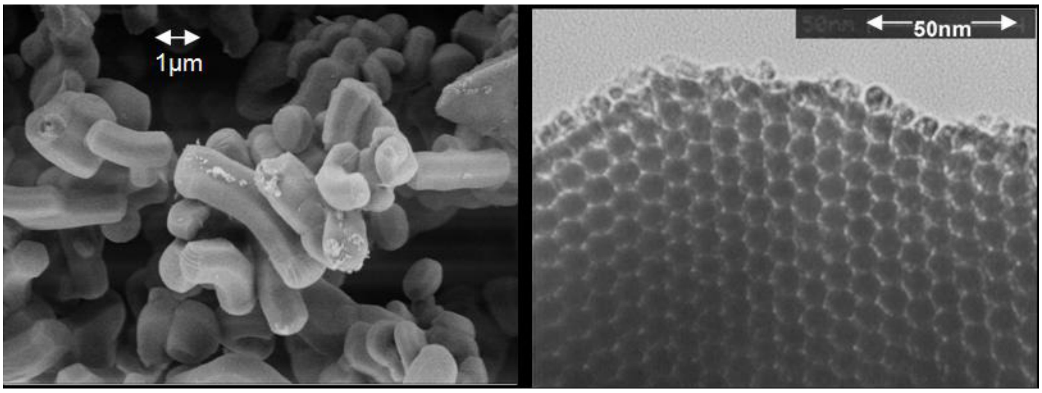

Figure 2.18: SEM (left) and TEM (right) pictures of MCM-41 materials, from [Prass, 2011] and [Akcakayiran, 2005], respectively.

A number of important factors influence the actual pore structure in MCM-41, i.e. the surfactant concentration, the pH-value of the solution, time of the synthesis and that of the hydrothermal treatment [Broyer, 2002, Palmqvist, 2003]. The development of optimised synthesis techniques is described in [Edler & White, 1997, Cai, 1999, Sayari, 1999] in more detail. As the result, materials with pore sizes ranging between 2 nm and 5 nm can be synthesised [Findenegg, 2008]. These materials consist of elongated grains with dimensions around 0.3 nm x 10 µm.

Each grain exhibits a two-dimensional hexagonal sturucture of cylindrical pores (Figure 2.18). The pore surface is shown to be smooth and is almost free of defects [Grunberg, 2004]. Within this work, MCM-41 materials with six different pore sizes, ranging between 2.0 nm and 4.4 nm are used. They are denoted as MCM20, MCM25, MCM30, MCM34, MCM39 and MCM44, where the numbers indicate the pore diameter (in Ångströms), determined by the improved Kruk-Jaroniec-Sayari (iKJS) method, giving the maximum of the pore size distribution curve [Jaroniec & Solovyov, 2006]. All materials were synthesised by S. Jähnert and D. Akcakayiran at the Berlin University of Technology using the method of Grün and collaborators, which is described in [Grün, 1997] and in [Jahnert, 2008b, Jahnert, 2008a, Akcakayiran, 2008], in more detail.

2.3.2 SBA-15

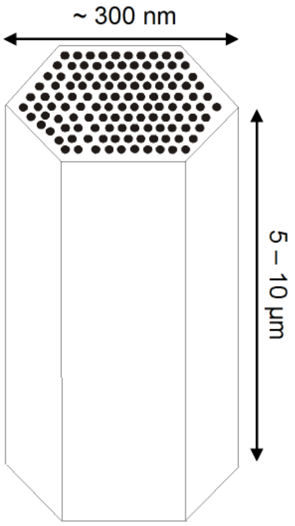

Figure 2.19: Illustration of an idealised grain of SBA-15 exhibiting a two-dimensional hexagonal pore structure.

In order to synthesise porous silica materials with larger pore sizes than MCM-41, larger template molecules are needed. The replacement of surfactant molecules by amphiphilic bloc-copolymers allows synthesis of materials with pore sizes up to 10 nm [Findenegg, 2008]. The synthesis of such new mesoporous materials with similar properties as MCM, but with larger pore sizes, has first been performed at the University of California in Santa Barbara. The so-called SBA-15 materials (Santa Barbara Amorphous type material) also exhibit a two-dimensional hexagonal structure of cylindrical pores with amorphous silica pore walls. However, the relatively large roughness of the pore walls [Ravikovitch & Neimark, 2001] and particularly the existence of a low-density shell, the so-called *microporous corona* [Imperor-Clerc, 2000, Zickler, 2006], are the marking-off attributes for SBA-15 materials. Moreover, the mesopore structure of SBA-15 seems to exhibit a system of interconnected channels which even allowing the fabrication of carbon replica materials CMK-3 (Carbon Mesostructures at Korea Advanced Institute of Science and Technology) [Ryoo, 2001].

The detailed structure examination of SBA-15 is an ongoing field of research [Kruk, 2000, Shin, 2001, Galarneau, 2003, Khodakov, 2005, Zickler, 2006, Jahnert, 2008a, Muter, 2009, Findenegg, 2010]. Refined models of the pore structure have been evolved within extensive experimental and theoretical studies [Hofmann, 2005, Jahnert, 2009, Muter, 2009]. However, the influence of the adsorbate, particularly of water, on both, the mesopore and micropore structures is still not fully understood. Adsorption of water in ordered mesoporous silica represents a much more complex phenomenon, as the pore walls can be changed by interaction with water (chemisorption). It is well-known that capillary condensation of water in freshly calcined samples of SBA-15 takes place only at, or even slightly above the saturation vapour pressure [Erko, 2008, Erko, 2010], indicating a hydrophobic nature of the pore walls. In subsequent sorption cycles, the capillary condensation pressure shifts to lower values and eventually reaches some limiting value. This observation indicates a gradual change of the surface properties of the pore walls, possibly even an irreversible change of the silica surface structure through the repeated adsorption and desorption of water. Similar changes of water isotherms were also reported for other silica materials [Boissiere, 2005], but have not yet been followed systematically.

The SBA-15 material used within this work has been synthesised by S. Jähnert from Berlin Institute of Technology using the method of Zhao *et al.* [Zhao, 1998]. The used material exhibits a uniform pore size of 8.9 nm (determined by the improved Kruk-Jaroniec-Sayari (iKJS) method [Jaroniec & Solovyov, 2006]), and is therefore denoted by SBA89.

2.4 Scattering theory

Scattering of different types of radiation, such as electrons, photons or neutrons are important experimental methods for the analysis of material properties, including both, the structure and dynamics. Within this thesis analysis of the structural properties of water together with those of silica mesopores was performed by means of elastic scattering of X-rays and neutrons. Additionally, this thesis also includes the analysis of water dynamics, preformed by means of inelastic scattering of visible light (Raman scattering). The latter was performed by a qualitative comparison of the experimental spectra with those reported in literature. This "fingerprint" method does not include a quantitative calculation of the energy transfer between a photon and a water molecule during a scattering process. Therefore, the following short description of the scattering theory is essentially limited to the case of elastic scattering. Only the process of absorption of the incident beam, which can be regarded as an inelastic scattering process, is discussed in more detail. The general scattering theory in subsection 2.4.1 is based on the text book by P. Lindner and T. Zemb. [Lindner & Zemb, 2002], in particular, on the chapter by P.N. Pusey. subsection 2.4.2 describes scattering from ordered systems, such as crystals, based on [Pecharsky & Zavalij, 2009]. The derived relations for a general scattering process are applied for the case of scattering with X-rays and neutrons in subsection 2.4.3. Important aspects for small- and wide-angle scattering are outlined in subsection 2.4.4. A basic introduction of Raman scattering is given in the end of this chapter in subsection 2.4.5.

2.4.1 General description

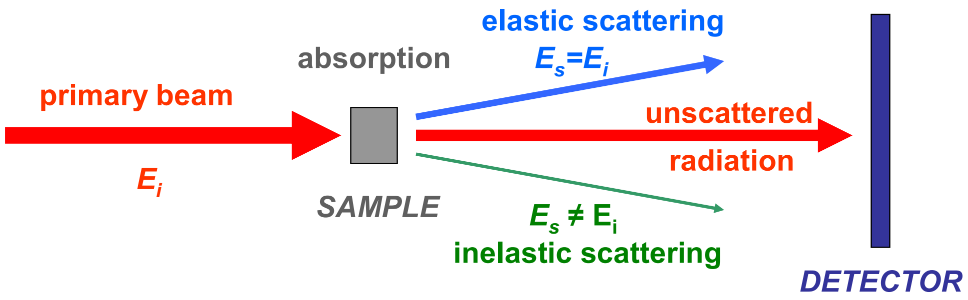

Figure 2.20: A general process of radiation interaction with matter includes absorption, elastic scattering and inelastic scattering. If no interaction takes place, the radiation waves do not change their initial trajectory.

Scattering implies a change of the trajectory of a wave in a course of interaction with matter. Hereby, the composition, together with the arrangement of the scattering centres determine the nature of the scattering process. Generally, a scattering process includes four different scenarios. 1) A certain proportion of primary waves is absorbed within the sample. More details about absorption of different types of radiation are given in subsection 2.4.3. The transmitted radiation is divided into an 2) unscattered part, that of 3) elastically scattered, and finally the part of 4) inelastically scattered radiation. Figure 2.20 schematically shows the basic principles of scattering.

A scattering process is called elastic if the energy of the scattered waves has the same value as that of the initial beam. However, if the energy changes in a course of interaction with matter, this process is called inelastic. For a wave with the initial energy of $E_i = \hbar\omega$ the corresponding wave vector is given by $\vec{k_i} = \vec{e_i} 2\pi/\lambda$, where $\vec{e_i}$ represents the unit vector in the direction of the incident beam. Scattering by an angle 2θ leads to a change of the scattering vector $\vec{q} = \vec{k_s} - \vec{k_i}$ (see Figure 2.21). In case of inelastic scattering, the length of the scattering vector $\vec{k}$ changes after the interaction with matter ($\mid \vec{k_s} \mid \neq \mid \vec{k_i} \mid$). The following analytical description of the scattering process assumes waves with $\mid \vec{k_i} \mid = \mid \vec{k_s} \mid = k$ for the absolute values of the scattering vector before and after the interaction with matter. Moreover, the main part of the initial radiation penetrates through the sample without interaction, and only a small part is scattered. Multiple scattering processes, with even smaller probability of occurrence, are neglected (Born approximation). A monochromatic plane wave is characterised by the amplitude:

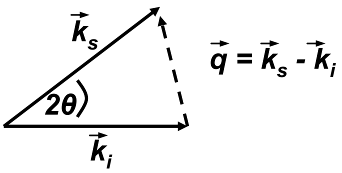

Figure 2.21: The definition of the scattering vector $\vec{q}$.

$$A_i(\vec{r}, t) = A_0 e^{[i(\vec{k_i}\vec{r} - \omega t)]}. \tag{2.24}$$

The amplitude of the scattered wave A_s has the same angular frequency $\omega = 2\pi\nu$ and wavelength $\lambda = h/p$, where $p = \mid \vec{p} \mid = \mid \hbar\vec{k} \mid$ represents the momentum of the wave. The scattering vector $\vec{q}$ introduced in Figure 2.21 is related to the scattering angle by:

$$q \equiv \mid \vec{q} \mid = \frac{4\pi}{\lambda} sin\theta. \tag{2.25}$$

The interaction of a plane wave with N discrete scattering objects is described by Huygens-Fresnel principle. According to that, each of the scattering objects emits a spherical wave, which then coherently add up forming the scattering wave front. Hence, the total scattering amplitude is the sum of the waves scattered by individual scattering objects (e.g. atoms, molecules or clusters). In the context of Fraunhofer (far field) approximation these waves can be treated as plane waves at the detector position. Combining both concepts, the measured scattering amplitude A_s at the detector position $\vec{R}$ is described in the following way:

$$A_s(\vec{R},t) \simeq \frac{A_0}{R} e^{i(kR-\omega t)} \sum_{j=1}^{N} a_j(\vec{q}) e^{-i\vec{q}\vec{R}_j}, \tag{2.26}$$

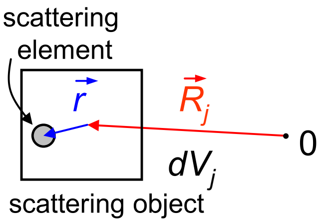

Figure 2.22: A spatially extended scattering object.

where R is the sample-detector distance (being much larger than the sample size), and $a_j(\vec{q})$ is the scattering amplitude of a single *scattering object* j (e.g. an atom, a molecule or a larger particle). The position of the particular scattering object j within the entire scattering volume V is given by the vector $\vec{R}_j$ (position of the centre of mass).

The local position of a *scattering element* (an electron or a nucleus) within the object volume $dV_j(= d^3r)$ is $\vec{r}$ (relative to the centre of mass position). The situation of a spatially extended scattering object is visualised in Figure 2.22. The scattering amplitude of a single scattering element is the so-called *scattering length* $b(\vec{r})$ and, in contrast to $a_j(\vec{q})$, it does not depend on the scattering vector $\vec{q}$. The sum in the scattering amplitude in Equation 2.26 is characterised by the scattering amplitude $a_j(\vec{q})$ of a single object j and a phase factor. The former quantity gives by the distribution of the scattering elements within the object. The latter one gives the spatial correlation of the objects within the entire sample. In order to understand the scattering process it is helpful to start with the former quantity. The scattering amplitude of a scattering object is given by:

$$a_j(\vec{q}) = \int\limits_{V_j} \rho(\vec{r}) e^{-i\vec{q}\vec{r}} d^3r, \tag{2.27}$$

where $\rho(\vec{r})$ is the *scattering length density* (sld) of an element at $\vec{r}$. It can be understood as the local density of the scattering elements, since the scattering magnitude for each scattering element is determined by $b(\vec{r})$, and it depends on both, the type of the scattering element and the type of radiation, respectively. The relation between ρ and b is introduced later in subsection 2.4.3, where the differences of the scattering processes of X-rays and neutrons will be discussed. There is no scattering in homogeneous media. The so-called *scattering contrast* $\Delta\rho$ is the *difference* between the sld of the scattering element at $\vec{r}$ and the mean value of the entire radiated sample volume.

Taking an example of a two-phase system consisting of homogeneous spherical scattering objects in a liquid ($\Delta\rho(\vec{r}) = \Delta\rho$), the amplitude from Equation 2.27 becomes [Pedersen, 1997]:

$$\begin{aligned} a_{sphere}(\vec{q}) &= \Delta\rho \int_{sphere} e^{-i\vec{q}\vec{r}} d^3r, \\ \rightarrow a_{sphere}(q) &= \Delta\rho \frac{3}{(qR)^3}(sin(qR) - qRcos(qR))\frac{4}{3}\pi R^3 \\ &= \Delta\rho Z(qR)\frac{4}{3}\pi R^3. \end{aligned} \tag{2.28}$$

Here R is the radius of the spherical scattering object, and the function $Z(qR)$ is given by $Z(qR) = 3j_1(qR)/(qR)$, where $j_1(qR)$ is the *spherical* Bessel function of the first kind. Introducing the volume of a sphere by $V_{sphere} = 4/3\pi R^3$ Equation 2.28 can also be written as:

$$a_{sphere}(q) = \Delta\rho F_{sphere}(q) V_{sphere}, \tag{2.29}$$

with $F_{sphere}(q)$ being the *form factor* of the spherical scattering object. It is defined by $F(q) =\mid a(q) \mid / \mid a(0) \mid$ so that $F(q) \rightarrow 1$ as $q \rightarrow 0$, and it provides information on the shape of the scattering particle. For a number N of nested spherical shells the form factor also includes the scattering contrast of the particular shell, since $\Delta\rho(\vec{r}) \neq \Delta\rho$. It is expressed by [Pedersen, 1997]:

$$F_{shells}(q) = \frac{\sum_{i=1}^{N}(\rho_i - \rho_{i-1})R_i^2 Z(qR_i)}{\sum_{i=1}^{N}(\rho_i - \rho_{i-1})R_i^2}, \tag{2.30}$$

where ρ_i is the sld and R_i the radius of the i-th shell, respectively, starting from the outermost shell. In analogy to the case of a sphere the corresponding form factor for a cylinder of infinite length is derived by a separation of the length and the cross-section terms in the integration of Equation 2.27. In that case the function $Z(qR)$ in Equation 2.28 and Equation 2.30 is given by $Z(qR) = 2J_1(qR)/(qR)$, where $J_1(qR)$ is the Bessel function of the first kind. The scattering intensity (see next paragraph) has then to be normalised by the so-called *Lorentz factor* $1/q$ [Glatter & O.Kratky, 1982].

In a scattering experiment the *scattering intensity* is measured rather than the amplitude. Since these two quantities are related by $I(\vec{q}, t) =\mid A(\vec{q}, t) \mid^2$, the measured intensity does not contain information about the phase of the wave in Equation 2.26. This is the so-called *phase problem*. Taking Equation 2.26 for identical homogeneous spherical scattering particles the scattering intensity can be written as (omitting pre-factors):

$$I_s(\vec{q}) = a^2(q) \sum_{j=1}^{N} \sum_{k=1}^{N} e^{-i\vec{q}(\vec{R}_j - \vec{R}_k)} \tag{2.31}$$

$$\approx K(\Delta\rho)^2 \mid F(q) \mid^2 S(\vec{q}), \tag{2.32}$$

where $K = NV^2$ is a constant factor, determined by the number and the volume of the particles, $(\Delta\rho)^2$ is the square of the scattering contrast, and $S(\vec{q})$ is the *structure factor*, which represents the modification of the intensity from initially uncorrelated particles due to their spatial correlation. In a dilute system with uncorrelated positions of the scattering objects $S(\vec{q}) = 1$. For concentrated systems, such as a liquid, these spatial correlations, are usually described in terms of the so-called *radial distribution function*, or the *pair correlation function* $g(R)$. It gives the probability of finding the centre of any particle at a distance R from the centre of a given particle [Lindner & Zemb, 2002]. If the total number of particles is N within the volume V, the number of particles in a volume element dV at a distance R from a given particle is $(N/V)g(R)dV$. For liquids the relation between the structure factor $S(q)$ and the pair correlation function $g(R)$ is expressed by:

$$S(q) = 1 + 4\pi \frac{N}{V} \int_0^\infty [g(R) - 1] R^2 \frac{sin(qR)}{qR} dR \tag{2.33}$$

Fourier inversion of Equation 2.33 gives the pair correlation function in terms of the structure factor:

$$g(R) = 1 + \frac{1}{2\pi^2} \frac{V}{N} \int_0^\infty [S(q) - 1] q^2 \frac{sin(qR)}{qR} dq \tag{2.34}$$

2.4.2 Diffraction

A special case of scattering is that of periodically arranged particles. A crystal is characterised by a periodic arrangement of identical basic elements on a lattice. These basic elements can either be single atoms, molecules or even larger objects, such as pores, clusters, or polymers. For every lattice one can define a unit cell with three basic unit vectors $\vec{a}_1$, $\vec{a}_2$, $\vec{a}_3$, and a lattice vector $\vec{T}_{uvw} = u\vec{a}_1 + v\vec{a}_2 + w\vec{a}_3$, where u, v and w are integer numbers. Every basic element can now be represented as a linear combination of these three lattice vector components. Any three-dimensional crystal can be described by one of 14 different, the so-called *Bravais lattices*. In order to distinctly define a *plane* of a crystal the so-called *Miller indices* are used. Regarding the case of cubic symmetry, a lattice vector with the direction $[hkl]$ is perpendicular to the plane with the corresponding Miller indices (hkl), where h, k and l are integer numbers.

An alternative approach in order to describe lattice vectors is defining the so-called *reciprocal lattice vectors* ($\vec{b}_1$, $\vec{b}_2$, $\vec{b}_3$). Their definition requires $\vec{a_i}\vec{b_j} = 2\pi\delta_{ij}$, ($\delta_{ij}$ - Kronecker delta, $\delta_{ij} = 1$ for $i = j$, and $\delta_{ij}= 0$ for $i \neq j$). The next section will show that the reciprocal lattice is very useful for the description of diffraction phenomena. Without the limitation to cubic symmetry, any reciprocal lattice vector with the direction $[hkl]$ is perpendicular to the plane with the corresponding Miller indices (hkl). For the case of scattering on a simple monoatomic crystal the radial distribution function is a set of delta-functions $g(\vec{R}) = \sum_{ij} \delta(\vec{R} - \vec{T}_i + \vec{T}_j)$ and the structure factor from Equation 2.32 has the form:

$$S_{crystal}(\vec{q}) =\mid \sum_{hkl} e^{-i\vec{q}\vec{T}_{hkl}} \mid^2 . \tag{2.35}$$

For crystals containing different atoms in the basis, the different scattering amplitudes have to be considered by introducing the *atomic form factor* f_{hkl} (detailed definition is given later in subsection 2.4.3) within the sum in Equation 2.35. This sum is only different from zero if the the scalar product $\vec{q}\cdot\vec{T}_{hkl}$ is an integer multiple of 2π. This leads to the so-called *diffraction condition*:

$$\vec{q} = \vec{G}_{hkl}, \tag{2.36}$$

with $\vec{G}_{hkl} = h\vec{b}_1 + k\vec{b}_2 + l\vec{b}_3$ and $\mid \vec{G}_{hkl} \mid= 2\pi/d_{hkl}$ is the reciprocal lattice vector (Figure 2.23).

The diffraction condition can be plausibly illustrated in the picture of the Ewald sphere in Figure 2.24. The incoming wave the vector $\vec{k}$ points to the origin of the reciprocal lattice. The radius of the sphere is given by the length of the wave vectors $\vec{k}$ and $\vec{k}'$, respectively. Hence, $\vec{q}$ can only reach points on the surface of the sphere. The diffraction condition is fulfilled only if $\vec{k}'$ is equal to a reciprocal lattice point. This can be performed either by rotating the sample, or the detector. Sample rotation induces rotation of the reciprocal lattice around the origin. Detector rotation by the angle 2θ rotates $\vec{k}'$ along the Ewald sphere.

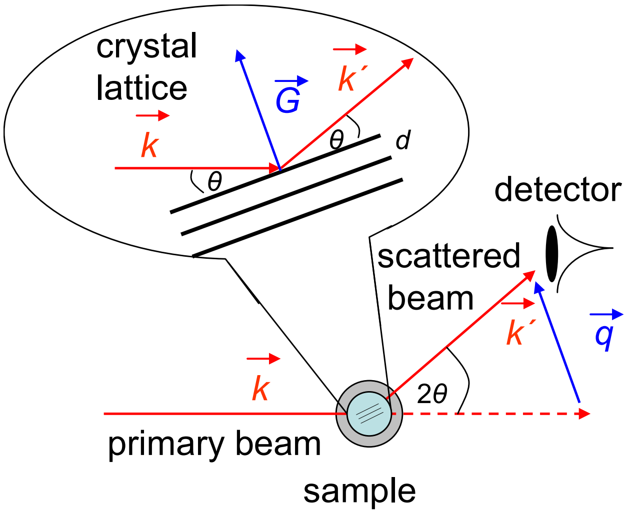

Figure 2.23: Principle of diffraction on a lattice. The mirror condition requires the angle symmetry between the lattice plane and the two scattering vectors $\vec{k}$ and $\vec{k}'$.

The reciprocal lattice of a crystal can directly be measured in a diffraction experiment. If the mirror condition is fulfilled (see Figure 2.23) one can combine the diffraction condition with the definition of q in Equation 2.25. The result leads to the so-called *Bragg law*:

$$2d_{hkl}sin\theta = \lambda \tag{2.37}$$

For an arbitrary crystal the scattered intensity derived from Equation 2.26 at the position of a Bragg peak can by written as:

$$I_s(\vec{G}_{hkl}) = \frac{I_0}{R^2} \mid \sum_j a_j e^{-i\vec{G}_{hkl}\vec{T}_j} \mid^2 \tag{2.38}$$

Measuring intensities of different Bragg peaks allows to determine values for a_j and $\vec{T}_j$, giving the types and positions of atoms in the unit cell of a crystal. Regarding the case of simple cubic symmetry with the lattice constant d gives $q_{hkl} = 2\pi\sqrt{h^2+k^2+l^2}/d$ for the position of the observed (hkl)-Bragg peak. For scattering objects which are perfectly ordered in a two-dimensional hexagonal lattice with the lattice constant d, constructive interference is observed at following scattering vectors:

$$q_{hk} = \frac{4\pi}{d\sqrt{3}}\sqrt{h^2+k^2+hk}. \tag{2.39}$$

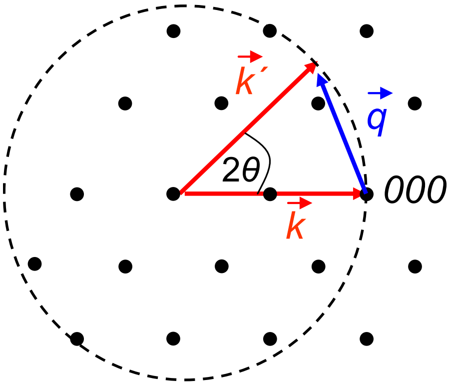

Figure 2.24: The concept of the Ewald sphere requires the vector $\vec{k}'$ to point on a reciprocal lattice point in order to fulfill the diffraction condition.

For powder samples the reciprocal lattice points in Figure 2.24 are not fixed points as for a single crystal, but they are distributed on *spherical shells*. Therefore, for powders, an intersection of the reciprocal lattice-shells with the Ewald sphere are fulfilled without any further rotation of the sample. Thus, there is always an optimally oriented crystallite leading to a spot on the detector at the corresponding diffraction angle 2θ. The resulting two-dimensional scattering pattern of a powder or a polycrystal typically contains a number of concentric rings (*Debye-Scherrer method*). Every point on such ring corresponds to a particular diffraction angle, for which the Bragg condition is fulfilled.

This distribution of the reciprocal lattice points has another important consequence for scattering data analysis from powdery samples. For the analytical scattering curve description of a powder containing cylindrical scattering objects, the factor $1/q^2$ has to be taken into account [Imperor-Clerc, 2000, Zickler, 2006]. This correction already includes the Lorentz factor for cylinders introduced in the previous sub-section. The number of reflections contributing to the total ring intensity strongly depends on the symmetry of the lattice [Guinier, 1994]. Reflections can be produced by more than only one (hkl) lattice plane. Therefore, the so-called multiplicity factor M_{hkl} for the particular reflection has to be taken into account. Some selected values for a hexagonal lattice symmetry are summarised in Table 2.2.

indices	M_{hkl}
$h00$	6
$hh0$	6
$hk0$	12

Table 2.2: Multiplicity factors for a hexagonal lattice.

2.4.3 X-rays and neutrons

The general analytical descriptions of elastic scattering derived within the previous two subsections are valid for all types of radiation, such as photons, neutrons or electrons. All radiation types are characterised by their energy $E = \hbar\omega$ and the momentum of their particles $\vec{p} = \hbar\vec{k}$. For radiation consisting of mass particles, such as neutrons or electrons, the values for E and p can alternatively be calculated using well-known equations from the mechanics: $E = mv^2/2$ and $p = mv$ (with $m = m(v)$ for $v \to c$). Since photons have zero mass, their energy corresponds to $E = hc/\lambda$ and their momentum is $p = h/\lambda$. As already mentioned earlier, the different types of radiation interact differently with matter. X-rays interact with atomic electrons and neutrons essentially with their nuclei (magnetic neutron scattering by the electrons is not considered within this context). A first important consequence is that different types of radiation get differently *absorbed* on the way through a sample with thickness x. The ratio between the outgoing intensity in forward direction $I(q = 0)$ and that of the incoming beam I_0 is the transmission of the sample τ, defined by:

$$\tau = \frac{I(q = 0)}{I_0} = e^{-\mu x}, \tag{2.40}$$

where μ is the linear *attenuation coefficient* (see Figure 2.25).

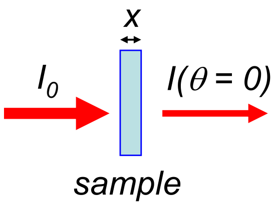

Figure 2.25: Transmission through a sample.

The values for μ depend on both, the sample material and the radiation type. In general, the attenuation coefficient is the sum of absorption, coherent and incoherent scattering. For X-rays it depends on the energy and the number of electrons in the atom ($\mu_{X-rays} \propto Z^4/E^3$). The tabulated values for different materials and energies can be found in Ref. [CSRRI, 2012]. Attenuation coefficient for X-rays strongly increases if the energy is near the binding energy of an electron within the sample atom. This property is used in absorption spectroscopy methods [Koenigsberger & Prins, 1988]. For neutrons, absorption is often accompanied by a nuclear reaction. Thus, some samples may be radioactive after a neutron experiment. Neutron absorption coefficient values scale with the neutron wavelength. Tabulated values for $\mu_{neutrons}$ for different materials can be found in Ref. [NIST, 2011].

For all types of radiation the attenuation coefficient is proportional to the density of the studied material. In order to calculate the actual value of attenuation for a material with the mass density ρ_m one uses tabulated values for the energy-dependent *mass attenuation coefficient* μ/ρ_m and multiplies with the corresponding material density. Thus, for quantitative density measurements appropriate data correction is important. Note further, that in order to minimise multiple scattering the choice of sample thickness with $x \ll 1/\mu$ is necessary.

The scattering intensity in Equation 2.32 is proportional to the square of the scattering contrast $(\Delta\rho)^2$. Due to the different interaction processes of radiation with matter, the magnitude of this quantity differs for different radiation types. Except for energies near the atomic electronic transitions, the scattering of X-rays occurs as if the electrons were free. For a single electron the magnitude of the scattering strength is characterised by the *scattering length of an electron* $b_e = r_e = e^2/m_e c^2 = 2.81 \cdot 10^{-15}$ m. It corresponds to the scattering amplitude of a single electron in forward direction (the detailed description is given in the chapter by G. Porod in Ref. [Glatter & O.Kratky, 1982]). Using the previously defined scattering amplitude of a scattering object in Equation 2.27 one obtains $a_e(q = 0) = b_e$. For an atom with Z electrons this scattering amplitude is $a(0) = b = Zb_e$, where b is the scattering length of the atom, introduced in subsection 2.4.1. Atoms with small atomic numbers scatter less than those with large Z. Consequently, the scattering contrast $\Delta\rho$ of an atom in vacuum is simply given by its own sld, defined by $\rho = b/V$. For X-rays there is no influence on the scattering behaviour if the scattering atom is replaced by its isotope, hydrogen by deuterium, for instance. Since typical X-ray wavelengths are in the dimension of an atomic electron cloud ($\sim 10^{-10}$ m), the scattering lengths values show some dependence on the scattering vector $\vec{q}$. This dependence is described in terms of the *atomic form facto*r $f(\vec{q}) = \int \rho(\vec{r}) exp(-i\vec{q}\vec{r}) d^3r$, (compare with Equation 2.27 for the scattering amplitude of a single electron in vacuum). Consequently, $f(0) = a(0) = Zb_e$. The values for $f(q)$ for different atoms and scattering vectors are tabulated in Refs. [Pecharsky & Zavalij, 2009, Ruppweb, 2012]. In this thesis the X-ray scattering amplitude was quantitatively analysed only at small scattering vectors. Therefore, the corresponding atomic form factors for X-rays are approximated by those in forward direction.

In contrast to the case of X-rays, values for neutron scattering lengths vary irregularly with the type of atoms. Some atoms are even characterised by negative values for the neutron scattering length, which corresponds to a phase shift of π radians during a scattering process. Different isotopes can have distinctly different scattering lengths. A prominent example is that of hydrogen and deuterium. The scattering length of a proton (hydrogen nucleus) is negative, and that of deuterium is positive. Consequently, a partial deuteration of aqueous samples leads to distinct changes of the neutron contrast, without a serious affection of their chemical properties. Another important difference between neutrons and X-rays is the angular dependence of the corresponding atomic form factors $f(\vec{q})$ (or $a(\vec{q})$ from Equation 2.27). Since the size of a nucleus is much smaller than that of a typical neutron wavelength, the neutron atomic form factors are independent on the value of the scattering vector , giving $f(\vec{q}) = b \int \delta(\vec{r}) exp(-i\vec{q}\vec{r}) d^3r = b$.

Since the magnitude of atomic scattering was shown to be characterised by their scattering lengths, the sld of a molecule consisting of different atoms can be introduced by:

$$\rho = \frac{\rho_m N_A}{M} \sum_i n_i b_i, \tag{2.41}$$

where N_A is the Avogadro number, M is the molar mass, ρ_m is the mass density, and n_i and b_i are the number and the scattering length of the atomic species i in the molecule, respectively. The corresponding sld values for water (H_2O), heavy water (D_2O) and for silica (SiO_2) at $T = 277$ K and ambient pressure are summarised in Table 2.3.

	mass density ρ_m [g/cm^3]	sld ρ (X-rays) [10^{-6}Å^{-2}]	sld ρ (neutrons) [10^{-6}Å^{-2}]
H_2O	1.00	9.46	-0.56
D_2O	1.105	9.41	6.36
SiO_2	2.20	18.9	3.47

Table 2.3: Scattering length densities for neutrons and X-rays. Values are taken from [NIST, 2011].

The contrast variation by isotopic substitution constitutes one important advantage of neutron scattering. Also the angle-independent values for the atomic scattering lengths make neutron scattering suitable for measurements at large scattering angles. The corresponding X-ray scattering lengths can get very small at large scattering angles (see e.g. Ref. [Ruppweb, 2012]). Magnetic interaction with the electron spin makes neutrons also well suitable for measurements of magnetic properties for different materials [Shull & Smart, 1949]. Good energy resolution ($\Delta E/E$) also allows dynamic measurements with neutrons [Mezei, 1972]. The main advantage of using X-ray radiation is the large flux of particles compared to that of a typical neutron source. For X-rays it is also possible to change the scattering contrast, e.g. by means of anomalous small-angle X-ray scattering (ASAXS). This method implies the change of the primary beam energy around the electronic transition of the studied matter [Stuhrmann, 1985]. There several other important advantages of using neutrons or X-rays. Describing all of them would go far beyond their actual application within this thesis.

2.4.4 Small-angle and wide-angle scattering

The method of diffraction presented in subsection 2.4.2 in most cases is used for the analysis of crystal lattices, where the distance d between the scattering objects is of the same dimension as the radiation wavelength usually used in experiments. Within this context often the term *diffraction* is used. For scattering objects, which exhibit larger distances between each other, such as large molecules, polymers or pores, the corresponding scattering angles become very small. For scattering objects with $d \gg \lambda$ usually the term *small-angle scattering* is used. This term is also applied to studies of disordered systems resulting in the analysis of diffuse scattering at very low angles [Glatter & O.Kratky, 1982, Brumberger, 1995]. In contrast, diffraction is then called *wide-angle scattering* (see Figure 2.26).

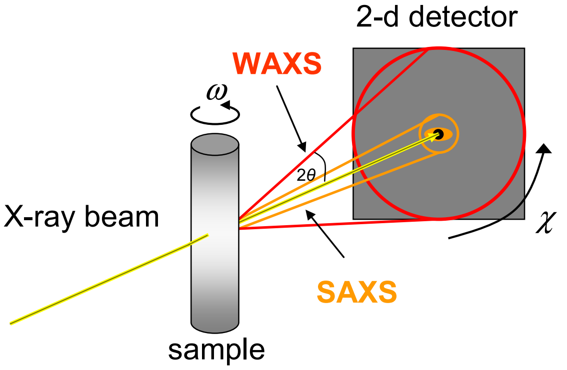

Figure 2.26: X-ray scattering: SAXS vs. WAXS. Primary beam is denoted yellow.

Within this thesis scattering experiments were performed on water-filled porous samples. These powdery samples are characterised by well-ordered structure of mesopores with diameters of some nanometers (see section 2.3). The scattering signal from this mesoporous structure was measured at low scattering angles. On the other hand, the structure of water, characterised by intermolecular distances of some Ångströms, was measured at large scattering vectors. Thus, the region of small-angle scattering and that of wide-angle scattering denote scattering contributions from these two well-separated spatial regions.

Small-angle scattering

This thesis includes the application of both small-angle scattering methods, i.e. with X-rays (*SAXS*) and with neutrons (*SANS*). The scattering objects are cylindrical pores with distances ranging between 2.5 nm and 11.7 nm, depending on the used material (see section 2.3). The corresponding structure factors and form factors, introduced in the previous sections are applied on the distribution and shape of these new scattering objects, i.e. the pores. Hereby, the scattering on empty pores within the silica matrix takes place according to the *Babinet's principle.* Small-angle scattering of hexagonal ordered cylindrical mesopores can be expressed by Equation 2.32. The structure factor $S(q)$ of the pores depends on their spatial arrangement. For the given case of perfectly arranged cylinders in a two-dimensional lattice, the structure factor gives non-vanishing intensity only at the positions of the individual Bragg reflection described by Equation 2.39, giving $S(q_{hk}) = 1/q_{hk}^2$, essentially the Lorentz factor of a powder containing cylindrical scattering objects [Imperor-Clerc, 2000, Zickler, 2006]. The structure factor is zero otherwise. However, due to the finite pore size distribution and a finite experimental resolution, in a real experiment these sharp peaks (ideally delta functions) are broadened and can be represented by Gaussian or Voigt functions [Zickler, 2006]. Broadening of Bragg reflections is also affected by the size of the investigated crystal by FWHM$\propto 2\pi/D$ (Scherrer equation, FWHM - full-width of half maximum of the peak, D - crystal size). Especially for very small lattice sizes this effect has to be taken into account. Thermal lattice distortions, usually considered by a Debye-Waller factor are not taken into account within this study. For the form factor $F(q)$ of the pores the scattering amplitude of a cylindrical cross section is used. It is given by Equation 2.30 for cylinders, and determines the relative intensity of the Bragg peaks. The data analysis within this thesis includes some important relations, which are introduced in the following:

For a system of two phases with sharp interfaces (e.g. solid particles in a liquid) *Porod's law* can be applied in order to describe the asymptotic behaviour of radially averaged scattering intensity of a powder. Hereby, the asymptotic case is given by $qd \gg 1$, where d denotes the length scale of sample inhomogeneities:

$$\lim_{q\to\infty} I_s(q) = \frac{2\pi(\Delta\rho)^2 A}{q^4} + B. \tag{2.42}$$

A is the sample surface per unit volume (internal and external, compare with the first section in subsection 2.2.4) and B is a background, which is usually constant (due to the incoherent contribution in a neutron scattering process, for instance). The numerator of the first term in Equation 2.42 is often denoted as the *Porod constant* P. A plot of $I_s(q)q^4$ versus q^4 is linear for large values of q. The intercept with the Iq^4-axis gives the value of the Porod constant, the slope of the straight line is the q-independent scattering background. The so-called *Porod-plot* has the form:

$$I_s(q)q^4 = P + Bq^4 \tag{2.43}$$

The detailed derivation of Equation 2.42 can be found in the reference book [Lindner & Zemb, 2002]. An important quantity for analysis of scattering experiments is the so-called *integrated intensity* $\bar{Q}$ [Porod, 1951]. The integration of the scattered intensity over the whole q-space gives a constant value [Glatter & O.Kratky, 1982]:

$$\frac{1}{4\pi}\int I_s(\vec{q})d^3q = \int_0^\infty I_s(q)q^2dq \equiv \bar{Q} \tag{2.44}$$

with

$$\bar{Q} = 2\pi^2 \left\langle \eta^2 \right\rangle, \tag{2.45}$$

where $\langle \eta^2 \rangle = \langle \rho^2 \rangle - \langle \rho \rangle^2$ indicates the average square fluctuation of the scattering length density ρ. For a system only composed of two phases, one with volume fraction ϕ, and the other with $(1-\phi)$, the corresponding (scattering length) densities are ρ_1 and ρ_2 , respectively. The integrated intensity $\bar{Q}$ is proportional to the scattering contrast of this two-phase system, yielding an important experimental formula:

$$\bar{Q} = 2\pi^2 \phi(1-\phi)\Delta\rho^2. \tag{2.46}$$

For a three-phase system with the volume fractions $\phi_1 + \phi_2 + \phi_3 = 1$, the corresponding description of the integrated intensity $\bar{Q}$ has the form [Peterlin, 1965, Ciccariello & Benedetti, 1985]:

$$\begin{aligned} \bar{Q} = 2\pi^2[(\rho_1 - \rho_3)^2\phi_1(1-\phi_1) + (\rho_2 - \rho_3)^2\phi_2(1-\phi_2) \\ - 2(\rho_1 - \rho_3)\phi_1(\rho_2 - \rho_3)\phi_2]. \end{aligned} \tag{2.47}$$

Application of these equations to the experimental data has to be done with care. Experimentally $\bar{Q}$ is determined by numerical integration of the measured quantity $I_s(q)q^2$, after subtracting a sample-related constant scattering background. The background is usually determined by a fit with Porod's law (Equation 2.42). Further an extrapolation of the scattering intensity to low and high scattering vectors is required. Usually, the low-q contribution is approximated by assuming a constant scattering intensity $I_{smin} = I_s(q_{min})$ for $q < q_{min}$, where q_{min} corresponds to the lower limit of the experimental data. The high-q contribution to $\bar{Q}$, for $q > q_{max}$ is usually determined by an extrapolation of $I_s(q)$, again, on the basis of Porod's law (Equation 2.42). The total experimental integral intensity can be written in the following form:

$$\bar{Q} = I_s(q_{min}) \cdot q_{min}^3 + \int_{q_{min}}^{q_{max}} I_s(q)q^2 dq + \frac{P}{q_{max}}. \tag{2.48}$$

The application of Equation 2.48 is illustrated in Figure 2.27.

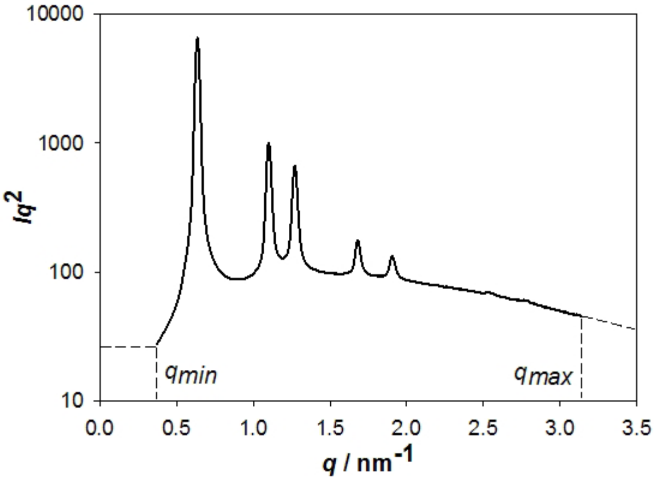

Figure 2.27: Experimental scattering pattern of SBA89 (the background was corrected using Equation 2.43) The integrated intensity $\bar{Q}$ is given by the area below the experimental and the extrapolated curves.

Wide-angle scattering

In this thesis wide-angle X-ray scattering (WAXS) is applied in order to monitor the intermolecular structure of water molecules. For liquid water at room temperature the structure factor from Equation 2.33 has a prominent peak situated at $q = 19.5$ nm^{-1} [Czihak, 2000] (see also Figure 2.28). Bulk ice is characterised by the following lattice parameters [Dowell & Rinfret, 1960, Schulson, 1999]: $a = 4.52$ Å, $c = 7.37$ Å for hexagonal ice (I_h) and $a = 6.35$ Å for cubic ice (I_c). The scattering angles for Cu $K - \alpha$ X-ray radiation line ($\lambda = 1.5425$ Å) [Lide, 1992] are shown together with the corresponding scattering vectors in Table 2.4.

Scattering angle 2θ [°]	Scattering vector q [nm^{-1}]	Bragg peak order I_h	Bragg peak order I_c
22.70	16.04	(100)	-
24.27	17.14	(002)	(111)
25.76	18.17	(101)	-
33.40	23.42	(102)	-
39.87	27.79	(110)	(220)
43.49	30.19	(103)	-

Table 2.4: Bragg peak positions for hexagonal and cubic ice. The scattering angles are given for Cu $K - \alpha$ radiation. The corresponding scattering vectors are also given. Values taken from [Murray, 2005, Pineri, 2007].

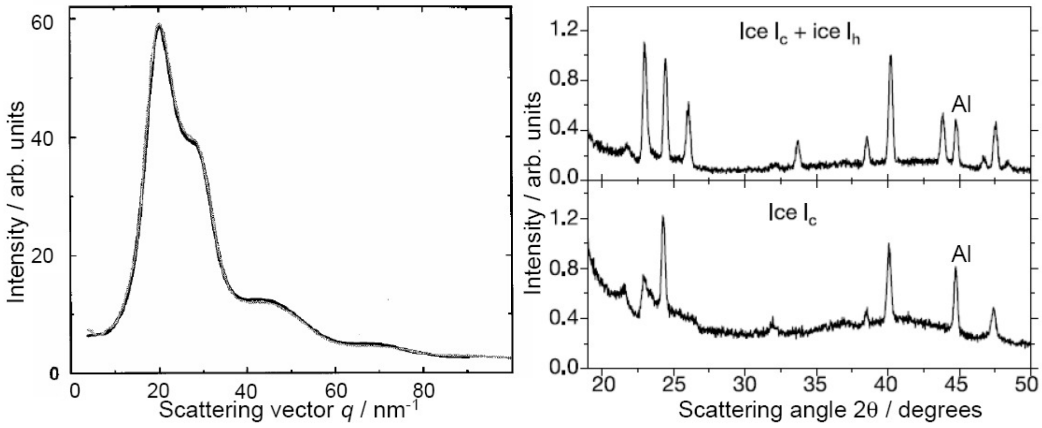

Figure 2.28: Left: experimental X-ray scattering data of liquid water at room temperature [Sorenson, 2000]. Right: experimental X-ray data of hexagonal I_h and cubic I_c ice [Murray, 2005].

2.4.5 Basics of Raman scattering

Beginning with the basic description of atomic and molecular absorption processes, this section introduces Raman scattering, as an alternative approach for studies of dynamical properties of water. The basic description of this method is referred to standard text books [Tipler, 1994], [Stuart & Klages, 1992] and [Hesse, 1991], together with some online references [Chemgapedia, 2011, Lund-University, 2011], and a presentation document from A. Masic [Masic, 2010]. Particularly for the description of Raman scattering of water, sections from an own publication [Erko, 2011] are included.

The quantum behaviour of the energy transfer between radiation and matter is known since the beginning of the 20th century. The photo-effect, discovered by A. Einstein in 1905, and the experiment of Franck and Hertz in 1913 are the best examples for this phenomenon. Similar effects of energy level quantisation can also be found for other atomic properties, taking for instance the magnetic structure determined by electronic or nuclear spin transitions. Thus, a photon gets absorbed if its energy exactly corresponds to the distance between two character-

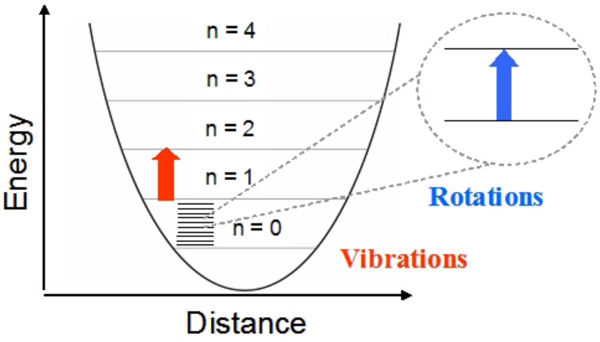

Figure 2.29: Relative energy spacing between molecular rotational and vibrational energy levels visualised by the energy levels of a harmonic oscillator. Figure adapted from [Masic, 2010].

istic energy levels of the atom. The opposite effect of absorption is that of *fluorescence,* which occurs whenever a photon is emitted by an atom upon the change of its energy level. Electronic transitions are in the energy region of ultra-violet light and that of low-energy X-rays. Spin transitions of atomic nuclei are in the range of radio waves, those of electrons are in the region of microwaves. In analogy to an atom also molecules are characterised by characteristic energy levels, determined by their rotational (micro waves, far infra-red (IR)) and vibrational (IR) modes. An arbitrary molecular potential can be approximated by a harmonic potential at the vicinity of a stable equilibrium point. In this picture absorption of a photon results in an excitation of a molecular vibrational mode. The relative spacing of the rotational and vibrational energy levels are visualised schematically in Figure 2.29. Quantum-mechanical solution of the harmonic oscillator gives the quantised energy levels with a non-zero value for the energy of the lowest level:

$$E_n = h\nu(n + \frac{1}{2}), \tag{2.49}$$

with h being the Planck's constant and n is an integer number starting at 0. The distance between vibrational energy levels of a two-atomic molecule can be approximated by $E = h \cdot \sqrt{s/\mu}/2\pi$, where s is the "spring constant" between the two atoms in the molecule and $\mu = (1/m_1 + 1/m_2)^{-1}$ is the effective mass. This spring constant can be understood in terms of the binding energy of the atoms.

The model of a harmonic oscillator is, however, too simplified and can not describe several phenomena, such as the dissociation of molecules, for instance. Different modes can also be characterised by different distances of the energy levels. The curve of an anharmonic oscillator gives a more realistic description of a molecular potential. Beside the quantum condition in Equation 2.49 absorption of infra-red (IR) light by a molecule also requires the change of its dipole moment by the applied electric field. Hence, only those molecular vibrations are IR-*active*, which change the molecular dipole moment. Consequently, for molecules exhibiting a centre of symmetry, symmetric vibrations are IR-*inactive* (see Figure 2.30). A typical IR spectrum is recorded by measuring the rate of absorbed monochromatic photons over a (step-wise) scanned energy range. In contrast to this dispersive method, Fourier-Transform IR-spectroscopy (FTIR) simultaneously collects spectral data in a wide spectral range, and extracts information from the analysis of the obtained interference spectrum. Particularly, the higher signal-to-noise ratio for a given scan-time or a shorter scan-time for a given resolution is the main advantages of the latter method.

An alternative approach for the analysis of molecular vibrations is the inelastic scattering of visible light, the so-called *Raman scattering.* If the energy of the incident beam is beyond molecular vibrational modes the main part of light will be transmitted without interaction with matter. A small part of the incident intensity (typically

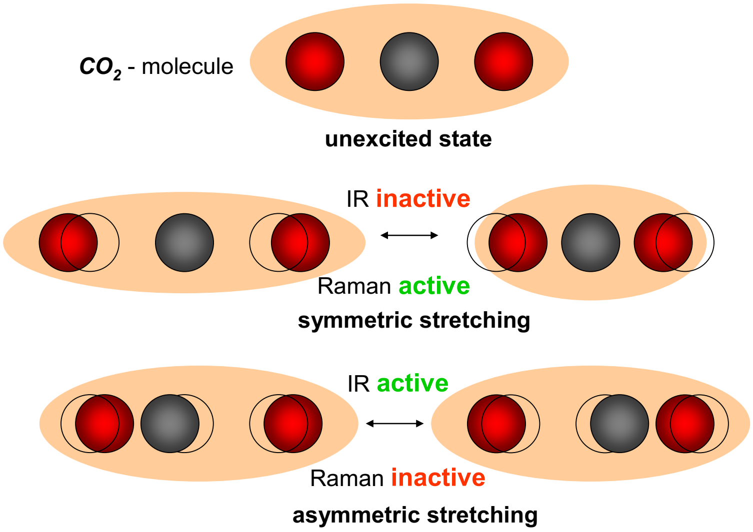

Figure 2.30: Symmetric vibrations are IR-inactive for molecules exhibiting a centre of symmetry, here the CO_2 molecule. A change of the ellipsoid of polarisability (orange) indicates Raman activity of a vibrational mode.

a factor of 10^{-4}) is scattered elastically in all spacial directions (*Rayleigh scattering*). An even smaller portion of the initial intensity (typically a factor of 10^{-8}) is also scattered in all directions, however exhibiting a characteristic energy distribution. The scattered photons are characterised by lower (Stokes) and higher (anti-Stokes) energy values compared to that of the incident beam. This scattering part results from the interaction of photons with phonons, and represents the *emission spectrum* of the studied material (see Figure 2.31). The process is described by an excitation of molecules from their vibrational ground state into a virtual energy level. The subsequent relaxation can either proceed back to the ground state (Rayleigh scattering), or it can terminate at an excited energy level resulting in photon emission with a lower energy compared to that of the incident light (anti-Stokes). The same interaction process leads to the emission of photons with a higher energy if the incident light excites a molecule which is already in an excited state. The difference between the primary energy and the energy distribution of the scattered photons can be regarded as the fingerprint for the vibrational structure of the sample.

While for IR studies a change in dipole moment of the molecule is required, for so-called *Raman active* matter the incident photon induces a change of *polarisability* of the studied molecules. Polarisablity of a molecule gives the extent of possible deformation of the electron cloud under the influence of the electric field. The electrons and the nuclei of the sample atoms are pushed in different directions resulting in a deformation of the molecule. A good illustration of Raman activity is understood in terms of the so-called *ellipsoid of polarisabilty*. The example of the linear CO_2 molecule shows that symmetric vibration results in a change of the polarisability of the molecule (see Figure 2.30). Thus, only symmetric stretching of the linear

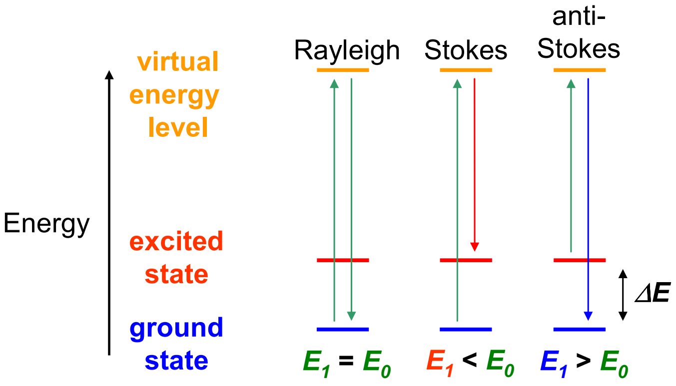

Figure 2.31: Principle of Raman scattering. Green arrows indicate excitation beam and elastically scattered light. Red and blue arrows indicate scattered light with lower (Stokes) and higher (anti-Stokes) energies compared to that of the exciting beam. ΔE gives the vibrational fingerprint of the molecule.

CO_2 molecule can be observed by Raman scattering. For H_2O the corresponding ellipsoid of polarisability is more difficult to visualise. Good illustrations can be found in Ref. [Chemgapedia, 2011]. The water molecule does not exhibit a centre of symmetry. This property is essential for spectroscopic IR and Raman studies on H_2O. Both techniques are regarded to probe the same vibrational energy structure of water [Mallamace, 2007a]. However, distinct quantitative differences between water spectra measured with the two different techniques are present.

The analytical description of the Raman effect implies that a charge shift in the molecule induces a dipole moment $\vec{p}_{ind} = \beta\vec{E}$, where β is the polarisability of the molecule and $\vec{E} = \vec{E}_0 cos(2\pi\nu_0 t)$ is the applied electric field with frequency ν_0. Molecular vibration can be expressed in terms of nuclear displacement by $x = x_0 cos(2\pi\nu_R t)$, where x is a generalised coordinate and ν_R is the resonance frequency. For small distortions one can write $\beta = \beta_0 + (\partial\beta/\partial x)_0 x$ (Taylor series until the linear term). The resultant induced dipole moment has the form

$$\begin{aligned}\vec{p}_{ind} &= \beta\vec{E}_0 cos(2\pi\nu_0 t)\\ &= \beta_0\vec{E}_0 cos(2\pi\nu_0 t) + (\frac{\partial\beta}{\partial x})_0 x_0\vec{E}_0 cos(2\pi\nu_0 t)cos(\nu_R t)\\ &= \beta_0\vec{E}_0 cos(2\pi\nu_0 t) + \frac{1}{2}(\frac{\partial\beta}{\partial x})_0 x_0\vec{E}_0 \left\{cos(2\pi[\nu_0+\nu_R]t) + cos(2\pi[\nu_0-\nu_R]t)\right\}.\end{aligned} \tag{2.50}$$

The first term in Equation 2.50 represents the Rayleigh scattering with the initial frequency ν_0, the second and the third terms are anti-Stokes and Stokes lines, respectively. Analysis of the inelastically scattered part gives information about the vibrational energy structure of the studied material. This structure depends on different parameters, such as the state or the temperature of the sample. The existence of this effect was initially predicted by A. Smekal in 1923 and five years later experimentally observed by the Indian scientist Ch. V. Raman. Together with the IR spectroscopy, Raman scattering has developed to a wide-spread spectroscopic tool within life-, geological-, chemical-, physical-, and other sciences.

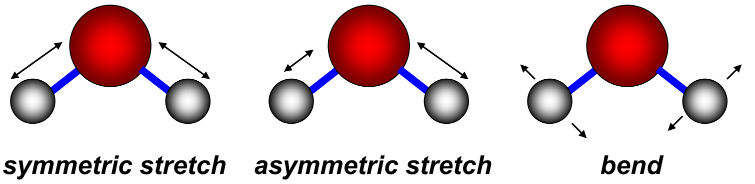

Figure 2.32: Raman-active vibrational modes of water.

This thesis includes the analysis of Raman spectra of water molecules at different temperatures and in different confinement dimensions. As previously mentioned water is one of only few molecules which are both, IR and Raman active. There exist a number of different partially contradictory spectral assignments of the different vibrational modes for water [Sun & Zheng, 2009, Li & Skinner, 2010]. Figure 2.32 shows some characteristic vibrational degrees of freedom for an H_2O molecule. In particular, the broad OH-stretching (OHS) region of water originating from different partially overlapping vibration modes has been analysed in detail and refined over the years for different temperature regions [Walrafen, 1967, Venkatesh, 1975, Sivakumar, 1978b, D'Arrigo, 1981, Sun, 2009]. At room temperature the OHS spectrum of bulk liquid water consists of four peaks: (I) 3250 cm^{-1}, (II) 3420 cm^{-1}, (III) 3545 cm^{-1}, and (IV) 3635 cm^{-1} (the energy is typically presented in *spectroscopic wavenumbers* $1/\lambda = E/hc$ in reciprocal centimetres). The four OHS modes reflect the different intermolecular bonding degrees, ranging from fully HB ones in mode I to the almost free molecules in mode IV [Sun, 2009]. Modes III and IV are most pronounced at high temperatures and decline at lower temperatures [Ratcliffe & Irish, 1982]. For temperatures below 280 K, a new component, mode V, arises at ~ 3100 cm^{-1}, representing the OHS contribution of water molecules forming the ice-like tetrahedral HB network. The occurrence of this "ice-peak" has been attributed to the existence of crystalline ice as heterophase fluctuation in supercooled bulk water [D'Arrigo, 1981].

3 Experimental

This chapter describes the experimental setup conditions for measurements performed within the present thesis. It includes the description of four independent experimental approaches which were used for studying the influence of confinement on the low-temperature properties of water.

Starting with the description of the Raman scattering setup in section 3.1, experimental details of the combined study with X-rays and neutrons are presented in section 3.2. The latter study consists of three independent experiments, i.e. small-angle and wide-angle scattering of X-rays (SAXS and WAXS), and small-angle neutron scattering (SANS). Experimental details for the study of repeated water sorption in SBA-15 are given in section 3.3. An important experimental part of this thesis was the development, construction and commissioning of a new apparatus which allows *in situ* studies of sorption and other phase transitions by means of small-angle X-ray scattering in a laboratory environment. The presentation of this Combined SCattering and ADsorption system (COSCAD's) is given in subsection 3.3.1. Detailed experimental conditions for the study of repeated water sorption in silica are given in subsection 3.3.2.

Parts of the content described here are already published in "Physical Review B" [Erko, 2011], in "Physical Chemistry Chemical Physics" [Erko, 2012a], and in "Journal of Physics: Condensed Matter" [Erko, 2012b]. The respective experimental conditions are described here in more detail than it could be done in the referred journal publications. Some of the text passages in this chapter are identical to those in the publications.

3.1 Raman scattering

The Raman scattering experiments represent a systematic study of confinement effects on the structure of water in the temperature region between 123 K and 293 K. Ordered mesoporous hydrophilic silica MCM-41 and SBA-15 materials with pore diameters ranging from 2.0 to 8.9 nm were used as confining matrices. Samples which were used in this experiment are denoted as MCM20, MCM25, MCM30, MCM34, MCM44, and SBA89 (see section 2.3). Data analysis was performed in two spectral regions attributed to water, i.e. HOH-bending part, and OH-stretching (OHS) part. Spectral position, width, and relative peak area of the components arising within these regions were analysed as a function of temperature and pore diameter.

Figure 3.1: Raman spectrometer Renishaw 1000 at King's College London (left). During measurements the temperature was controlled by the Linkam THS 600 cooling stage (right).

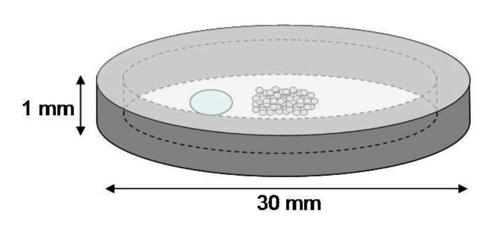

Figure 3.2: Sample cell for Raman measurements. The porous material (grey grains) is enclosed together with a droplet of deionised water (blue) between two glass plates, which are separated by a layer of vacuum grease (dark grey).

The experiments were performed at the Physics Department of King's College London within a Short-Time Scientific Mission provided by ESF COST Action MP0601. The local laboratory equipment provided a Renishaw 1000 Raman spectrometer with a 40× objective (Nikon, ELWD 0.6 NA) (Figure 3.1). Temperature control of the samples was realised by a liquid nitrogen–based Linkam THMS 600 cooling stage operating between 110 and 310 K. Each sample was enclosed in a glass sample cell inside the cooling stage, surrounded by a nitrogen atmosphere. The pore space of the silica powder samples was filled with deionised water at ambient pressure from the saturated vapour phase. The sample cell was made of two thin glass plates with 100 µm thickness and 3 cm diameter. A 1 mm thick layer of temperature-resistant vacuum grease was peripherally applied on the edges of one glass plate. A small amount of mesoporous powder material and a droplet of deionised water were placed in the middle of the glass plate. The second glass plate was pushed on top of the first one, and slightly twisted, enclosing the sample together with the water droplet within a water-saturated atmosphere (Figure 3.2). The specific amount of water required to completely fill the pore space is known from earlier adsorption experiments [Jahnert, 2008b, Erko, 2010]. This amount was considered by the preparation of each experiment in order to minimise the amount of bulk water outside the pores.

One cooling cycle and one heating cycle were performed for each sample in the temperature range between room temperature and 123 K. Unfortunately, measurements at lower temperatures were prevented by enhanced vibrations of the sample cell, arising at high nitrogen pump rates. The cooling/heating rate was 1 K/min. Raman spectra were recorded at constant temperature in steps of 5 K after temperature equilibration of three minutes per measurement point. As a reference, a measurement with a single water droplet representing the bulk water state was performed under exactly the same experimental conditions as those used for water confined in nanopores.

The samples were illuminated with a green laser (Innova 70C, $\lambda = 514$ nm) at 300 mW. Illumination of accumulated powder batches induced an intensive fluorescence background. Another difficulty was the optimisation of the focal distance of the lens system on the actual hight of the sample. These difficulties were solved by illuminating well-separated flat clusters of MCM-41/SBA-15 (see Figure 3.3).

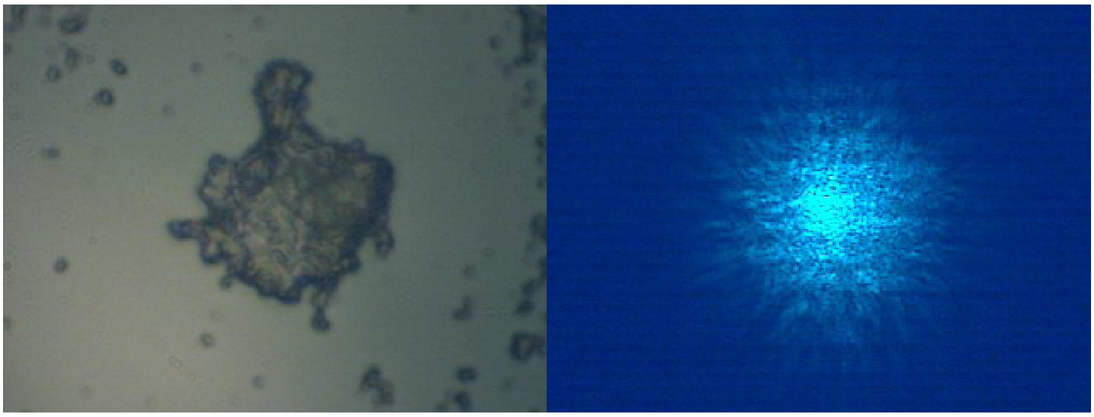

Figure 3.3: Optical picture of the MCM25 material through the 40× objective without (left) and with laser illumination (right).

Raman scattering measurements were performed at ambient pressure in the spectral region between 100 and 4200 cm^{-1} . Spectra were recorded with a charge-coupled device camera at a resolution of 1 cm^{-1}, with a total exposure time of 215 s for each spectrum. Renishaw Wire 3.1 software was used for the primary data correction. Hereby, no additional smoothing of the spectra was performed. A polynomial of the second degree was used for baseline correction (see Figure 3.4).

Peak analysis was performed by the same software using Gaussian curves for all spectral components arising in the spectral region around 1600 cm^{-1}, and between 2800 and 3700 cm^{-1}. The region around 1600 cm^{-1} is the HOH-bending region of water characterised by one single component (see subsection 2.4.5). For the OHS region between 3100 and 3700 cm^{-1} at room temperature four overlapping peaks are expected. The origin of the two sharp peaks between 2900 and 3000 cm^{-1} is discussed later. During the analysis process these peaks were fitted by two additional Gaussian curves at 2910 cm^{-1} and at 2970 cm^{-1}, respectively. The data analysis started with the spectrum obtained for bulk water droplet at room temperature. Tabulated

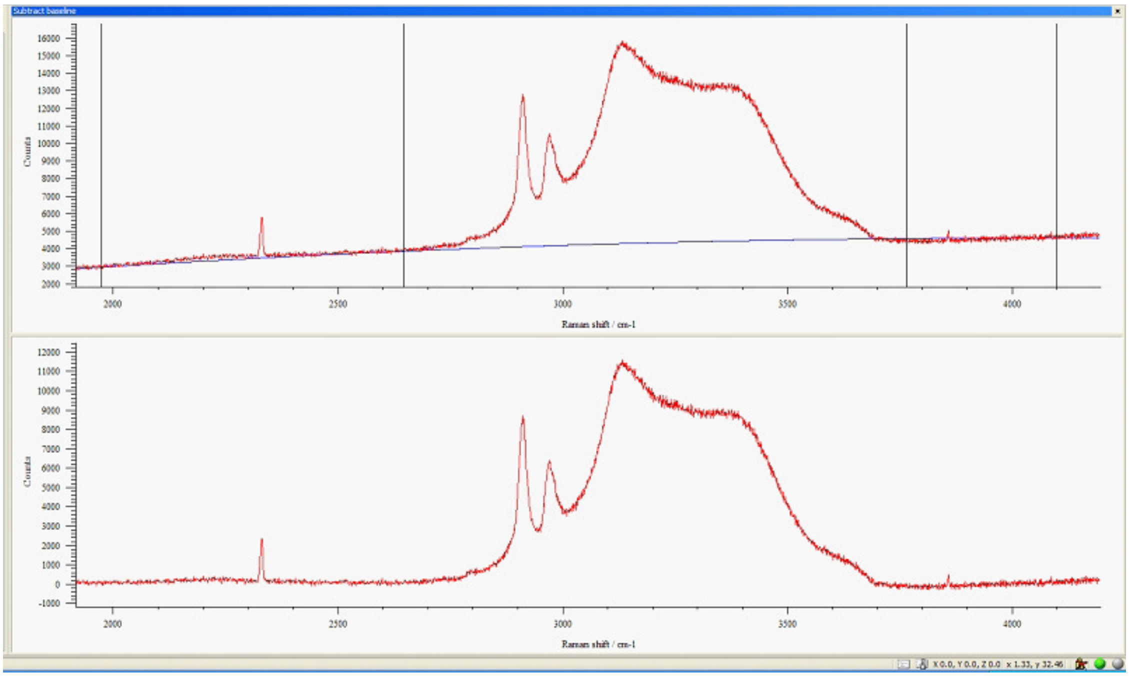

Figure 3.4: Snapshot of the fitting procedure by Renishaw Wire 3.1 software. Top: experimental Raman spectrum of the OHS region of water (red). Four positions for which no Raman signal is expected are marked manually and held constant for all samples (vertical black lines). The blue line indicates the baseline, as suggested by the software on the basis of the intensity at the four marked points. Bottom: preview of the baseline-corrected spectrum (MCM25 at 190 K).

position values for the corresponding OHS mode were used as starting parameters for the fitting procedure of this spectrum. Results of this fit were the starting parameters in the peak fitting procedure of the spectrum at the next nearest temperature point. This fit procedure was applied for all subsequent spectra measured for the bulk water droplet. After fitting the bulk water spectra within the entire temperature region, the spectra of water in the largest pores (SBA89) were fitted in the same manner. Hereby, staring parameters for the first measurement at room temperature were taken from the corresponding fit results obtained for bulk water. For water in smaller pores the first set of starting parameters was taken from the corresponding fit results of the next nearest pore size. The subsequent fit procedure for all samples was performed in the same way.

3.2 SANS, SAXS and WAXS experiments at large-scale facilities

All experiments presented in this section were performed at the Helmholtz Zentrum Berlin (HZB), utilizing the synchrotron radiation facility BESSY II and the neutron source BER II. Ordered mesoporous materials MCM-41 with four different pore diameters were used as confining matrices. The used materials are denoted as MCM20, MCM34, MCM39, and MCM44. The amount of water inside the mesopores was controlled by filling them from the gas phase using the DEGAS (Dedicated Environment for combined GAs sorption and Scattering) equipment, which was already successfully used in our previous work [Erko, 2008, Erko, 2010]. The basic working principle of such a vapour dosing system is described in subsection 3.3.1 in more detail. The filling fraction of the mesopores was chosen to be close to but not larger than unity, to avoid ice nucleation outside the pores. The pores were filled with H_2O at 280 K for SAXS and WAXS, and with D_2O for SANS measurements. Heavy water was chosen for the neutron experiments to circumvent the large incoherent scattering from hydrogen atoms. The studied temperature region was 100 - 280 K.

Small-angle neutron scattering (SANS) data were collected at the instrument V1 at the BER II reactor. The incident monochromator-selected neutron beam had a wavelength of 0.523 nm. A Be-filter at liquid nitrogen temperature was used to suppress neutrons with wavelengths below 0.39 nm. The scattering patterns were collected using a ^{3}He detector with the sensitive area of 19 x 19 cm^2 and the spatial resolution of 1.5 x 1.5 mm^2. The sample-detector distance was 1.025 m, giving the measured scattering vector region of q = 0.6 - 2.8 nm^{-1}. Calibration of the sample-detector distance was performed using a yttrium-iron garnet (YIG) standard sample. SANS data were accumulated for 30 minutes at a fixed temperature. Data correction was performed using the Compaq Alpha Workstation software provided by the beamline. This software essentially performs data correction of the obtained neutron intensity by the formula:

$$I(q) = \frac{I_{s+sh} - I_{Cd}}{\tau_{s+sh}} - \frac{I_{sh} - I_{Cd}}{\tau_{sh}}, \tag{3.1}$$

here I and τ with the indices sh and $s + sh$ indicate the measured intensity and transmission of the empty sample holder, and those of the sample within the sample holder, respectively. The index Cd indicates the background intensity, measured by placing a strong neutron absorber, i.e. Cadmium, at the sample position. All spectra were normalised with respect to the primary beam intensity. Cooling and heating of the sample was performed in 10 K steps between the measurements using a CGA-PTR mini Pulsetube Refrigerator. The cooling rate was 2 K/min. SANS measurements were performed only for two samples i.e. MCM20 and MCM34 due to the limited measurement time available at the instrument.

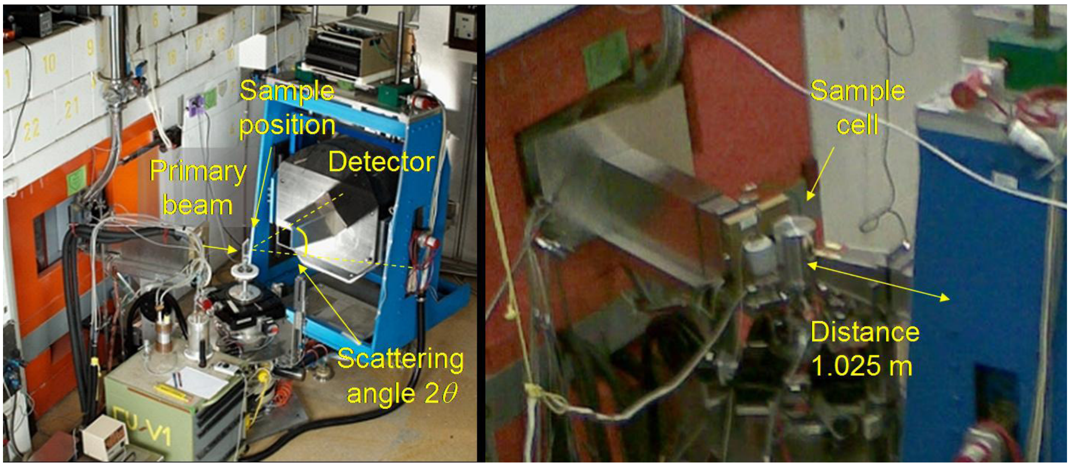

Figure 3.5: SANS experimental setup at BER II V1 beamline. The sample was embedded within an aluminium sample cell.

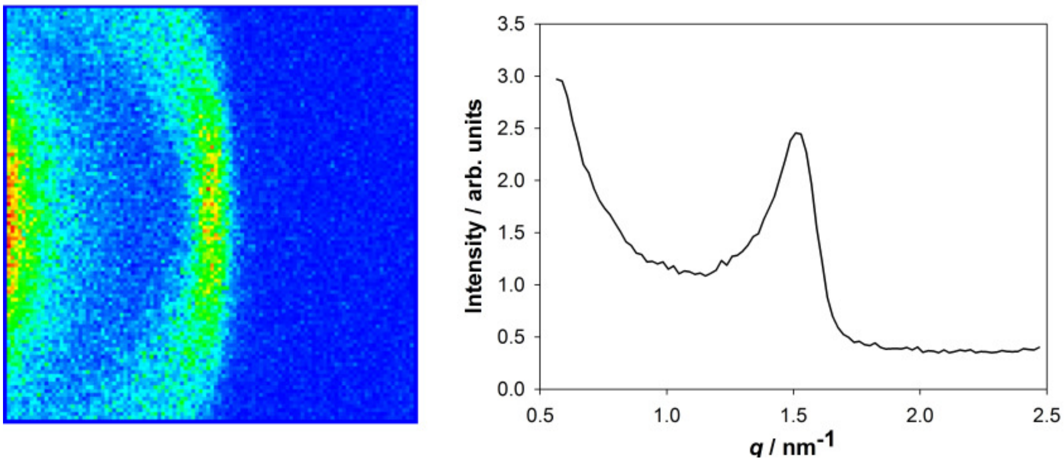

Figure 3.6: Left: neutron scattering pattern of MCM34 material on the 2D detector behind the sample. Right: the corresponding scattering intensity after radial averaging using Equation 3.2.

Figure 3.6 shows a scattering pattern as observed during the experiment. The Bragg peak in Figure 3.6 arises from the hexagonally ordered pore structure of MCM34. Due to the slit-like shape of the primary neutron beam, the powder ring on the detector is smeared in the radial direction. Therefore, the spectra obtained after radial averaging (see next paragraph and Equation 3.2) are smeared to lower q values. Data analysis of this experiment included only the extraction of the maximum value of the Bragg peak intensity at a particular temperature. The relative change of the Bragg peak intensity with temperature was further used to determine the change of the average water density in nanopores.

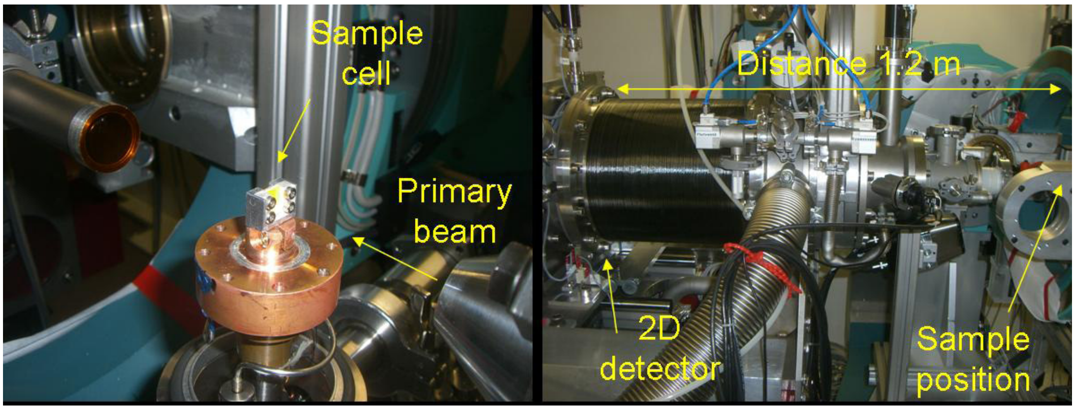

Figure 3.7: SAXS experimental setup at BESSY II 7T-MPW-SAXS beamline. The sample is embedded between two Kapton foils. During the experiments the sample cell is covered by a Beryllium dome and by a vacuum shield (see also Figure 3.9).

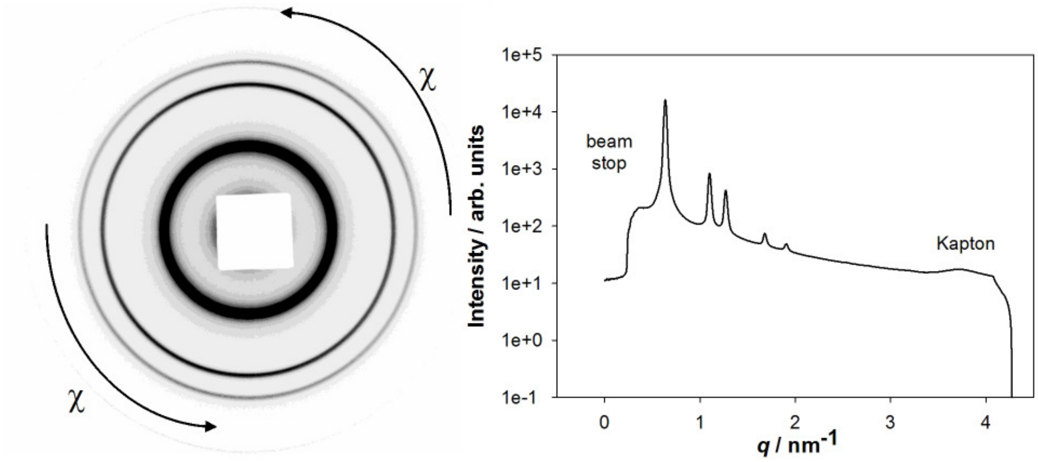

Figure 3.8: Left: two-dimensional X-ray scattering pattern of empty SBA89 material on the Mar165 detector behind the sample. Right: the corresponding scattering intensity radially averaged using Equation 3.2. The Kapton peak arises from the sample cell.

Small-angle X-ray scattering (SAXS) measurements were performed at the BESSY II 7T-MPW-SAXS beamline in the scattering vector region of q = 0.65 - 3.50 nm^{-1} at a sample-detector distance of 1.2 m. The chosen wavelength was 0.098 nm, and the data were collected for 10 s for each pattern using a 2D position sensitive detector (charge-coupled device Mar165, MarResearch, USA). The temperature of the sample was changed continuously with a rate of 1.4 K/min. The setup of the SAXS experiment is shown in Figure 3.7. Data were normalised with respect to the primary beam intensity. The sample transmission was measured by a photo diode placed on top of the beam stop of the detector. The transmission was properly taken into account within the data normalisation. Since the scattering patterns were collected on a two-dimensional detector behind the sample (see Figure 3.7 and Figure 2.26), a typical powder diffraction pattern consists of concentric rings, where the distance from the centre gives the corresponding scattering angle. The *radial averaging* of two-dimensional scattering data implies an angular integration of concentric spheres around the primary beam:

$$I_s(q) = \frac{1}{2\pi} \int_0^{2\pi} I_s(q, \chi) d\chi, \tag{3.2}$$

the corresponding integration angle is visualised in Figure 3.8.

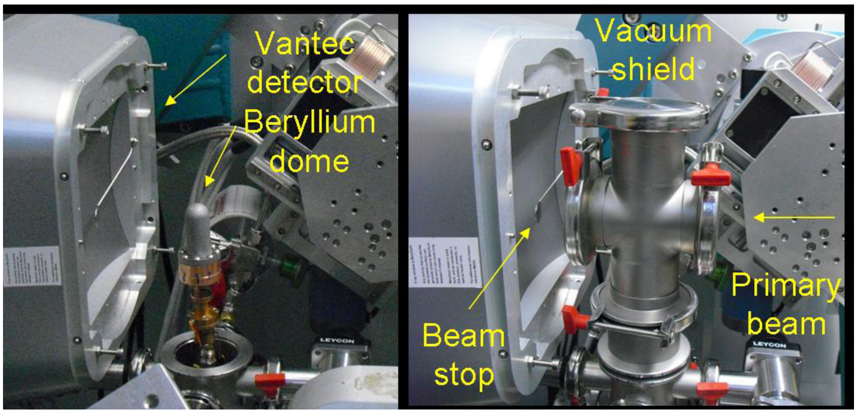

Figure 3.9: WAXS experimental setup at BESSY II KMC2 beamline showing the sample cell covered by a beryllium dome (left). The vacuum shield (right) prevents formation of frost on the sample cell upon cooling. In order to monitor WAXS peaks from ice the sample-detector distance was only 0.071 m.

Wide-angle X-ray scattering (WAXS) experiments were conducted at the BESSY II KMC2 experimental station [Erko, 2000]. The scattering patterns were collected with a position sensitive area detector (Bruker Vantec 200) for 20 s each pattern using the same cooling and heating protocols as for SAXS. The sample detector distance was 0.071 m, and the wavelength was 0.154 nm, which gives an accessible q-range of $q = 10 - 30$ nm^{-1}. All data were normalised to the primary beam intensity and radially averaged (see Figure 3.10). No transmission correction was performed for WAXS measurement. In order to obtain the WAXS signal only from water the data were corrected by the appropriate subtraction of a separate measurement of the empty sample within the sample holder, performed at room temperature. Unfortunately, the instrument was not precisely calibrated to absolute q-values. Therefore, the fitted values for the peak position obtained for bulk ice was used for data normalisation to the known q-position of hexagonal ice. The analysis of the water WAXS signal was performed only qualitatively by monitoring the relative change of peak characteristics (intensity, full-width of half maximum FWHM, and position) with temperature.

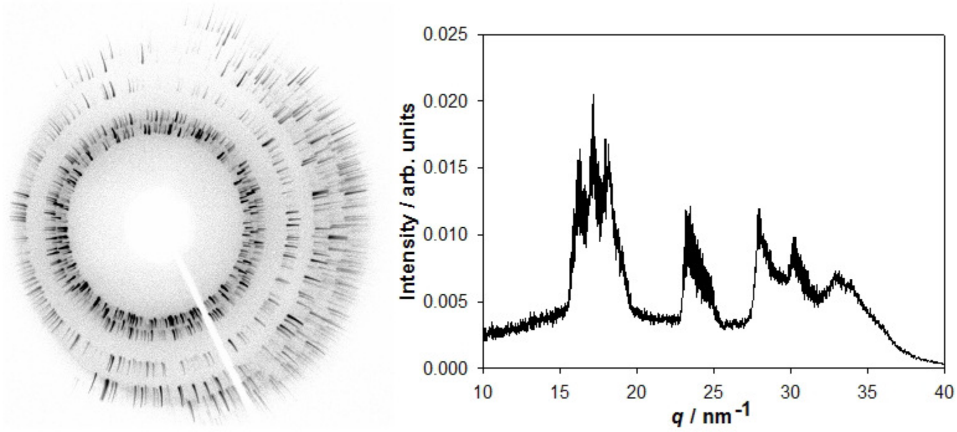

Figure 3.10: Left: X-ray scattering pattern of bulk ice (strongly overfilled mesopores) on a 2D detector. The occurrence of radial “spikes” is described in the text. Right: the corresponding scattering intensity radially averaged and corrected by subtracting the scattering of empty sample within the sample holder.

In contrast to the previously shown SAXS signal, the scattering pattern in Figure 3.10 consists of a number of concentric spots, rather than of rings. The number of ice crystals hit by the X-ray beam was not enough to produce a scattering pattern of a perfect powder. The radial smearing of these spots originates from a different effect. The combination of a relatively small sample-detector distance with a finite penetration depth within the detector’s active area led to the occurrence of these “spikes” in radial direction on the detector picture. An illustration of this effect is shown in Figure 3.11. At large detector distances, the scattering photons hit the detector by an angle of approximately 90°. Hereby, a single photon is ideally recorded by a single detector pixel. However, if the angle between a scattering photon and the detector active area gets too low, one single scattering photon can be recorded by several detector pixels. This effect also depends on the depth of detector pixels. It is most pronounced for sharp intensive Bragg peaks, such as for bulk hexagonal ice (see Figure 3.10). For measurements of water in mesopores this effect was not extensively pronounced probably due to strong peak broadening resulting from the small size of the ice crystals in mesopores.

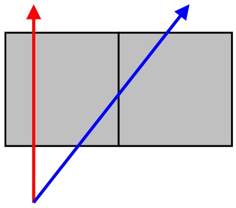

Figure 3.11: The red photon is detected by only one detector pixel (grey squares), the blue one - by two.

3.3 SAXS experiments at the laboratory X-ray source

Quantitative studies of water sorption in mesoporous silica are experimentally challenging and quite time consuming due to very slow equilibration. Neutron or synchrotron radiation facilities as used in the experiments in the previous section do typically not provide sufficient beamtime to conduct such experiments in a systematic way with sufficient equilibration time between the single measurements. Therefore, an *in situ* sorption device was developed to study sorption processes in ordered mesoporous materials using a laboratory small-angle X-ray instrument. This chapter presents the "COSCAD's" (COmbined SCattering and ADsorption system) setup in detail, and shows its first application by studying repeated sorption of water in SBA-15 with *in situ* SAXS.

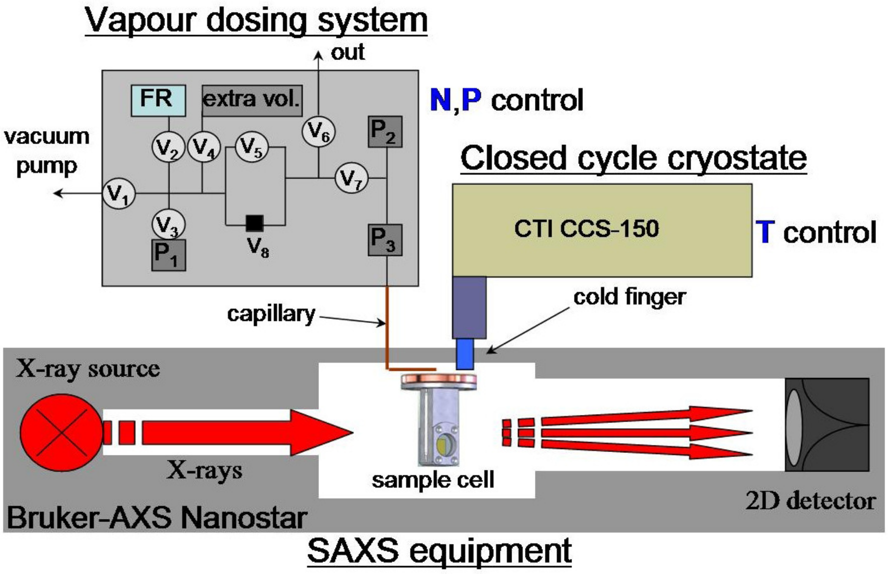

Figure 3.12: Schematic view of the laboratory sorption SAXS apparatus COSCAD's. Pneumatic valves of the vapour dosing system are denoted by V_1-V_7, the proportional valve by V_8, the pressure gauges by P_1-P_3, and the fluid reservoir by FR. Figure taken from [Erko, 2012b].

3.3.1 COmbined SCattering and ADsorption system (COSCAD's)

The apparatus for *in situ* small-angle X-ray scattering (SAXS) studies of fluid sorption is a combination of three independently working systems, i.e. the laboratory SAXS system, a closed cycle cryostat for sample temperature control, and the vapour dosing system including the sample cell (Figure 3.12). This apparatus allows studies of monolithic or powdered porous samples via the gas sorption method in different temperature regions currently ranging from 200 K to 330 K. The sorption process can be either monitored quantitatively by stepwise volumetric analysis, or by continuous gas dosing without quantitative determination of the adsorbed amount. At the same time, SAXS patterns can be measured for different gas pressures. All components of the system including the sample cell are constructed in a modular way and can also be used outside the laboratory location (e.g. at a synchrotron or neutron facility).

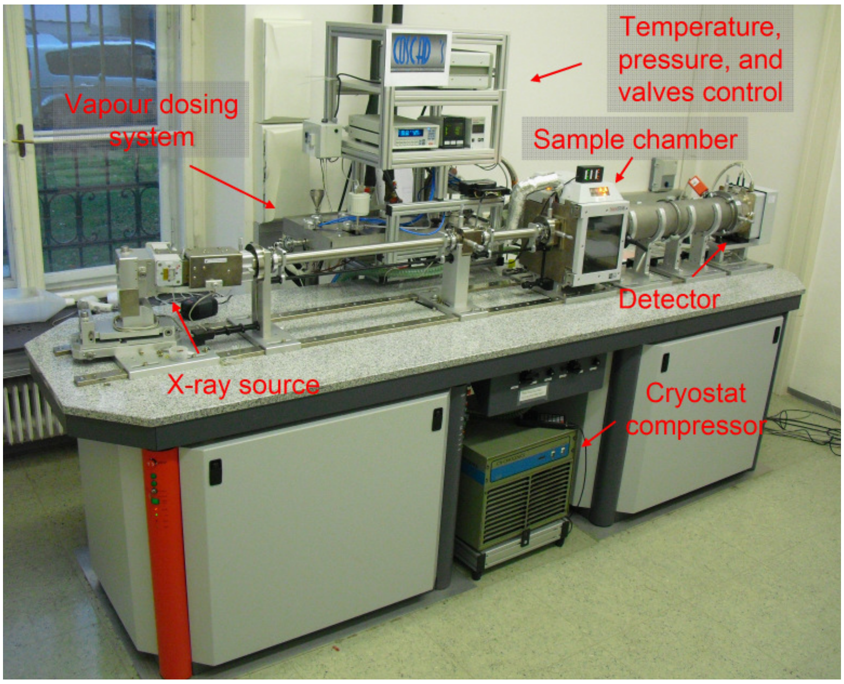

Figure 3.13: Bruker AXS Nanostar as a part of the COSCAD's setup.

The commercial Nanostar SAXS system (Bruker-AXS, Karlsruhe, Germany) includes a sealed-tube Cu source operated at the $K-\alpha$ radiation line, selected and focused by two crossed-coupled, parabolically bent multilayers (Göbel mirrors). The SAXS patterns are collected by a Bruker-AXS Hi-Star area detector. Two different sample-detector distances (0.25 m and 1.05 m) can be used to cover a scattering vector range from 0.1 nm^{-1} to 8.0 nm^{-1} with sufficient overlap.

The custom-built vapour dosing system is used for the controlled filling and emptying of the porous material with different fluids. The components of the system consist of steel tubes tightly connected via Hy-Lok fittings (Hy-Lok, Oyten, Germany). Optimum gas flow control is realised by pneumatic bellow valves operated by a custom-written Labview software. Two high-pressure gauges (Oerlikon Leybold Vacuum, Cologne, Germany) and one low-pressure gauge (Pfeiffer Vacuum, Asslar, Germany) operating between 10^{-1} mbar - 1000 mbar and 10^{-5} mbar - 10 mbar, respectively are used for pressure control. The two different types of pressure

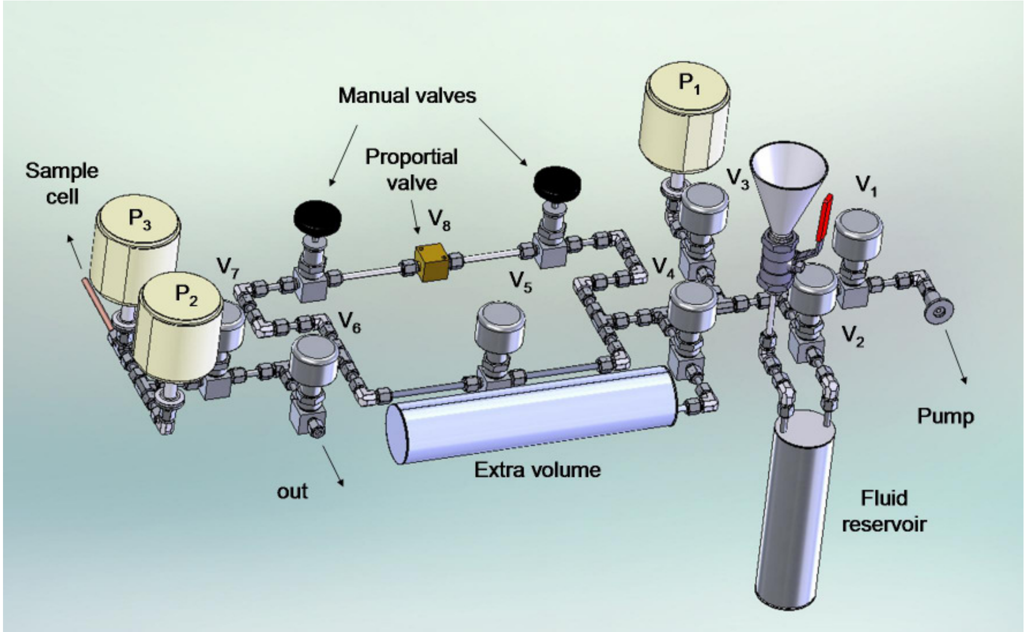

Figure 3.14: COSCAD's vapour dosing system. Notation of the valves and the pressure gauges corresponds to that in Figure 3.12.

gauges with sufficiently overlapping ranges are necessary for customisable studies of various fluids and gases. The vapour dosing system is connected to the temperature controlled sample cell via a copper capillary. The whole sorption system can be kept at a considerably higher temperature than the sample (up to 350 K), in order to avoid fluid adsorption on the inner surfaces of the connection tubes.

The vapour dosing system can be operated either stepwise or in continuous mode. Stepwise valve operation allows an accurate step-by-step determination of the volumetric sorption isotherm (i.e., a step-by-step gas dosing, each followed by pressure equilibration) between two sorption steps. Figure 3.15 exemplary shows the pressure data measured within the dosing volume during a single adsorption step. The experimental description for Figure 3.15 is given below:

- after evacuation of the entire sorption system (except the fluid reservoir) the initial state requires closing of all valves
- valve V_4 has to be opened in order to extend the dosing volume by the “extra volume” reservoir
- the pressure within the dosing volume can be measured by opening the valve V_3 to the pressure gauge P_1
- at $t \approx 75$ s the valve V_2 between the fluid reservoir and the entire system is shortly opened until the fluid vapour fills the entire dosing volume, hereby the pressure within the dosing volume increases from $p \approx 0$ to $p = p_1 \sim 5$ mbar
- system equilibration persists until $t \approx 200$ s

- at $t = 200$ s the valves V_5 and V_7 are simultaneously opened, connecting the dosing volume to the sample cell
- fluid adsorption in mesopores leads to a decrease of the pressure within the dosing volume, the total equilibration time of the system depends on both, the fluid and the sorbate
- the pressure value which corresponds to the equilibrium pressure can be obtained by extrapolating the pressure decay by an exponential function to the value of p_2
- the amount of adsorbed fluid can calculated from the measured pressure drop during a sorption step ($\Delta p = p_1 - p_2$) using the calibrated volume values (Table 3.1) of the system, and applying the ideal gas equation of state

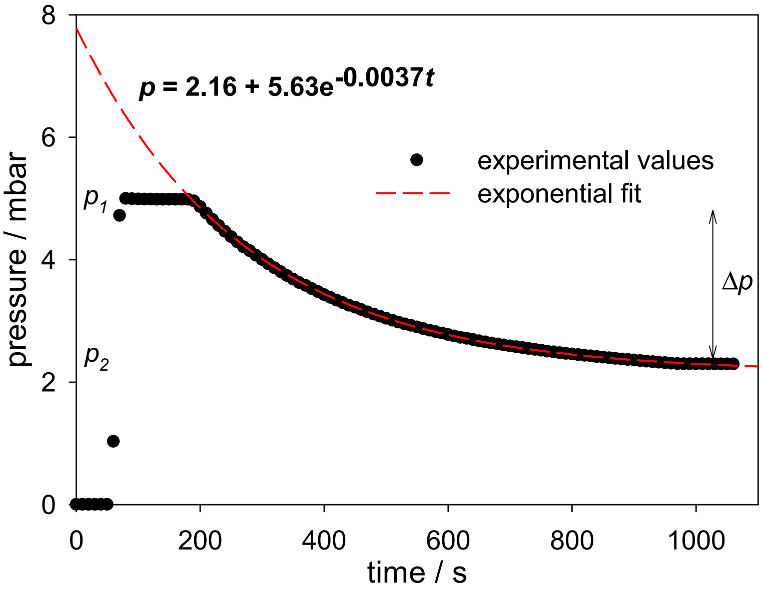

Figure 3.15: Pressure behaviour within the dosing volume, measured at the pressure gauge P_1 during an adsorption step. The amount Δn of adsorbed material can be calculated by $\Delta n = \Delta p \cdot (V/R_G T)$.

The volume calibration of the different parts of the system was performed with helium gas at pressures below 100 mbar. The initial value for the volume of the fluid reservoir was calculated using the technical drawings of the system. Volume calibration of the residual parts of the vapour dosing system was performed by monitoring the pressure decrease of helium gas upon relaxation from the fluid reservoir. Assuming that helium at low pressures can be treated as an ideal gas, the volume calculation was performed inserting the values of the pressure changes into the equation of state of an ideal gas. Volume values for all parts of the system were obtained from three independent measurements. The average values from these measurements were taken to determine the particular volume value. As a cross-check, a reverse calculation of the volume of the fluid reservoir was performed using the volumes of the entire system. The average value of these two measurements was taken as the real volume of the fluid reservoir. The difference between this value and that from technical drawings was taken as the relative volume error for all parts of the dosing system. The error is smaller than one per cent. The volume values for all parts of the system are summarised in Table 3.1.

Section	Volume / ml	error / ml
Fluid reservoir	483	4
Between V_1, V_2, V_4, V_5, V_8	34.4	0.3
Between V_5, V_6, V_7, V_8	15.5	0.2
Extra volume	682	6
Sample cell + capillary	60.3	0.6

Table 3.1: Calibrated volumes from different parts of the vapour dosing system.

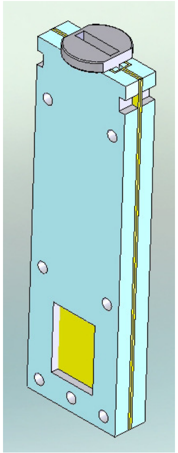

Figure 3.16: Sample cartridge, including two Kapton foils between aluminium plates and a spacer.

Alternatively, the vapour dosing system can be operated in a continuous filling/emptying mode by the appropriate adjustment of the proportional valve V_8 located between the reservoir and the sample cell (see Figure 3.14). The appropriate choice of gas flux rate for the complete sorption isotherm, or separately for individual parts of it, is crucial in this continuous mode. Incorrect values of the measured pressure in the sample cell may result if the gas pressure increase is too fast in the continuous sorption process. However, if equilibration times are known for a certain sample and a certain fluid (for instance from earlier measurements using the volumetric method), this continuous mode allows saving time during *in situ* measurements, since the SAXS data collection can also be performed continuously. This is particularly necessary for measurements at synchrotron radiation sources, where available beamtime is restricted. In order to optimise the filling and emptying processes, the system software allows pre-setting of a number of different flux ramps for each sorption direction. However, one should keep in mind that in the course of a continuous sorption process the sample is never in real equilibrium with the sorption fluid, which can therefore lead to mis-interpretation of data.

A special sample cell was constructed to be placed in the vacuum chamber of the SAXS system, combined with the vapour dosing system and the temperature control from the closed cycle cryostat. The sample cell has two indium-sealed beryllium windows which separate the sample atmosphere from the evacuated SAXS chamber (see Figure 3.17). The sample cell body is made of aluminium and copper, and is fixed to the x-y stage. The cell is designed for monolithic samples of a maximum size of (6x10x1) mm^3 or powder samples of similar volume. In order to simplify the sample change procedure samples are embedded within replaceable sample cartridges. Therein, the sample is embedded between two Kapton foils which are fixed by two aluminium plates with openings for the X-ray beam. A cone-shaped hollow aluminium spacer between the two Kapton foils realises optimal connection to the gas supply from the vapour dosing system (see Figure 3.16).

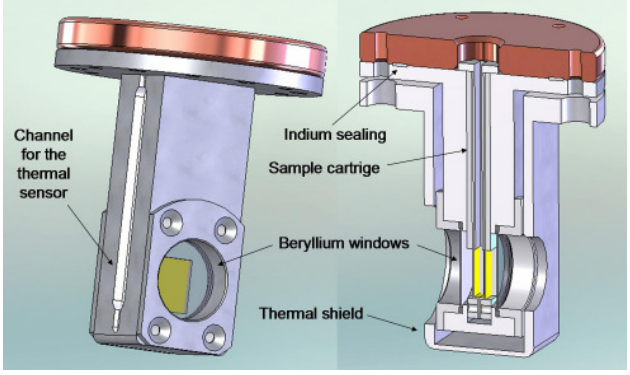

Figure 3.17: X-ray sample cell in normal view and in cross-section. The thermal shield reduces the power of radiation on the sample cell.

Temperature control of the sample cell is realised by a closed cycle cryostat (CTI CCS-150, Janis Research, USA). The thermal connection is realised by flexible braided copper wires. The system is operated via a Lake Shore Model 335 (Lake Shore Cryotronics, USA) temperature controller by the same Labview software as used for the vapour dosing system. The silicon diode temperature sensor is embedded in a channel within the sample cell body. In a sorption process the sample cell is typically held slightly below the temperature of the fluid reservoir. This setup presently allows measurements in a temperature range from 200 K to 330 K. The upper limit is due to the indium-sealed parts of the sample cell. The lower limit is due to the old cryostat. With a new cryostat measurements at temperatures down to at least 70 K will be possible, allowing sorption studies using liquid nitrogen.

3.3.2 Samples and measurements

Process	Time / hours
Adsorption 1	62
Desorption 1	48
Adsorption 2	76
Desorption 2	50
Adsorption 3	70
Desorption 3	68
Adsorption 4	25
Desorption 4	24
Aged sample ads.	66
Aged sample des.	48

Tabelle 3.2: Overall adsorption and desorption times for the individual cycles.

The mesoporous SBA89 powder used in this study was taken from the same batch as in the other experiments (section 3.1). Water adsorption and desorption cycles were measured at 278 K after initial sample annealing at 330 K for 24 hours under low vacuum conditions (10^{-3} mbar). Pore filling and emptying of SBA89 with water was performed by the continuous vapour dosing mode. In order to avoid bulk water condensation in the sample cell the maximal pressure value was limited to 8.6 mbar which is slightly below the bulk water saturation pressure at the given temperature. The overall times of the individual adsorption-desorption cycles are summarised in Table 3.2. The required time for a sorption path close to equilibrium was estimated from our experience in earlier work of water sorption in the same SBA89 material [Erko, 2010]. This ensures that the sample is close to equilibrium even in the capillary condensation regime where kinetics becomes particularly slow. Only for cycle 4 insufficient equilibration may possibly be expected.

Four complete adsorption-desorption cycles of water in SBA89 were performed in direct sequence and SAXS patterns were measured *in situ* with the Nanostar configuration of 1.05 m sample-detector distance. This detector distance was carefully calibrated using a Ag-behenate standard sample. Each SAXS spectrum was accumulated for 10 minutes. All scattering data were normalised to the primary beam intensity measured by the scattering intensity of glassy carbon before and after the measurements. The pressure values for the individual SAXS data points were taken at the mid-time of the SAXS accumulation period. After completion of each desorption run the sample was evacuated for three hours at the experimental temperature before starting a next sorption cycle. After the fourth sorption cycle the sample was evacuated at an elevated temperature (330 K) for 3 hours, while simultaneously recording the SAXS pattern. Several further water sorption cycles were then performed on this sample and it was stored for several months under ambient laboratory conditions with varying relative humidity. To probe the state of the sample after this treatment, a further water adsorption measurement was performed without previous annealing (“aged sample”). 2D data were radially averaged according to Equation 3.2 to obtain SAXS profiles. Figure 3.18 exemplary shows experimental data for the two-dimensional hexagonal pore lattice of SBA89 material in its empty state.

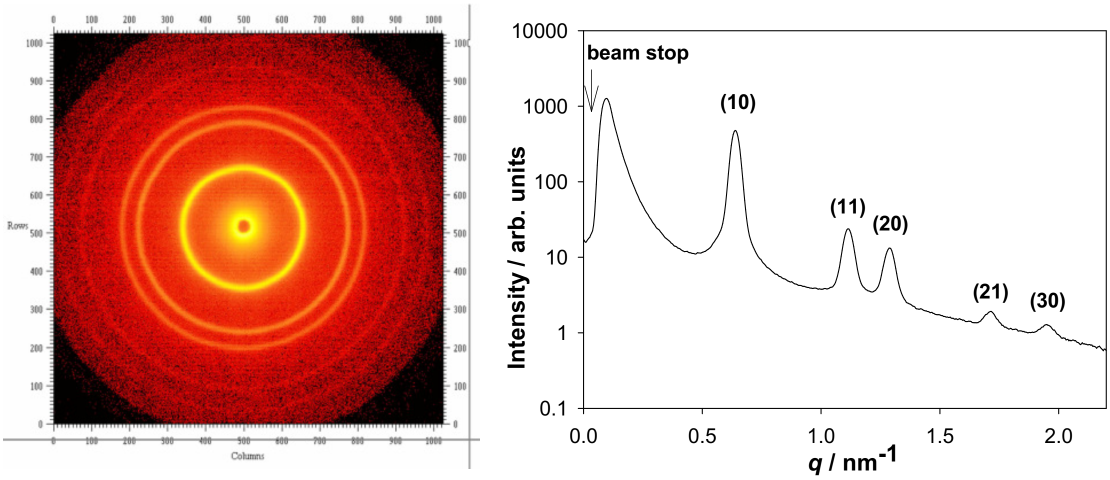

Figure 3.18: Left: X-ray scattering pattern from empty SBA89 on a two-dimensional detector (Bruker AXS Nanostar). Right: the corresponding radially averaged scattering intensity of SBA89 with the lattice constant of $d = 11.52$ nm. Numbers denote the Bragg peak order of the two-dimensional hexagonal pore structure according to Equation 2.39.

4 Results and Discussion

This chapter presents the results from all four experimental approaches performed within this thesis. Starting with the inelastic scattering of light (Raman scattering) in section 4.1, the next section presents the results from combined elastic scattering of X-rays and neutrons at two different ranges of scattering angles (SAXS, SANS, and WAXS) (section 4.2). SAXS data from this study are further analysed in terms of the influence of temperature on the pore lattice parameter of the mesopores with different diameters. Pore lattice deformation with temperature is analysed and discussed in section 4.3. Results from repeated water sorption in SBA-15 measured by means of SAXS at the laboratory equipment (COSCAD's) are presented and discussed in section 4.4.

The results presented in section 4.1, in section 4.2 and in section 4.4 are already published in scientific journals, referred as [Erko, 2011], [Erko, 2012a], and [Erko, 2012b], respectively. A large part of the text passages in this chapter corresponds to those in the publications.

4.1 Structure of confined water

The two spectral regions analysed in this thesis are attributed to the HOH-bending mode of water molecules around 1600 cm^{-1}, and to that of the OH-stretching (OHS) ranging between 3000 - 3700 cm^{-1} (see subsection 2.4.5). Analysis of HOH-bending region was performed only qualitatively comparing the relative spectral intensity measured for different temperatures, and for different pore diameters. Experimental data analysis of the OHS region of water was performed by determining the position, width, and relative peak area of the HB mode V in the OHS part of the Raman spectrum as a function of temperature and pore diameter. The spectral position of the mode I OHS contribution was used to estimate the phase transition temperature for pore diameters larger than 2.5 nm. The results are compared with literature values for bulk (hexagonal) crystalline ice and for bulk amorphous ice and are discussed with respect to the influence of confinement on the low-temperature phase behaviour of water.

4.1.1 Raman spectra

The experimental Raman spectrum of the entire measured spectral region between 100 cm^{-1} and 4200 cm^{-1} is shown in Figure 4.1. The particular contributions are assigned in Figure 4.1, determined by a number of systematic measurements during the preparation of the experiment. Thereby, the Raman signal of water is divided into three separate vibrational contributions. The measured spectra are dominated by a broad and intensive signal in the range 3100–3700 cm^{-1}, which is attributed to the water OH-stretching (OHS) mode [Walrafen, 1967]. The weakly pronounced peak around 1600 cm^{-1} is the signal of HOH-bending [Franks, 1975]. The contribution below 250 cm^{-1} originates from the vibration of free water molecules [Zwick & Landa, 1994].

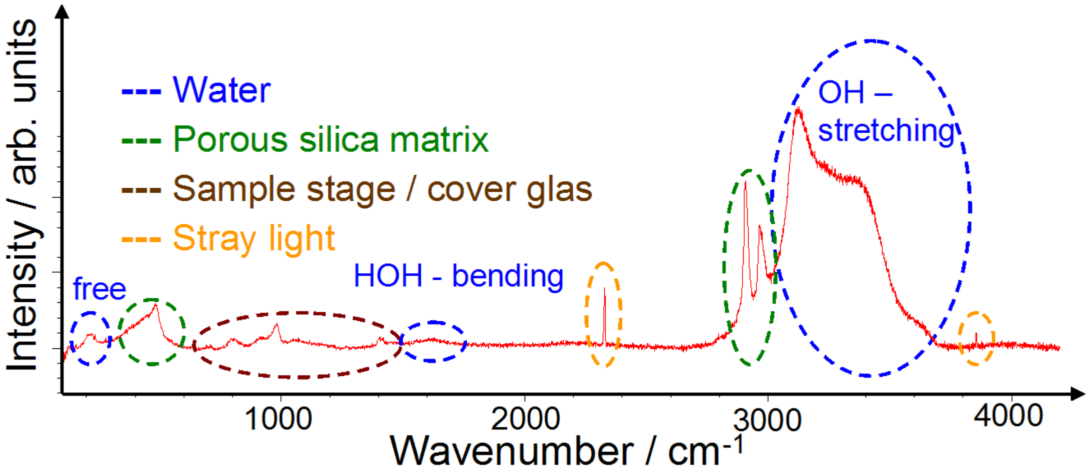

Figure 4.1: Experimental Raman spectrum for water in mesopores of MCM25, measured at 143 K.

Within the context of this work, particularly the OHS region of water molecules ranging between 3100 cm^{-1} and 3700 cm^{-1} was analysed in detail. Additionally, a qualitative analysis of the HOH-bending vibration around 1600 cm^{-1} was performed. The region around 250 cm^{-1} and below was not analysed.

Unfortunately, the analysis of HOH-bending is limited by the very low signal-to-noise ration of the Raman signal in this region. However, the signal of bulk water and for water confined in different systems distinctly changes also in the spectral region around 1600 cm^{-1}. Figure 4.2 shows experimental data of the water droplet measured at 283 K in the liquid state and at 163 K in the frozen state. The data suggest that the signal in this region vanishes below the water freezing point. Figure 4.2 additionally shows a measurement of water confined in the pores of SBA89 material. Various experimental methods verify that water confined in SBA89 pores is frozen at the temperature of 163 K (see e.g. [Schreiber, 2001]). However, intensity around 1600 cm^{-1} is still present for this case. This observation already shows a distinct difference between the Raman signal of frozen bulk ice and that of the frozen confined pore water. However, the low intensity in this region does not allow a quantitative signal analysis. Even marginal changes of the baseline correction strongly influence the data, resulting in arbitrary data interpretation.

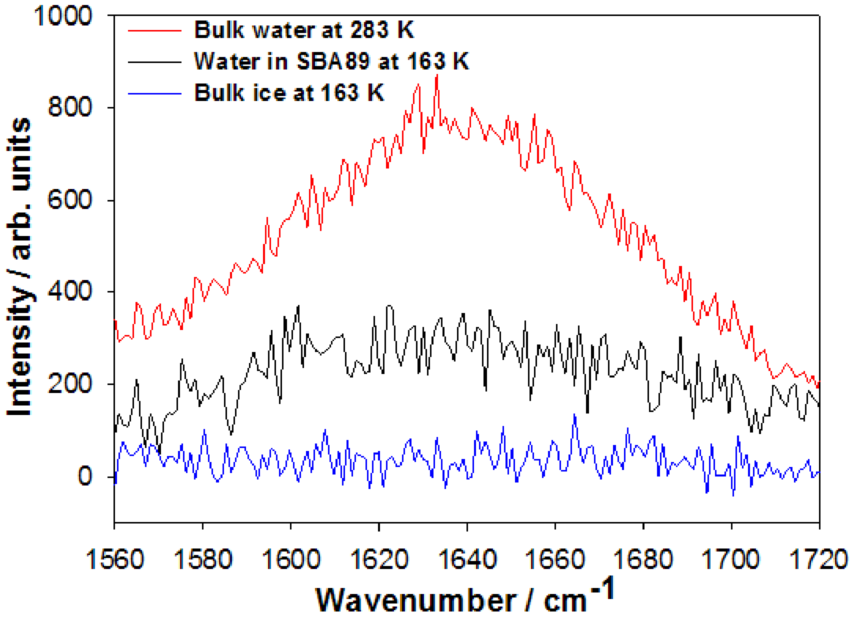

Figure 4.2: Experimental Raman spectra in the HOH bending region. Bulk water droplet in liquid phase measured at 283 K (red) and at in solid phase at 163 K (blue). The Raman signal from water confined in 8.9 nm wide pores of SBA89, measured at 163 K (black).

Room temperature spectra of the OHS region for bulk water (water droplet) and water confined in MCM25 (2.5 nm pore diameter) are shown in Figure 4.3. Also shown is the room temperature spectrum of dry MCM25 which was recorded in a stream of dry nitrogen gas. The OHS spectrum shows significant changes with temperature (Figure 4.4) and as a function of confinement in the pores (see Figure 4.5). In addition to the water OHS signal, two sharp peaks appear between 2900 and 3000 cm^{-1}. This double peak is also present for the empty MCM25 sample but is absent for the water droplet and should therefore be attributable to the mesoporous matrix. Similar spectral features were already reported and discussed in the literature, but their physical origin still seems to be a matter of debate. Because the spectral position is roughly consistent with CH-stretching, it has been attributed to hydrocarbon impurities remaining from the surfactant after calcination [Blin & Carteret, 2007]. However, because our samples were calcined at 550 °C, we do not expect any hydrocarbon impurities. A different description implies laser radiation–induced defects (silanone, i.e., $Si = O$ double bonds) [Zyubin, 2002], which seems to be a more plausible explanation. In our case, the two sharp peaks showed some minor variation for the different samples, but no temperature dependence was observed. This leads us to the conclusion that these peaks are not associated with the OHS spectrum of water. Hence, we do not discuss them further in the subsequent analysis. From Figure 4.4, we see that the tail of the water OHS spectrum slightly enters the region of these two peaks. Therefore, the two peaks were fitted together with the water spectrum (described later). A cross-check for some data sets revealed that the analysis is robust irrespective of whether the peaks are taken into account in peak fitting or not.

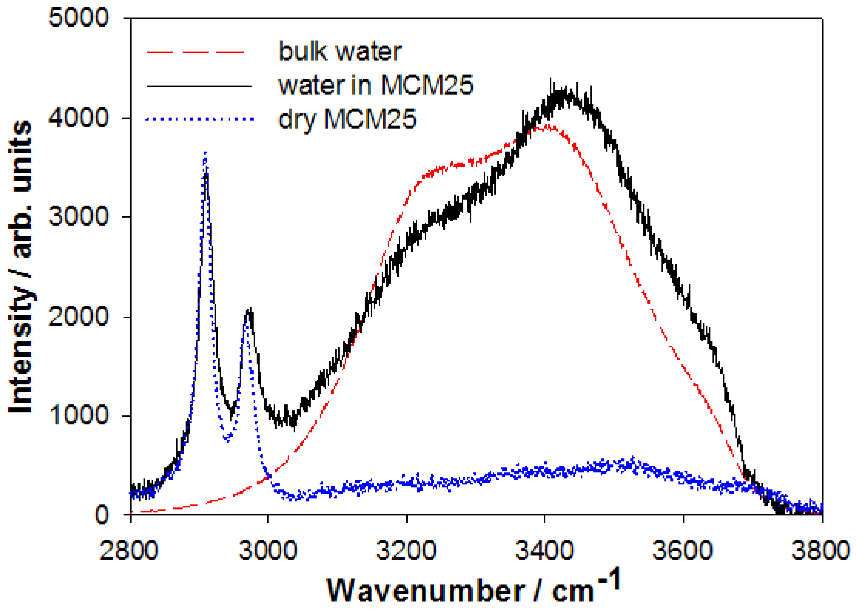

Figure 4.3: Experimental Raman OHS spectra measured at room temperature. The bulk water spectrum, represented by the measurement of the water droplet, is shown by the dashed red line. The black solid line is the spectrum measured for water confined in MCM25 (2.5 nm wide pores). The two sharp peaks at low wave numbers arise from the mesoporous matrix, as indicated by an independent measurement of dry MCM25 (blue dotted line). Figure adapted from [Erko, 2011].

Deconvolution of the broad OHS Raman spectrum was performed using four or five Gaussian functions, depending on the temperature. As an example, a fit of the spectrum of water confined in MCM25 at 143 K is shown in Figure 4.6. They are attributed to the OHS modes I–IV, with their spectral position ranging from 3200 cm^{-1} (mode I) to 3650 cm^{-1} (mode IV), in accordance with reports in the literature [Mallamace, 2007b, Sun & Zheng, 2009, Brubach, 2005, Walrafen, 1986]. At low temperatures, an additional component (mode V) appears somewhat below mode I (3100 cm^{-1}). This peak is attributed to the formation of a tetrahedral HB network, as in hexagonal, cubic, and (low density) amorphous ice, and is referred to as ice-peak [Venkatesh, 1975, Sivakumar, 1978b, Brubach, 2005, Bertie & Whalley, 1964, Rice & Sceats, 1981]. For all samples, the spectral characteristics (peak position, peak width, and intensity) of all OHS components change with temperature. Figure 4.4 demonstrates that lowering the temperature causes a spectral shift to lower wave numbers (redshift) and a sharpening of the mode V component is observed. Furthermore, the intensities of modes I and V were found to increase relative to those of modes II–IV as the temperature decreases.

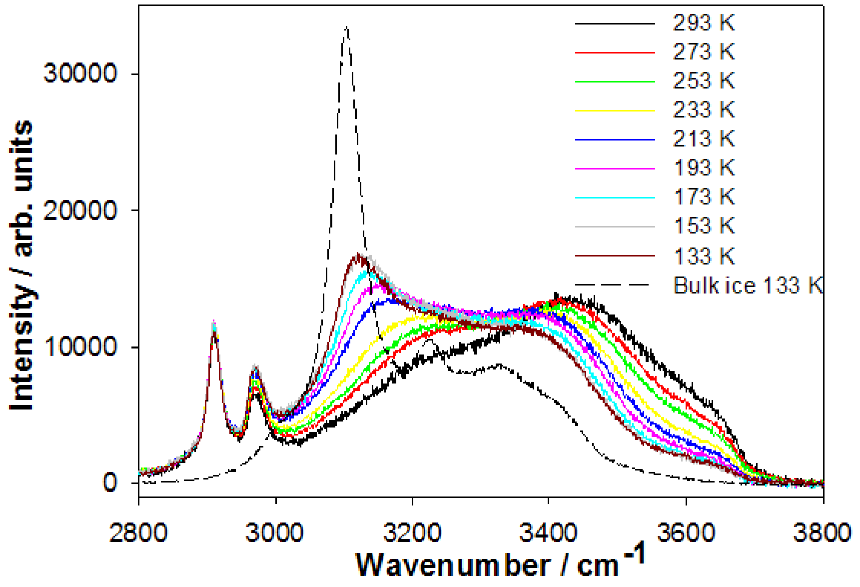

Figure 4.4: Experimental Raman OHS spectra measured for water in MCM25 (2.5 nm wide pores) for different temperatures (color solid lines), together with the experimental bulk ice spectrum at 133 K (black dashed line).

For water confined in the pores, the peak characteristics of the OHS spectrum are changing with the degree of confinement. In SBA89, the material with the widest pores (8.9-nm diameter) in the OHS spectrum largely resembles the features of the one for the water droplet (bulk water) at the same temperatures. As the pore size decreases, a blueshift of the mode V contribution and a broadening of the entire OHS water spectrum are observed, as demonstrated in Figure 4.5 for a given temperature of 143 K. The spectral characteristics (peak position, peak width, and intensity) of all components of the OHS spectrum of bulk water (water droplet) and water confined in pores of the six silica materials were determined from the spectral fits for the entire experimental temperature range. Major changes are observed for the low-wave-number contributions, or modes I and V. Modes II–IV did not exhibit such significant systematic changes with temperature or pore size. Therefore, a detailed analysis was performed only for OHS modes I and V.

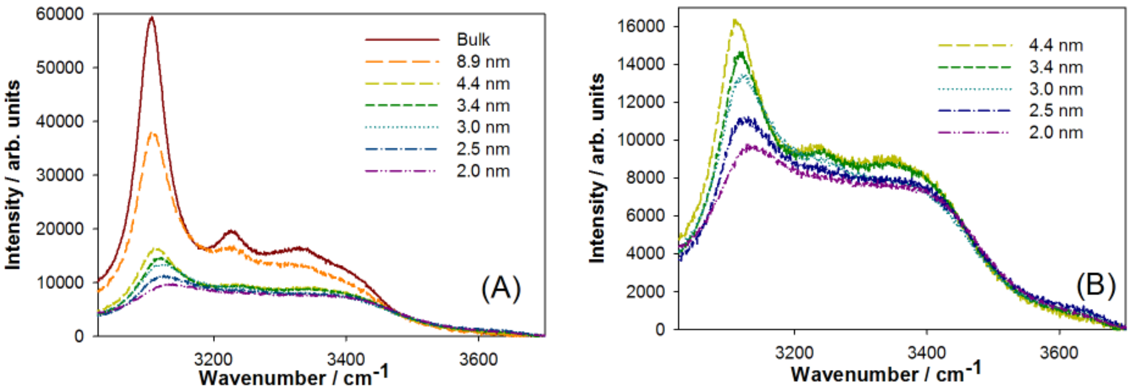

Figure 4.5: (A) Raman OHS spectra of water in different confinement at 143 K. The spectral contribution of mode V that occurs around 3100 cm^{-1} decreases monotonically with decreasing pore size. (B) shows magnified spectra of samples with pore sizes between 2.0 and 4.4 nm. Figure adapted from [Erko, 2011].

4.1.2 Freezing and melting in confinement

The OHS spectrum of bulk water (water droplet) exhibits significant changes upon freezing and melting. The position, as well as the peak width, of mode I changes in a discontinuous way at the phase transition temperature during the cooling and melting cycles. For confined water, a similar stepwise change of the mode I component is found as long as the pore diameter is not too small. Figure 4.7 shows exemplary the results for MCM34. The discontinuous step in the peak position is clearly observed occurring around 220 K upon cooling and occurring around 230 K upon heating. As the pore size decreases, the step occurs at a lower temperature and the step height decreases. For water confined in the sample of the 2.5 nm pore diameter, this step is at the limit of experimental detectability, and for the sample of the 2.0 nm pore size, all fitted parameters of the OHS mode I change smoothly with temperature.

The OHS spectrum of bulk ice is dominated by the intensity of mode V [Venkatesh, 1975, Bertie & Whalley, 1964] (see Figure 4.4 and Figure 4.5), which is absent in the liquid range at high temperatures. For the bulk water droplet, it appears between 263 – 253 K upon cooling, and it vanishes between 263 – 273 K upon heating, in perfect agreement with the step in mode I. The temperature at which the mode V peak first appears in confinement decreases with decreasing pore size. Therefore, not only the discontinuous change in the position and width of mode I but also the appearance of mode V seem to be indicative for the liquid–solid phase transition of water. However, at low-enough temperatures, the mode V peak is present in all samples - including the one with smallest pores (2.0 nm), for which no step was found by the analysis of mode I. Experimental evidence for mode V in supercooled liquid bulk water was also reported

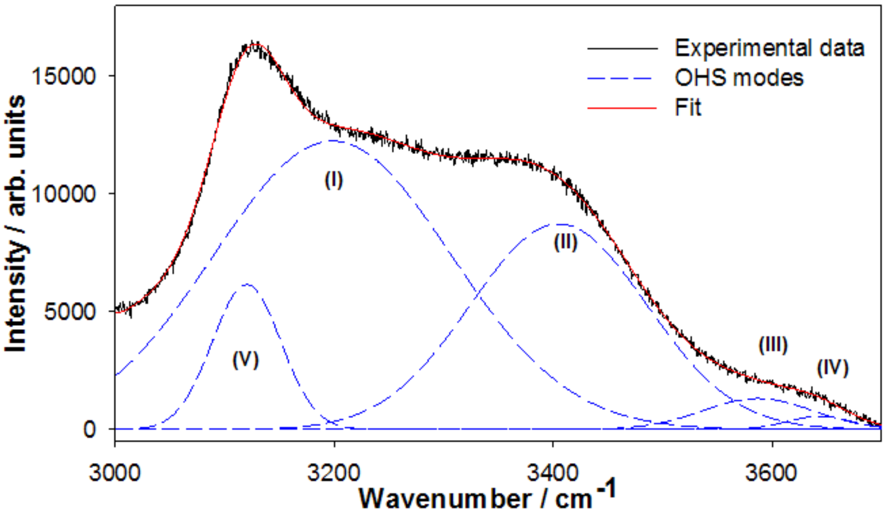

Figure 4.6: Deconvolution of the OHS region for water confined in MCM25 at 143 K: experimental data (black solid line), fit function (red solid line), and the five components (modes I–V) (black dashed lines). Figure adapted from [Erko, 2011].

in [D'Arrigo, 1981]. Therefore, we conclude that the first appearance of mode V should not be taken as unique indication of the liquid–solid phase transition of confined water. Instead, we take the discontinuous change in the position of mode I to estimate the phase transition temperature. According to current models [Sun & Zheng, 2009, Brubach, 2005, Bertie & Whalley, 1964], mode I represents the symmetric stretching vibration of strongly HB water molecules (see also Figure 2.32) that are already present in the liquid state. The Raman intensity of this mode is strong in both the liquid and the solid states; therefore, data analysis of the whole measured temperature range between room temperature and 123 K could be performed with high accuracy.

The confinement-induced shift of the melting temperature, $\Delta T_m = T_0 - T_m$, for water in a series of MCM-41 and SBA-15 materials was recently studied by Findenegg *et al.* using DSC [Findenegg, 2008]. They found that ΔT_m can be related to the pore radius R by a modified form of the thermodynamic Gibbs-Thomson equation (see subsection 2.2.3):

$$\Delta T_m = \frac{C}{R - t}, \tag{4.1}$$

with

$$C = C_{GT} = \frac{2T_0 \sigma_{sl} V^M}{\Delta H^M}, \tag{4.2}$$

where the parameter t was introduced to account for a layer of non-freezable water at the pore walls. A good representation of the DSC data was obtained with t = 0.6 nm, which corresponds to about two monolayers of non-freezing water molecules adjacent to the pore walls [Findenegg, 2008, Jahnert, 2008b]. From our Raman scattering results, we define the phase transition temperature in the pores by the discontinuous change of the spectral position of the OHS mode I (Figure 4.7).

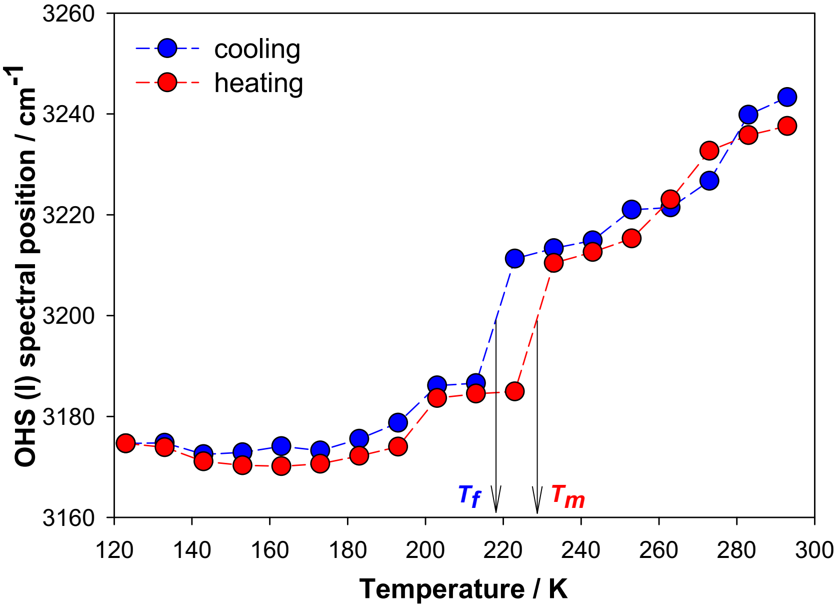

Figure 4.7: Fitted spectral position for OHS mode I of water confined in 3.4 nm pores. Open and filled circles indicate the cooling and heating directions, respectively. The freezing and melting temperatures, T_f and T_m, respectively, are assigned to the midpoints of the interval before and after the discontinuous change. Figure adapted from [Erko, 2011].

The nominal freezing and melting temperatures of water in a given sample were defined operationally as the midpoint of the interval before and after the discontinuous change of the OHS mode I spectral position. Since the spectra were taken in 10 - K steps, the transition temperatures have error bars of ± 5 K. To check whether the phase transition temperature T_m derived from the temperature dependence of the Raman OHS mode I conform to this simple relation, combiningEquation 4.1 with Equation 4.2 gives

$$T_m(R–t) = T_0(R–t)–C_{GT} \tag{4.3}$$

A plot of the resulting melting temperatures according to Equation 4.3, with t = 0.6 nm, is shown in Figure 4.8, together with the respective results from the DSC measurements taken from [Jahnert, 2008b, Schreiber, 2001]. The graph shows that the results from Raman scattering are in excellent agreement with those of the DSC study. The value of the Gibbs-Thomson constant derived from the analysis of the OHS mode I on the basis of Equation 4.3, $C = 63 \pm 8$ K nm, agrees within the limits of error with the respective value from the DSC study, $C = 53 \pm 1$ K nm. As in the DSC study, no clear discontinuity indicating a first-order phase transition could be obtained for samples with diameter of 2.5 nm and below.

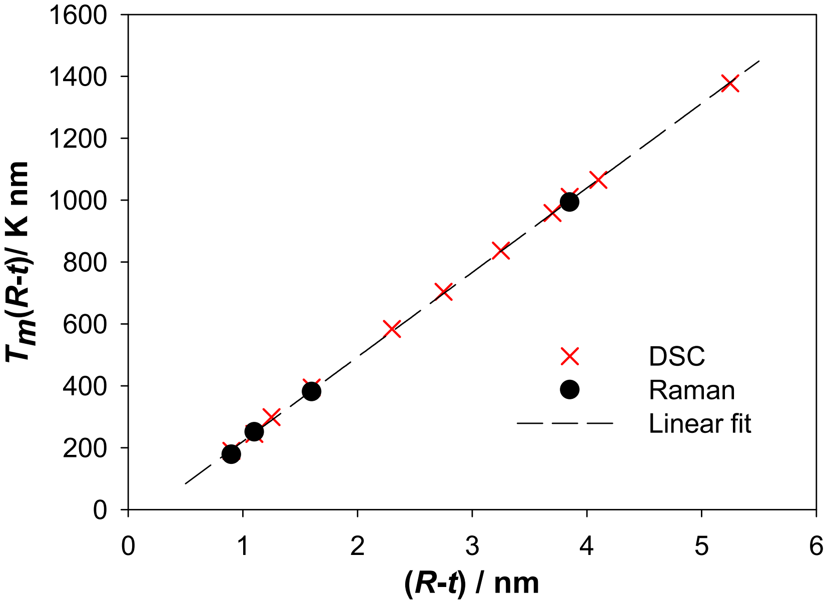

Figure 4.8: Correlation of the melting temperature T_m with an effective pore radius $(R - t)$, assuming a layer thickness $t = 0.6$ nm of non-freezable water. Crosses mark the DSC data from Refs. [Jahnert, 2008b, Schreiber, 2001]; points are obtained by the present Raman data analysis. The dashed line illustrates the linear regression described by Equation 4.3. Figure adapted from [Erko, 2011].

4.1.3 Analysis of the ice peak

Another remarkable finding becomes apparent from the detailed analysis of the mode V contribution as a function of temperature and confinement. As mentioned earlier, this mode represents strongly HB oscillators in an icelike tetrahedral water network, as present in hexagonal, cubic, and (low density) amorphous ice. We therefore denote this peak as ice-peak in the following. Figure 4.9 shows the spectral position and width (full width at half maximum, or FWHM) of the ice-peak plotted as a function of temperature for samples of different pore widths. For all samples, the peak position shifts to a lower wave number and the peak width decreases as the temperature decreases. Figure 4.9 also shows that decreasing the pore size at a given temperature causes a shift of the peak position to higher wave numbers Figure 4.9(A) and a broadening of the peak Figure 4.9(B). Raman and FTIR OHS spectra of bulk crystalline ice and low-density amorphous ice (LDA) have been reported in earlier studies [Sivakumar, 1978b, Venkatesh, 1975]. The values of the spectral position and width of the ice-peak of crystalline and amorphous bulk ice reported in literature are included in Figure 4.9. Apparently, these curves seem to determine the bounds of our experimental data, with water in the 8.9 nm pores almost corresponding to bulk crystalline ice and water in the 2.0 nm pores almost corresponding to vapour-deposited LDA.

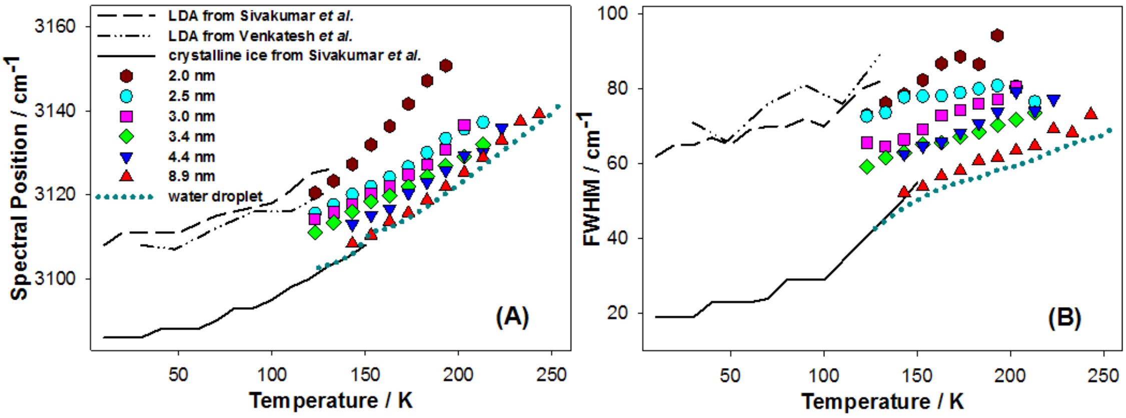

Figure 4.9: Temperature dependence of the ice-peak characteristics for confinement in pores of different sizes. (A) Fitted spectral position, and (B) FWHM for the measurements of the single water droplet (dotted line) and for water in six confinement dimensions (symbols). Also shown are the data attributed to crystalline (solid line) and amorphous (dashed line) solid water from [Sivakumar, 1978b] and [Venkatesh, 1975]. Figure adapted from [Erko, 2011].

Further analysis of the OHS spectrum also reveals that the intensity contribution of the ice-peak, defined as the ratio of the area of mode V divided by the total OHS area, changes with the degree of confinement of water (see also Figure 4.5). The temperature development of this quantity for different confinement dimensions is shown in Figure 4.10. Interestingly, the relative area of the ice-peak increases linearly with decreasing temperature. Moreover, the slope of the curves in Figure 4.10 is similar for all studied confinement dimensions.

The curves are only shifted in temperature, giving a systematic picture at a fixed temperature. According to that, the relative contribution of the ice-peak is largest for water in the widest pores and decreases systematically with decreasing pore size. This relation holds for the entire temperature range in which the ice-peak is observed. The relative peak area can be taken as a measure for the fraction of molecules in the respective vibrational mode. Hence, we may infer that there are two populations of water molecules in the pores: one forming a strong HB tetrahedral

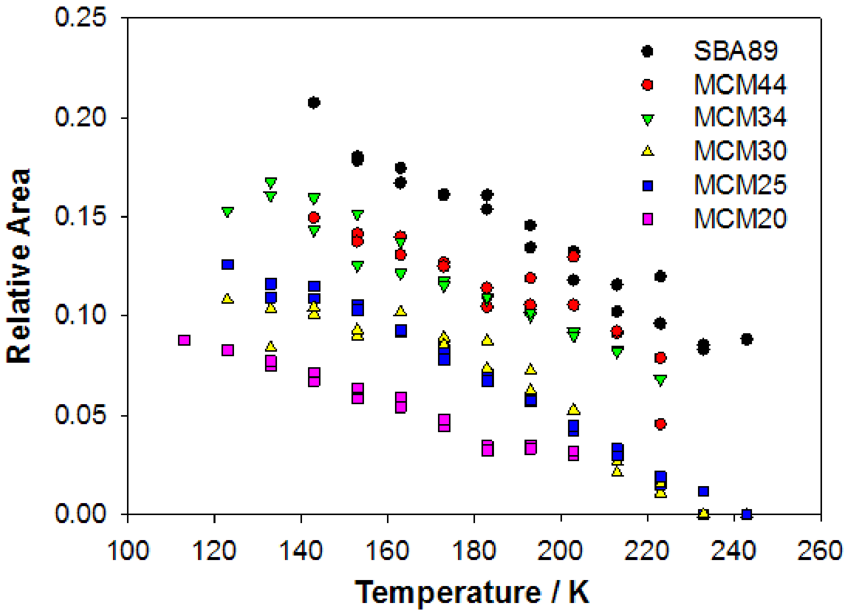

Figure 4.10: Temperature behaviour of the relative area of the OHS mode V (A(mode V)/A(total)) for different confinement dimensions.

water network and the other not forming such a network. On the basis of the results presented in Figure 4.8, we propose that these two populations represent the water in the core of the pores and the layer of non-freezable water at the pore walls, which is often termed interfacial water [Brovchenko & Oleinikova, 2008]. Assuming that the layer thickness t is independent of the pore radius R, as suggested by Figure 4.8, and that a layer of similar thickness exists in the smallest pores, we can estimate the volume fraction of water in the core of the pores, which we call core water, by $\varphi = (R - t)^2/R^2$. A plot of the relative area of the ice-peak versus the volume fraction of core water, adopting a layer thickness $t = 0.6$ nm, is shown in Figure 4.11 for a fixed temperature of 173 K.

Remarkably, a linear relationship is obtained for the entire set of samples, including those with smallest pore diameters (2.5 and 2.0 nm) and the bulk water droplet, for which the fraction of core water was set to 1. A linear relationship as in Figure 4.11 holds for all temperatures for the set of samples in which the ice-peak was present at that particular temperature. The error bars in Figure 4.11 indicate the estimated error in the determination of the relative area of the ice-peak (vertical bars) and the changes in the calculated fraction of core water resulting from an estimated uncertainty of the layer thickness t of non-freezable water of 0.1 nm (horizontal bars). The linear relation between the relative peak area of the ice-peak and the volume fraction of the core water also holds for these higher or lower values of the layer thickness. Moreover, the graph for the lower layer thickness ($t = 0.5$ nm), indicated by the dashed line in Figure 4.11, passes through the origin - as would be

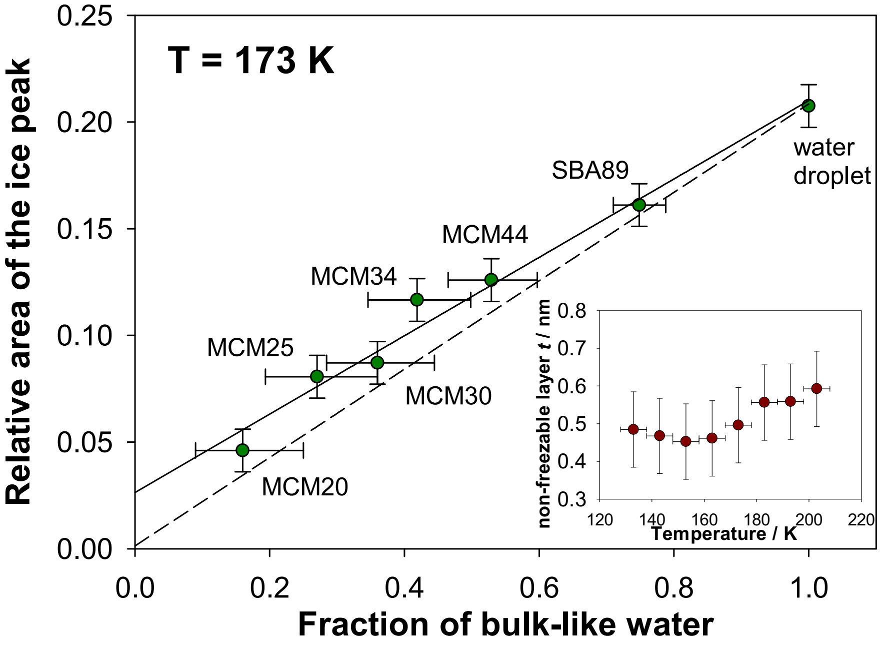

Figure 4.11: The relative area of the ice-peak is directly proportional to the fraction of core water within the pores of different sizes. The solid line is a linear fit for $t = 0.6$ nm. The dashed line shows the fit for a decrease of the layer thickness t by 0.1 nm. The inset shows the temperature dependence of t. Figure adapted from [Erko, 2011].

expected if the non-freezable wall layer is assumed not to contribute to the ice-peak. The appropriate values for the non-freezable layer thickness for other temperatures are shown in the inset of Figure 4.11. The deviation of our Raman OHS data from the DSC data in Figure 4.8 in this case is still well within the combined experimental uncertainty of the two independent methods.

4.1.4 Discussion

We performed a systematic study of the effect of confinement on freezing and melting of water in cylindrical silica nanopores using Raman scattering. These findings confirm results from earlier studies [D'Arrigo, 1981, Furic & Volovsek, 2010, Sivakumar, 1977, Sivakumar, 1978b, Sivakumar, 1978a, Walrafen, 1964] and allow us to draw new conclusions based on the systematic change of confinement dimensions from 8.9 to 2 nm. Raman spectra in the OHS region of water show pronounced changes in the population of the individual stretching modes on confinement. At room temperature, the population of high-energy vibrations increases with confinement (Figure 4.3). This high-energy contribution can be attributed to weakly connected water molecules [Brubach, 2005, Sun & Zheng, 2009]. Accordingly, confinement appears to weaken the connectivity of the HB network of water molecules, resulting in an increase of their mobility. This effect is consistent with results from NMR measurements [Liu, 2006, Webber, 2007]. Significant changes of the OHS Raman signal are observed during cooling and heating in the temperature range between 123 and 303 K. The temperature-induced changes in the OHS spectrum are indicative for the changes of the intramolecular bonding within the water network. The position and width, as well as the relative intensities of all spectral components, change systematically with temperature. With decreasing temperature, the non-HB oscillations are successively replaced by those of a HB network, leading to a relative increase of the intensity of the components with lower wave numbers. This temperature-induced change in the network of water molecules also influences the strength of the molecular oscillators and leads to a shift in the spectral position of the OHS modes. Temperature-induced ordering and disordering of water molecules lead to, respectively, narrowing and broadening of each contribution peak. These effects also show a systematic dependence on confinement dimensions. For bulk water and water confined in pores larger than 2.5 nm, the development of the OHS mode I contribution with temperature can be used to determine the liquid–solid phase transition temperature from the discontinuous change of the spectral position (Figure 4.7) and the width of the peak (data not shown). Phase transition temperatures obtained by this method are in excellent agreement with those from DSC measurements performed independently on the same samples [Findenegg, 2008, Jahnert, 2008b]. This close agreement confirms the finding in [Jahnert, 2008b] that the parameter C of Equation 4.2 agrees reasonably with the Gibbs-Thomson constant as derived from thermodynamic parameters of bulk water: $C_{GT} = 2T_0\sigma_{sl}V^M/\Delta H^M = 54$ K nm, where T_0 is the melting temperature, σ_{sl}, is the free energy per unit area of the liquid–solid interface, V^M is the molar volume of the liquid phase, and ΔH^M is the molar enthalpy of melting. It is remarkable that the thermodynamic Gibbs-Thomson equation is applicable down to the nanometer regime when we allow for the existence of a non-freezable layer of water at the pore walls. In agreement with the DSC study, we find that at the pore walls of hydrophilic silica in MCM-41 and SBA-15, the thickness of this layer corresponds to about two monolayers of water molecules. Strong interfacial-bound water layers of similar thickness where also reported for Vycor porous glass [Gruener, 2009], and the existence of a quasiliquid water layer was reported for planar silica surfaces [Engemann, 2004]. The magnitude of the discontinuous step in the spectral position and width of the OHS mode I decreases with decreasing pore size, showing essentially the same trend as the exothermic/endothermic heat transfer measured in DSC [Jahnert, 2008b]. For water confined in pores of a 2.5 nm diameter, a slight discontinuity in the spectrum is perhaps present but is no longer quantifiable. In pores of a 2.0 nm diameter, both the position and the width of the OHS mode I change smoothly with temperature in the range between 123 and 303 K. This observation supports the conjecture of a continuous liquid–solid phase transition of water in narrow pores [Morishige & Kawano, 1999]. This effect should in some way be connected to the existence of a non-freezing water layer close to the pore wall.

To assess the significance of the vanishing step in the OHS mode I parameters more quantitatively, the step height should be normalised by the amount of water in the core volume. A non-freezing water layer of a 0.6 nm thickness in pores of a 2.5 or 2.0 nm diameter leaves a core volume fraction of 27% and of 16%, respectively, in which the water may freeze. In both cases, the amount of water in the core volume is well above the limit of experimental resolution of DSC and Raman measurements. The analysis of the DSC data revealed that the (molar) enthalpy of melting ΔH^M of water sharply decreases with decreasing core radius $(R-t)$ and disappears at an estimated pore diameter of 2.7 nm [Jahnert, 2009]. The value of the limiting pore diameter derived from the DSC data in this way somewhat depends on the value of the layer thickness t, which can only be determined indirectly. In this respect, the determination of the limiting pore diameter from the Raman OHS spectra is more direct, because it is based on the direct detection of the disappearance of a step in the position and width of the mode I spectra. In this way we definitively found that no first-order phase transition occurs in pores of diameters smaller than 2.5 nm. Hence, the two methods yield concordant results for the limiting pore diameter of a first-order freezing transition of water. In this context, the population of the ice-peak (mode V) scales linearly with the estimated fraction of core water, according to $\varphi = (R-t)^2/R^2$, when assuming the same value of the layer thickness of non-freezing water as in the analysis of the mode I spectra (Figure 4.7). Although a slight temperature dependence of t seems to be present (inset in Figure 4.11), this result suggests that water in the pores consists of two spatially separated phases irrespective of the pore size. The interfacial water near the pore walls consists of non- or weakly HB water molecules, contributing essentially to the high-energy part of the OHS spectrum (modes II–IV). The relative fraction of water in the core of the pore space consequently decreases with decreasing pore size. From the viewpoint of dynamics, this seems to imply that there should be no essential difference in the dynamic behaviour of bulk water and confined core water, even in very small pores. In a similar context, the term “free” water with bulklike properties was introduced by Gallo *et al.* [Gallo, 2010b, Gallo, 2010a] and was used to argue that results obtained from strongly confined water can be taken to predict bulk water behaviour in the no man’s land [Xu, 2009]. However, an important conclusion from the analysis of the Raman ice-peak is that the structure of water in the core of the pores changes with the degree of confinement, which should therefore not be considered bulklike. This follows from a comparison of the parameters of the ice-peak in the pores with the corresponding values for bulk samples of crystalline ice and vapour-deposited LDA reported by Sivakumar *et al.* [Sivakumar, 1978b]. This in turn leads to the conclusion that, upon cooling, the core water in large pores undergoes a first-order phase transition, forming crystalline ice similar to bulk ice. For water confined in pores of a smaller pore size, a shift of the spectral position and peak width toward the values attributed to LDA as reported in [Sivakumar, 1978b] and in [Venkatesh, 1975] is observed. In the pores of a 2.0 nm diameter, we observe a signal that corresponds closely to the one of bulk LDA. From this, we conclude that there is a continuous transition from crystalline ice for weak confinement (8.9

nm pores) to LDA for strong confinement (2 nm pores). Hence, our results indicate a confinement-induced structural change of the core water with decreasing pore size. A similar continuous transition of confined water from liquid to solid has previously been reported from X-ray diffraction measurements and was interpreted as a “new type of phase transition” [Morishige & Kawano, 1999].

Finally, distinct differences in the dynamics of bulk water and confined water can also be deduced from the spectral region around 1600 cm^{-1}, which represents the HOH-bending mode of water molecules. For bulk water, the disappearance of the HOH-bending peak upon freezing has been attributed to the sudden increase of the molecular connectivity [Franks, 1975]. In our experiments (Figure 4.2), the HOH-bending peak was present at all temperatures down to 123 K, even in the widest pores of the SBA-15 sample (8.9 nm pore diameter). Only for the bulk water droplet did the HOH peak completely vanish upon freezing, in accordance with other investigations. Therefore, we stress that this spectral signature (similar to the appearance/disappearance of the ice-peak) cannot be used to uniquely determine the liquid state of water in pores, as was proposed by Mallamace and co-workers in [Mallamace, 2007b]. Nevertheless, further work is needed for a more quantitative analysis of the effect of confinement on the weak HOH-bending signal.

4.1.5 Conclusions

We presented experimental evidence that the strong interaction of water molecules with the walls of the cylindrical nanopores of SBA-15 and MCM-41 leads to a non-freezable water layer of approximately 0.6 nm thickness. This layer contributes to the high-energy part of the OHS spectrum only, indicating a weakly HB water structure without any tetrahedral coordination. In contrast, the water confined within the core of the cylindrical pores shows at low temperatures the fingerprint of HB, tetrahedrally coordinated water represented by the Raman mode V or ice-peak in the low-energy region of the OHS spectrum. This core water shows a continuous structural change from crystalline ice for large (8.9 nm) pores toward LDA for very small (2 nm) pores. In view of these two spatially separated water populations in the pores, and because the intrinsic structure of the core water depends on the degree of confinement, we conclude that it will be rather difficult to extract information about the state of bulk liquid water in the no man’s land from studies of water confined in nanopores [Mishima & Stanley, 1998].

4.2 Density minimum of confined water

Combined data from *in situ* small-angle scattering of X-rays (SAXS) and neutrons (SANS) are corroborated by additional wide-angle X-ray scattering (WAXS). Hereby, the small-angle signal shows the Bragg peak intensity from the mesoporous lattice, that at wide angles corresponds to the intermolecular scattering of water in mesopores. The influence of confinement dimensions on the development of the scattering intensity with temperature is analysed and discussed in this section.

4.2.1 Scattering data

For all three independent experiments the scattering intensity $I(q)$ shows characteristic changes with temperature. A temperature shift (hysteresis) between cooling and heating is observed. All data presented within this work correspond to the heating cycle, but the results are valid also for the cooling cycles. Figure 4.12 shows exemplary scattering patterns for water confined in MCM34 for two selected temperatures. The development of the wide-angle X-ray scattering (WAXS) signal for MCM34 is shown in Figure 4.12(a). We performed a peak fit to the first intensity maximum between 15 nm^{-1} and 22 nm^{-1}. Unfortunately, the instrument was not calibrated very precisely to absolute q-values. Therefore, the fitted values for the peak position obtained for the largest pore size at the lowest temperature were used for the normalisation of the data to the known q-position of cubic ice [Dowell & Rinfret, 1960].

A plot of the peak height, the peak width and its position as a function of temperature are shown in Figure 4.13 for all four samples. The observed step in the peak intensity is accompanied by a discontinuous change of the width and the position of the peak. The discontinuity of the WAXS parameters for MCM34, MCM39 and MCM44 coincides well with the phase transition temperature (dashed lines) measured by independent DSC-[Findenegg, 2008] and Raman measurements in section 4.1 on the same samples. The sudden peak broadening, intensity decrease, and peak shift in the WAXS region can therefore be used as a signature of the first-order melting transition of water inside the pores. As in the DSC-[Findenegg, 2008] and the Raman studies from section 4.1 also the WAXS data show no clear discontinuity, but rather a continuous change for water confined in 2.0 nm wide pores, indicating the absence of a first-order melting transition in this case.

The small-angle scattering signal (Figure 4.12(b) and (c)) shows well-pronounced Bragg peaks resulting from the two-dimensional hexagonal mesopore lattice. The high brilliance and the excellent resolution of the synchrotron source allow highly accurate measurements of several Bragg peak orders. Unfortunately, in the neutron experiments only the first order Bragg peak could be measured due to the small q-range covered by the detector and insufficient beamtime available (Figure 4.12(c)).

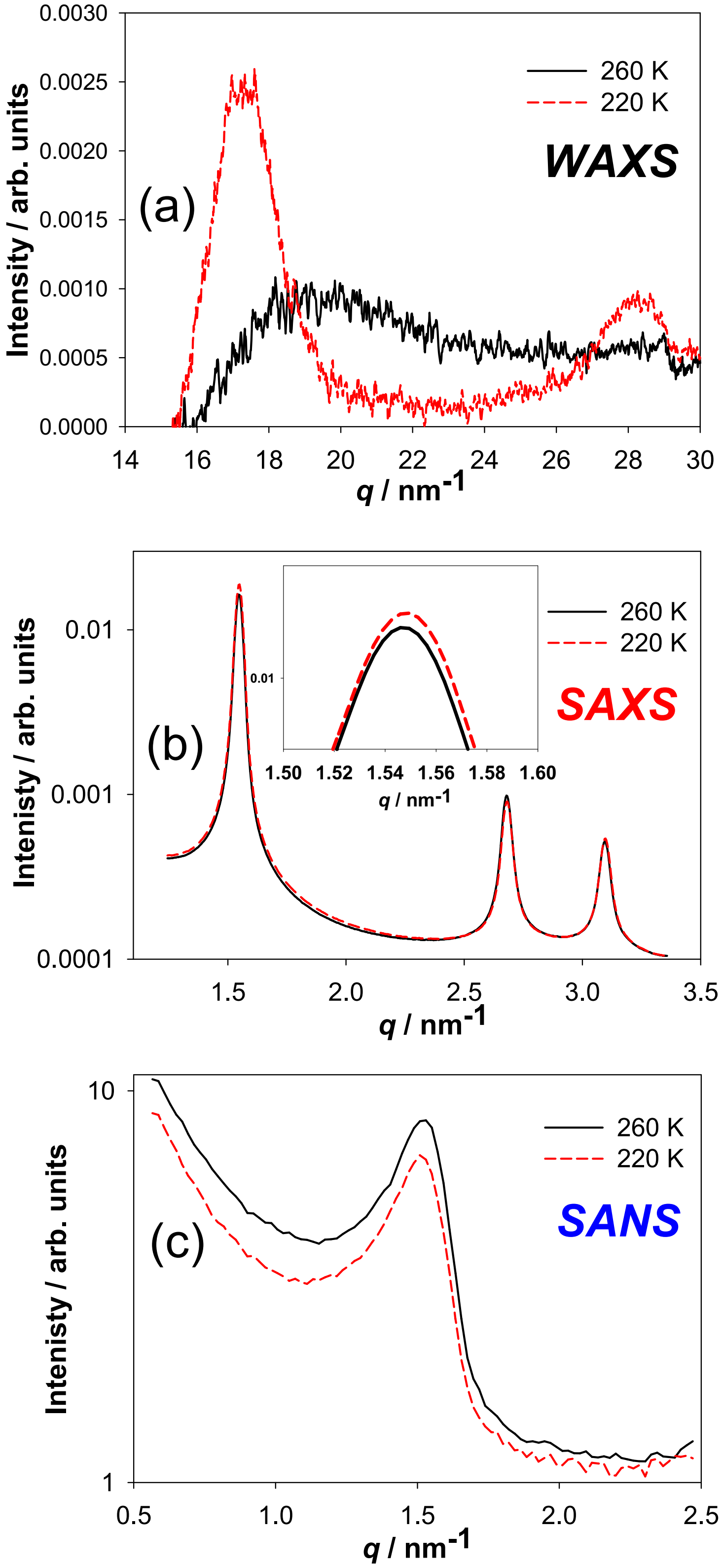

Figure 4.12: Scattering patterns for MCM34 for two different temperatures above (black) and below (red) the melting transition temperature. (a) WAXS, (b) SAXS, (c) SANS. Figure adapted from [Erko, 2012a].

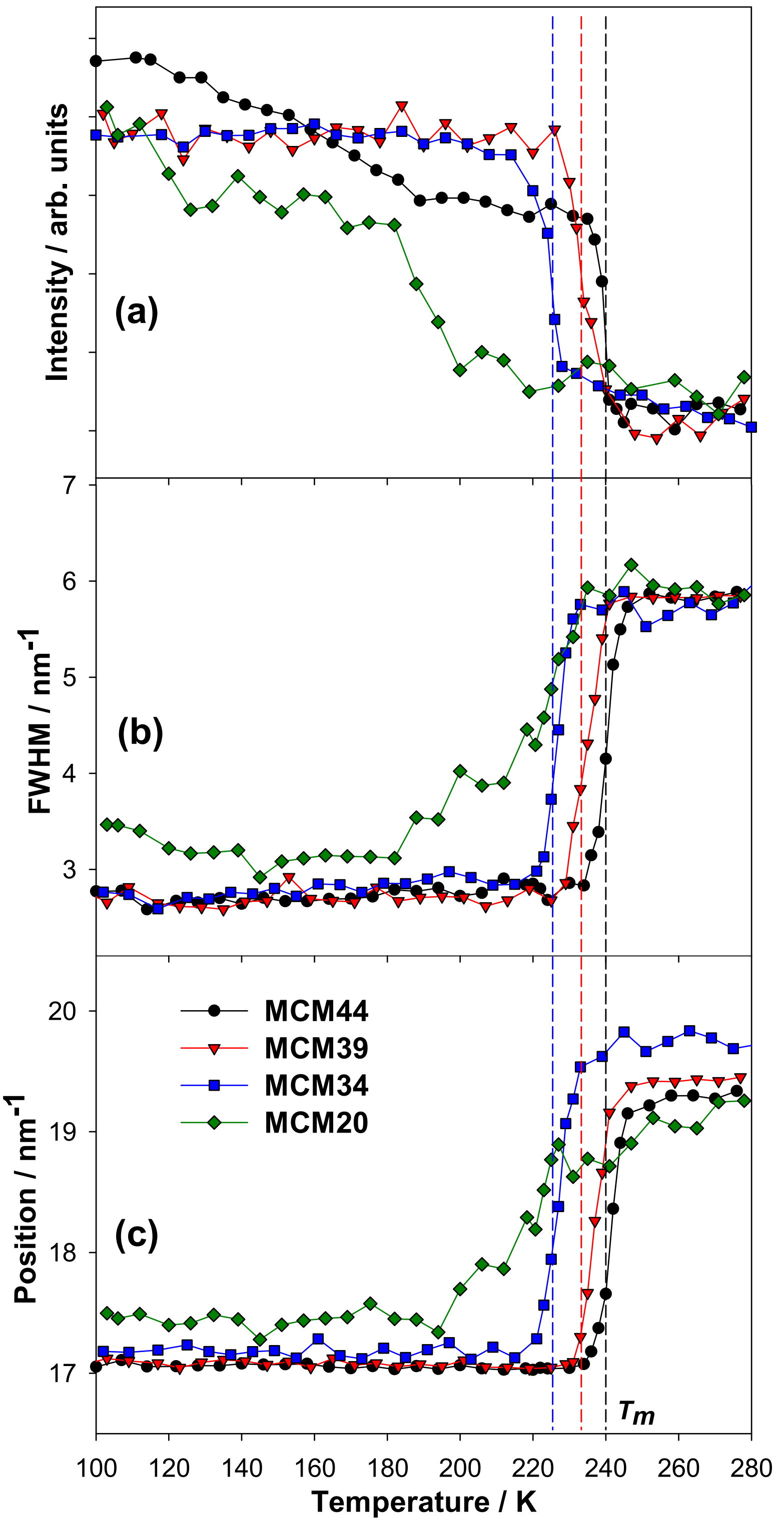

Figure 4.13: Temperature dependence of the WAXS signal. The plot shows fitted values of the peak intensity (a), peak width (b) and peak position (c). The corresponding pore size-dependent water melting temperatures T_m from Ref. [Jahnert, 2008b] are indicated by the vertical dashed lines. Figure adapted from [Erko, 2012a].

The SAXS intensities of the individual Bragg peaks, normalised to the intensity measured at $T = 100$ K, are shown in Figure 4.14(a) for MCM34 as a function of temperature. The corresponding (10) Bragg peak intensity for the same sample measured with SANS is shown in Figure 4.14(b). The SAXS data exhibit an intensity maximumat about 220 K, and the SANS data show a minimum in the same temperature region. These extremes roughly correspond to the temperature where the jump in the WAXS parameters occurs. Taking into account the aforementioned coincidence of this jump with the phase transition temperature, the intensity maxima and minima in SAXS and SANS, respectively, can be attributed to the melting transition of water in MCM34. All other samples show essentially the same temperature behavior of the scattering signal. However, the points of the intensity maxima and minima are shifted in temperature similar to the WAXS parameters.

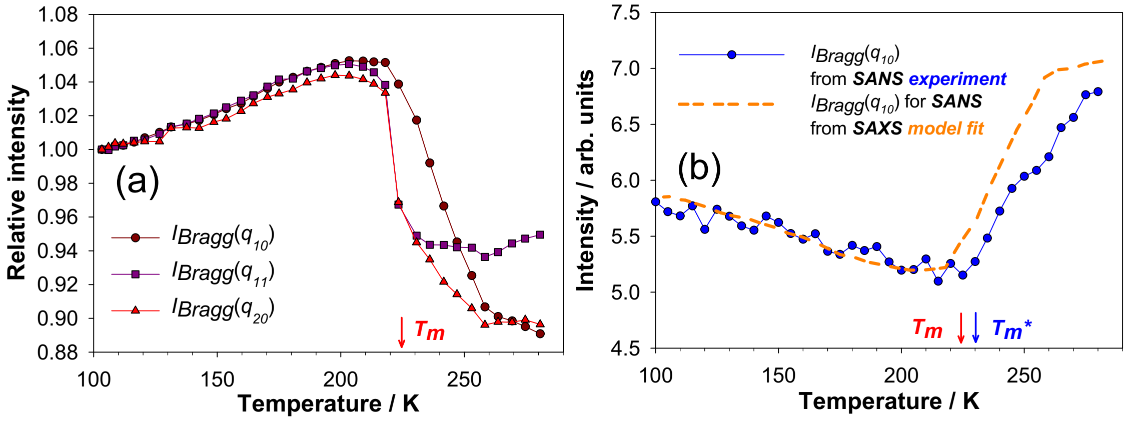

Figure 4.14: Temperature dependence of the scattering intensity of individual reflections during heating. (a) Peak height for the three reflections (10), (11) and (20) of the mesopore lattice measured with SAXS. (b) Peak height of the (10) mesopore lattice reflection measured with SANS, together with the predicted SANS data from the model fit of the SAXS data (Section IV). Water melting temperatures as observed in DSC [Jahnert, 2008b] are indicated as T_m for H_2O and T_m^* for D_2O, respectively. Figure taken from [Erko, 2012a].

In a two-phase approximation (i.e. water of homogeneous density within the cylindrical mesopores of the homogeneous silica matrix), the Bragg peak intensity from the pore lattice is proportional to the scattering contrast (i.e. the square of the scattering length density difference between the silica matrix and water). Due to the different interactions of neutrons and X-rays with matter, the scattering contrast of neutrons is different from that of X-rays. The density of solid silica does exhibit only negligible dependence on temperature. The observed changes in Figure 4.14 can therefore be attributed to changes in the scattering length density (which is related to the mass density) of water within the pores.

In the SANS experiment the (10) Bragg peak intensity changes in the opposite way with temperature as compared to the SAXS measurements. Moreover, the

SAXS signal (Figure 4.14(a)) shows different temperature behavior for each of the three Bragg peaks. This last observation implies in particular that the intensity changes cannot be described simply by a two-phase system, since then all reflections should show exactly the same temperature dependence. A non-homogeneous water distribution within mesopores was already suggested earlier to be fully in-line with neutron scattering experiments on confined water [Mancinelli, 2010a].

4.2.2 Density distribution

Several experimental [Schreiber, 2001, Findenegg, 2008, Mancinelli, 2009] and theoretical [Lombardo, 2008, Brovchenko & Oleinikova, 2008, Gallo, 2010b] studies of water in hydrophilic nano-confinement give evidence of a wall layer of approximately two water molecules exhibiting a different density than the core water. We therefore assume a simple core–shell type density distribution of the water, which is compatible with our earlier work (see section 4.1), and qualitatively also with Ref. [Mancinelli, 2010b]. In order to describe the temperature dependence of the integrated intensity, we adapt the step-density model from Ref. [Zickler, 2006], and apply it to the SAXS and SANS data simultaneously. In the model, one phase represents the silica matrix, the second the water in the vicinity of the pore walls, (surface water), and the third phase describes the water in the inner part of the pore (core water). For MCM-41 and other hydrophilic confinement the strong attraction of water by the substrate leads to an increased water density close to pore walls [Svergun, 1998, Merzel & Smith, 2002, Mancinelli, 2010a], and therefore to an increased scattering length density (sld) as compared to bulk water under ambient conditions. The scattering length density ρ, describing the interaction strength of a substance with the X-rays or neutrons, is directly proportional to its mass density ρ_m (see Equation 2.41). The mass densities for bulk water and silica at 277 K and the corresponding scattering length densities for X-rays and neutrons are summarised in Table 2.3.

The scattering intensity $I(q)$ for a system of monodisperse, hexagonally packed, water filled pores with average sld ρ_{al} in a silica matrix with sld ρ_s can generally be expressed by Equation 2.32, with $\Delta\rho = \rho_{al} - \rho_s$. For a perfect two-dimensional hexagonal lattice, the structure factor $S(q)$ gives non-vanishing intensity contributions only at the position of individual Bragg reflections, $S(q_{hk}) \propto 1/q_{hk}^2$, and is zero otherwise. Due to finite experimental resolution, these delta functions are broadened and can be represented by Gaussian or Voigt functions [Zickler, 2006]. The square of the form factor $|F(q)|^2$ determines the height of the Bragg peaks and is for a number N of nested cylindrical shells expressed by Equation 2.30, with $Z(qR) = 2J_1(qR)/(qR)$, where $J_1(qR)$ is the "ordinary" Bessel function of the first kind. The sld profile of the three-phase model ($N = 2$) based on fitted results for MCM34 at 220 K is sketched in Figure 4.15. The scattering length densities corresponding to Equation 2.30 are: ρ_0: silica matrix, ρ_1: surface water and ρ_2: core water. $(R_1 - R_2)$ corresponds to the thickness of the surface water shell and R_2

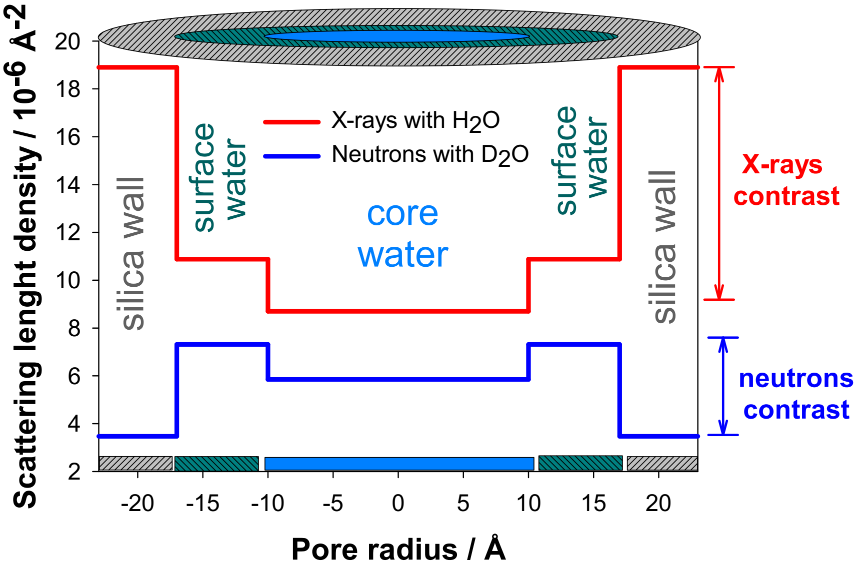

Figure 4.15: Scattering length density profile for water-filled MCM34 at 220 K obtained from the SAXS data fit using Equation 2.32 and Equation 2.30 (red). From this, the expected sld for neutrons can be calculated on the basis of Equation 2.41 (blue). A water density change leads to the opposite contrast scenario for neutrons and X-rays, respectively. Figure taken from [Erko, 2012a].

to the pore radius occupied by core water. The values for the pore radius R_1 of each sample are taken from earlier nitrogen sorption experiments [Jahnert, 2008b]. Uncertainties occur particularly in the not very precisely known density of the silica walls (see e.g. Ref. [Fan, 2007]).

If we assume a constant value of the sld of silica from Table 2.3, Equation 2.32 can be used to fit the experimental data for the three Bragg peaks$I_{Bragg}(q_{hk})$ from SAXS using the least square method. The value for the average water scattering length density ρ_{al} is hereby given by:

$$\rho_{al} = \frac{\rho_1(R_1^2 - R_2^2) + \rho_2 R_2^2}{R_1^2} \tag{4.4}$$

Starting with the measurements at 280 K, the best fit for the parameters K, ρ_1 and R_2 can be obtained. Since the value of K in Equation 2.32 cannot be determined from the experiments (no absolute intensity calibration was made), the fit was performed with $\rho_2 = 9.46 \cdot 10^{-6}\text{Å}^{-2}$, assuming the mass density of core water being identical to the bulk water value at 280 K. For the subsequently measured temperature series, the parameter K was kept constant, fitting the parameters ρ_1, ρ_2 and R_2 to the SAXS data. According to this, the three-phase model provides the temperature dependence of three characteristic parameters, i.e. the thickness of the surface water layer and the scattering length densities - and thus the mass densities - of the surface water and the core water within the pores. Figure 4.16 shows the fit results for the temperature dependence of the core water density for the three different confinement dimensions for which three Bragg reflections could be measured (for MCM20, only the (10) reflection could be observed). These data are shown together with the bulk density for supercooled water and for bulk hexagonal ice taken from the literature [Landolt & Boernstein, 1977, Hare & Sorensen, 1987]. For temperatures below 280 K the density of core water decreases continuously until it steeply drops at the phase transition temperature T_m. This density drop is clearly pronounced for MCM44, gets smaller for MCM39, and is practically absent for MCM34. For temperatures below T_m the core water density for all samples increases again resulting in a density minimum situated slightly below the liquid–solid phase transition temperature T_m measured by DSC [Jahnert, 2008b] and by WAXS in this work. The total magnitude of the density change does not vary much with the confinement dimension. The temperature behaviour of the core water density below T_m closely corresponds to that expected for bulk hexagonal ice [Landolt & Boernstein, 1977].

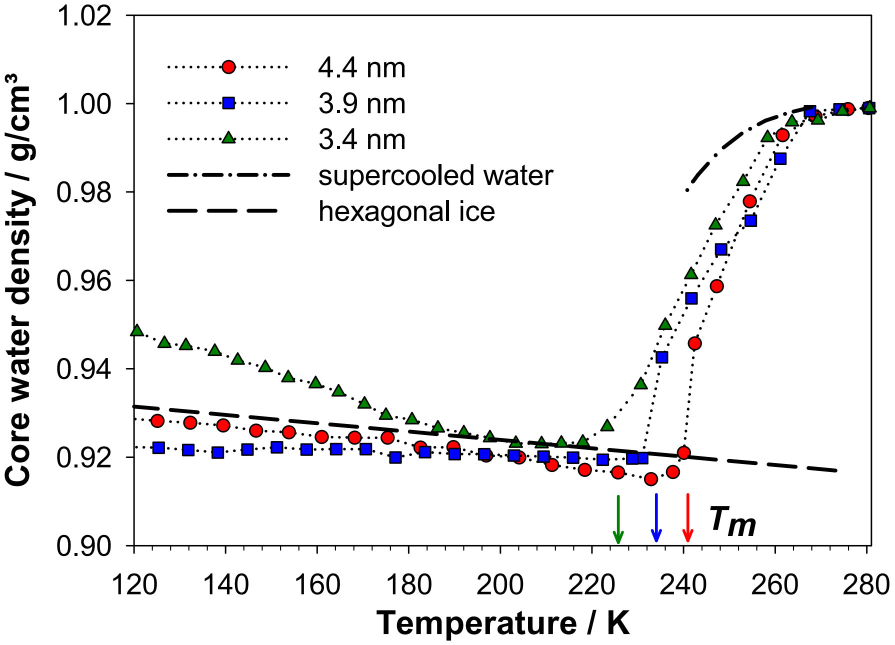

Figure 4.16: Core water density from the SAXS data model together with the corresponding values for supercooled bulk water [Hare & Sorensen, 1987] and bulk hexagonal ice [Landolt & Boernstein, 1977]. Figure taken from [Erko, 2012a].

A surface water layer of 0.70 ± 0.05 nm is found for all three investigated samples. The thickness of the surface layer does not change with temperature within the margins of error. The respective mass density values are slightly different for the different samples ranging between 1.07-1.14 g cm^{-3}. The temperature dependence of the surface layer mass density shows qualitatively similar behaviour as the core water. However, the observed magnitude of the density change of the core water is about three times larger than that of the surface water.

We use the complementary information from X-rays and neutrons to perform an independent cross-check for our model. From the water density distribution obtained from SAXS we calculate the corresponding neutron scattering intensity for D_2O. The resulting dependence of the SANS intensity on temperature for MCM34 is shown in Figure 4.14(b). The two curves almost perfectly coincide except a temperature shift of 5–10 K towards higher temperatures for the SANS experiment. This is understood by the fact that the calculated curve is based on SAXS data measured on confined H_2O. SANS experiments, however, were performed with D_2O. The density maxima of the two water types in bulk water are also shifted by around 7 K (277 K for H_2O and 284 K for D_2O), and the melting temperature of bulk D_2O is about 4 K higher than that of bulk H_2O. Moreover, a shift of the same order in T_m was also reported from DSC measurements on confined D_2O and H_2O, respectively [Jahnert, 2008b]. Consequently, the observed temperature shift is attributed to the two different water types used in the two independent experiments. This shows that the results obtained from our model are confirmed by both independent scattering experiments.

A detailed determination of the water density distribution according to the three-phase model could be performed only for the samples MCM44, MCM39 and MCM34 which showed at least three Bragg peaks in the X-ray scattering pattern. Unfortunately, for the sample MCM20 with the smallest pore size only the first order Bragg peak could be resolved due to the low pore ordering. Therefore, no detailed water density distribution, and particularly no core water density could be extracted for the smallest pores under investigation here. The temperature dependence of the (10) Bragg peak intensity for the MCM20 sample is shown in Figure 4.17 for both, SANS and SAXS, respectively. Also for water confined in these two-nanometer pores, the Bragg peak intensities from SANS and SAXS show the expected reversed temperature behavior justified by the respective contrast scenario in Figure 4.15. Similar to Figure 4.14(b), the two curves are slightly shifted in temperature. The minimum SANS intensity is observed in the temperature range between 170 K and 190 K, while the maximum SAXS intensity is at about 160 K. This strongly indicated a density minimum of water also in the 2.0 nm pores, similar to the other three samples (Figure 4.16). We recall that no sign of a first order phase transition was found in this sample, neither from the WAXS data (Figure 4.13), nor from DSC [Findenegg, 2008, Jahnert, 2008b] or Raman measurements from section 4.1. An interesting observation concerns also the extremal values of the intensity at around 250 K (SANS) and 240 K (SAXS), indicating the presence of a corresponding water density maximum.

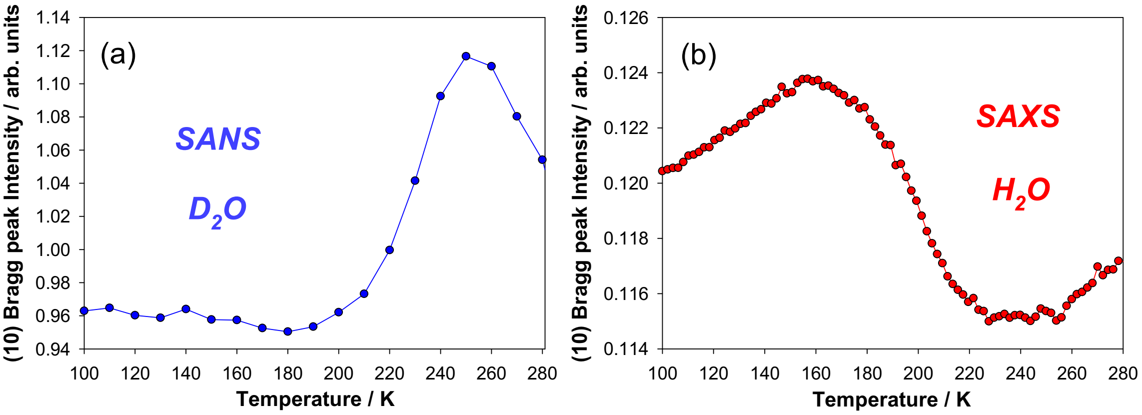

Figure 4.17: (10) Bragg peak intensity from SANS (a) and SAXS (b), respectively, for the sample with 2.0 nm pore diameter (MCM20). The intensity change of X-ray and neutron data with temperature suggests a density maximum situated at high temperatures and a density minimum at low temperatures. Figure taken from [Erko, 2012a].

4.2.3 Discussion

This work presents a systematic study of confinement effects on water freezing using small-angle neutron (SANS), small-angle X-ray (SAXS) and wide-angle X-ray (WAXS) scattering. The wide-angle scattering signal results from the intermolecular structure factor of the water network. For water in its liquid state the WAXS signal is weak and strongly broadened with a first maximum at around $q = 19.5\ \mathrm{nm}^{-1}$, qualitatively similar to the structure factor of bulk water. From earlier work on similar systems it is known that water in mesopores freezes into cubic ice with the first Bragg peak at around $q = 17\ \mathrm{nm}^{-1}$ [Bellissent-Funel, 1993, Morishige & Nobuoka, 1997]. Therefore, for the three samples with the largest pore sizes the discontinuous change of the WAXS peak position directly indicates the liquid–solid first order phase transition of water in the pores. For the sample with 2.0 nm pore diameter, however, the WAXS parameters (position, width and height) change only gradually with temperature. A plausible explanation consistent with numerous other investigations (e.g. the absence of freezing peaks in DSC) is that water does not transform into a crystalline phase if the pore size is clearly below 3 nm. However, it should be noted that diffraction from a crystallite of only 2 nm diameter already leads to considerable broadening of the WAXS signal. Taking additionally into account two non-freezable wall layers of roughly 1 nm in total, only about 1 nm (i.e. less than three molecules of water across) would remain to define the thickness of the crystallite. This makes it impossible to identify or exclude a crystalline phase by WAXS which has already been discussed in earlier work [Morishige & Kawano, 1999, Mancinelli, 2010a]. However, our previous Raman study on the same materials (see section 4.1) gives clear evidence of the gradual development of a low-density amorphous (LDA) ice-like hydrogen bond network for the core water in pores below 3 nm pore size. We therefore strongly believe that the water structure within the smallest pores is not crystalline in the entire temperature region. For water confined in larger pores, the phase transition signature from WAXS (Figure 4.13) coincides perfectly with the independent DSC and Raman measurements.

Previous analysis of small-angle neutron scattering data was performed assuming a homogeneous distribution of water in the mesopores [Liu, 2007, Zhang, 2009], and a density minimum was observed at about 210 K for hydrophilic pores of 1.5 nm in diameter. It was one of the major aims of the present work to systematically investigate the occurrence of a density minimum in MCM-41 samples with different pore diameters, in order to understand and discuss this effect more in detail. Our SAXS data clearly demonstrate that the assumption of a homogeneous water density within the pores is not correct. At least two separated density regions of water within the pores must be considered, in accordance with our Raman study in section 4.1, and with neutron scattering experiments performed by other groups [Mancinelli, 2010b]. A simple model analysis of the SAXS data is consistent with a wall-layer of approximately two water molecules with larger mass density as compared to the core water. Such interfacial-bound quasi-liquid water layers with comparable thickness were also reported from several other studies, e.g. in MCM-41 [Mancinelli, 2010a], Vycor porous glass [Gruener, 2009] and planar silica surfaces [Engemann, 2004]. Surprisingly, our results for the surface water show qualitatively the same temperature dependence as observed for the core water, its magnitude being, however, much smaller (by a factor of three). We suggest that the observed effect of the wall layer density change may be due to our model restrictions. We motivate this interpretation by our recent observation that - contrary to the core water - the surface water does not develop a strong hydrogen bond network upon cooling (see section 4.1). Therefore, we do not expect distinct density changes with temperature for the wall layer. A data fit with a constant density for the wall layer only changes the quantitative values of the core water density, while the qualitative temperature behaviour, including the position of the density minima, remains unchanged. However, the fit quality gets worse compared to that including a change in surface water density. A more detailed analysis, such as proposed in Refs. [Webber, 2008, Mancinelli, 2010b, Webber, 2010] would have to go beyond the two-step model applied here, implying also the measurement of more than just three Bragg-reflections with high accuracy. Such improved experiments including advanced modelling of higher order reflections are however beyond this study.

Nevertheless, the core water in our investigations consistently shows a density minimum, similar to the one found by Liu *et al.* [Liu, 2007]. However, we observe this density minimum for all our samples, not only for the smallest ones where no freezing transition takes place. Notably, the position of the density minimum depends on the pore size, shifting to lower temperatures as the pore diameter decreases. For the larger pore diameters, where crystalline ice was clearly observed, the density minimum is related to the core water melting temperature, being roughly 10 K lower than the melting temperature determined by independent methods on the same samples (Figure 4.16). We point out that this density minimum is not surprising at all since bulk water shows exactly the same behaviour. Upon (under)cooling from 277 K, the bulk water density decreases first continuously and then abruptly at the freezing transition, followed by a density increase of the bulk ice upon further cooling (see Figure 4.16). Upon confinement, the magnitude of the discontinuous density drop of the core water at T_m decreases with decreasing pore size due to the increasing contribution from the (unfreezable) wall layer, essentially showing the same behaviour as the exothermic/endothermic heat transfer measured in DSC [Jahnert, 2008b], or the spectral changes in the OH-stretching region measured by Raman scattering in section 4.1.

The water density minimum at around 210 K reported by Liu *et al.* [Liu, 2007, Liu, 2008] has been measured for confining systems very similar to those in the present study (MCM-41S silica materials). The pore size reported in these studies was even smaller than the one of the smallest sample (MCM20) used in the present work. According to the results of our work, the density minimum for the 2.0 nm pores is at around 180 K, i.e. at considerably lower temperature as compared to the minimum at about 210 K observed by Liu *et al.* We find a minimum at about 210 K for MCM34, i.e. the sample with nominally 3.4 nm pore diameter, which is more than double the diameter of the Liu sample. We do not have a convincing explanation for this discrepancy. Although the method of determining the pore size might somehow influence the exact values for the pore radius, we do not expect a factor of two. Therefore, there remains a quantitative discrepancy between the results of Liu *et al.* and this work concerning the position of the water density minimum for very small pores. Our consistent data from SAXS and SANS are the result of two completely independent experiments with a different setup. Therefore, we can largely exclude experimental artefacts. Based on the modified Gibbs–Thomson equation (Equation 4.1), which was demonstrated to describe the melting point dependency on the pore size [Schreiber, 2001], one would expect the phase transition temperature for water in 2.0 nm pores to take place at around 210 K. Interestingly, this temperature exactly corresponds to that of the density minimum reported by Liu and co-workers. However, our data of the MCM20 sample do not show any apparent effect at this temperature. A possible explanation for the observed density minimum at around 160–180 K may be connected to the recently reported dynamical transition of the surface layer in MCM-41-S materials of a similar size, which takes place in the same temperature region [Bruni, 2011]. Unfortunately, for the smallest pore size we cannot unambiguously distinguish between the signal from the core water and that from the surface water. However, since the fraction of surface water within the pores of 2.0 nm size is around 84% (see section 4.1), the scattering signal in Figure 4.17 should mainly originate from this fraction. Moreover, similar experimental methods applied to pores with hydrophobic walls do no show evidence of a water density minimum in such small pores [Zhang, 2009]. Additionally, no discontinuous transition of core water in MCM20 was found by Raman scattering in section 4.1. Thus, we relate this effect to the structural change of the surface water layer, which is apparently very different from bulk water.

Finally both SANS and SAXS data for the sample with smallest pores suggest a water density maximum at about 240 K (Figure 4.17). A lowering of about 40 K for the temperature of maximum density (TMD) for water in confinement has been reported from computer simulations [Kumar, 2005, Gallo & Rovere, 2007]. A lowering of TMD for confined water has also been observed experimentally [Zhang, 2009, Taschin, 2010]. For the larger pore sizes in our work, however, any indication of a density maximum is missing. We think that our upper experimental limit of 280 K may be too low in order to distinctly assign this phenomenon. Whether this effect scales with the ratio of surface water, or whether it also depends on the pore size remains unclear. A detailed study of the density maximum goes however beyond the scope of the work presented here.

4.3 Temperature-induced strain effects on the mesopore lattice

This chapter contains the analysis of temperature-induced pore lattice deformation of water-filled MCM-41 materials. For this purpose, further analysis of the SAXS data from section 4.2 was performed. In the previous section, the changes of the Bragg peak intensity with temperature were discussed. This section now analyses the development of the Bragg peak positions, which were observed during the same measurements. Hereby, the analysis of SAXS data from six different MCM-41 samples with pore sizes ranging between 2.0 nm and 4.4 nm was performed. The obtained results are discussed and set into the context with those previously reported from measurements on similar systems. A new explanation for their occurrence is proposed.

4.3.1 Pore lattice strain from Bragg peak shifts

The previous chapter already introduced some characteristic changes of the SAXS scattering patterns with temperature measured for water-filled MCM-41 samples. Particularly, the Bragg peaks originating from ordered mesopore structure show clear changes with temperature. As previously shown, the change of their intensity is understood by the change of core water density upon cooling and heating. Particularly at phase transition points, this change is strongly pronounced due to the density change between the solid and the liquid phases. Analysing the scattering data in detail shows that intensity is not the only changing parameter of the Bragg peaks. The positions of the different Bragg peaks also show some characteristic changes upon cooling and heating. In order to visualise the observed effect, the scattering patterns measured for MCM44 sample at three different temperature points are shown in Figure 4.18 for the region of the (10) Bragg peak. The observed peak shift seems to be not uniform (see the shift between the red and the blue curves in Figure 4.18). Note, that the position of a Bragg peak is determined by the lattice parameter of the hexagonally-ordered mesopore lattice. Thus, the observed effect can be related to the change of the pore lattice parameter with temperature.

In order to analyse this effect in more detail, the pore lattice parameter d was calculated using Equation 2.39. Hereby, the position q_{hk} of the particular (hk) Bragg peak was determined by two different approaches. The first approach includes a fit of the (10) Bragg peak intensity by a Gaussian curve and a constant background (first-order polynomial). Figure 4.19 exemplary shows a fit of the scattering intensity in the region of the Bragg peak of MCM44. The fit results for the *centre position of the Gaussian curve* were then used for the calculation of the lattice parameter at a particular temperature.

The second approach defines the value for q_{hk} by the *centre of mass* of the Bragg

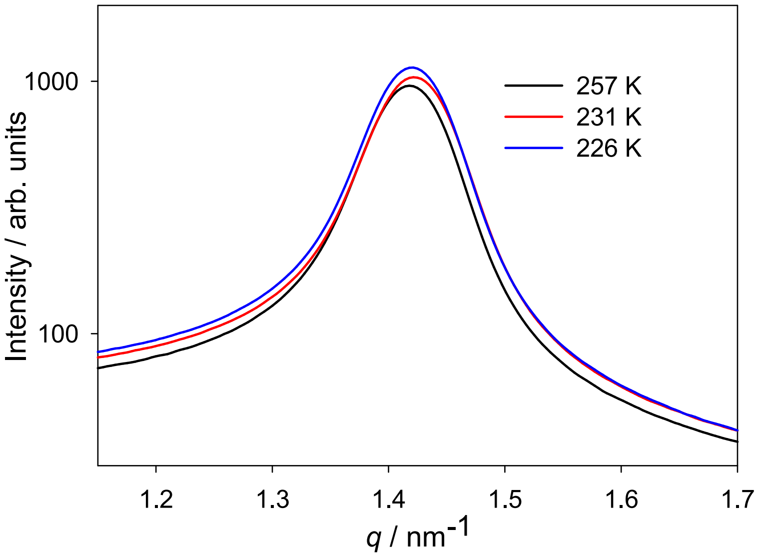

Figure 4.18: Scattering pattern of MCM44 material shown for three temperature points of interest (see Figure 4.22).

peak, calculated by:

$$q_{hk} = \frac{\int qI(q)dq}{\int I(q)dq} \tag{4.5}$$

The detailed procedure of calculation of q_{hk} by Equation 4.5 was performed in the following way [Prass, 2011] (see also Figure 4.20):

- first the position of maximal intensity I_{Max} was determined approximately
- the limits of integration in Equation 4.5 were set by taking an interval Δ, defined by the 3.5-fold of the half-width at half maximum (HWHM), to both sides from I_{Max}
- the background was defined using an exponential curve crossing the borders of this interval, and was subtracted from the entire intensity
- for the residual intensity distribution the centre of mass was calculated by a numerical intensity integration according to Equation 4.5

The two different approaches for determining the Bragg peak position provide very similar slope results giving only a slight difference for the obtained strain isosteres (see Figure 4.21). The borders of the different temperature regions are not affected by the choice of these two approaches. The difference for the slope values will be considered by introducing error bars for the particular slope values. The asymmetric shape of the Bragg peak observed in Figure 4.18 is unclear. Contrast effects,

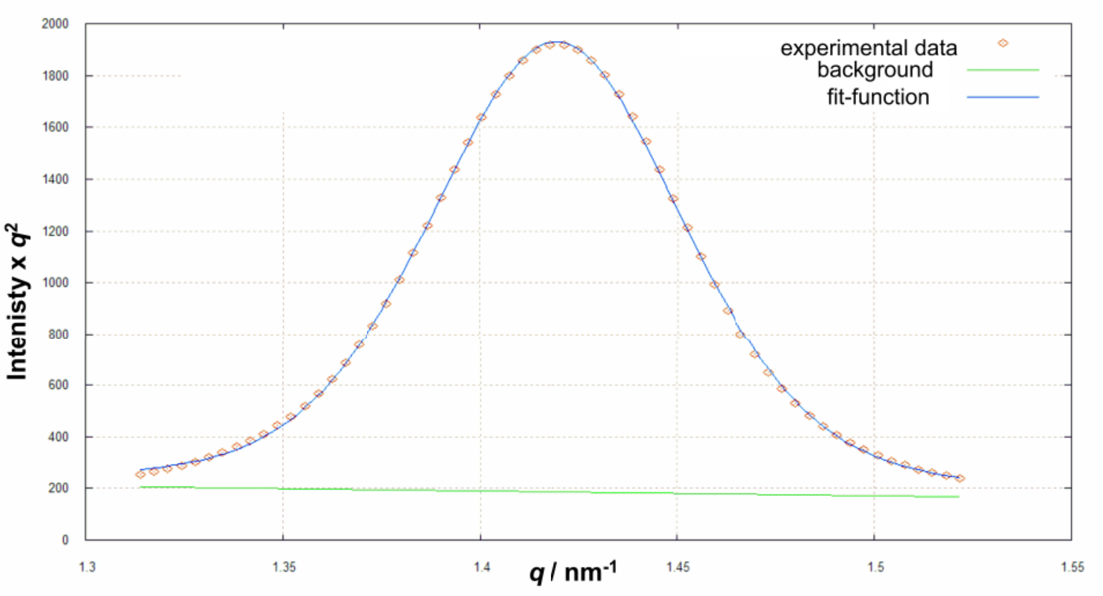

Figure 4.19: Fit of the (10) Bragg peak of MCM44 sample by a Gaussian curve. This approach includes a fit of the scattering intensity (multiplied by q^2) to a Gaussian curve and a background, approximated by a first-order polynomial curve.

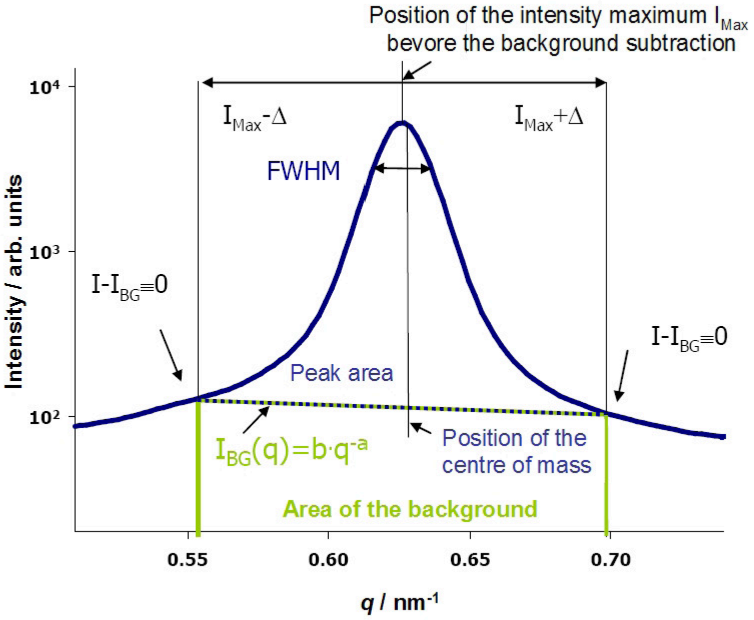

Figure 4.20: Determination of the centre of mass of a Bragg peak. The figure adapted from [Prass, 2011].

which were shown to explain similar observations during liquid-vapour transitions in mesopores [Prass, 2011] can only partly explain the present case. A liquid-vapour transition is characterised by a large change of the pore scattering contrast. In our case this change is expected to be only in the order of 10%, due to the density change of water and ice. Inhomogeneous strains due to lattice imperfections are not considered.

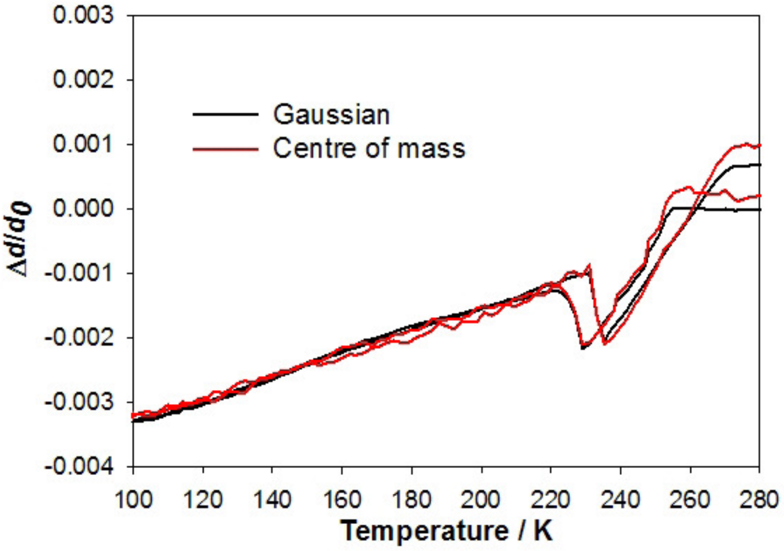

Figure 4.21: Strain isosteres for water-filled MCM34 sample obtained by two different approaches for the determination of the (10) Bragg position. Note that the black curve here is identical to the black curve in Figure 4.27.

Figure 4.22(A) exemplarily shows the temperature development of q_{10} with temperature for the sample MCM44 using the Gaussian fit method. The temperature-induced deformation of the pore lattice can be calculated by introducing the *strain* of the pore lattice:

$$\frac{\Delta d}{d_0} = \frac{d(T) - d_0}{d_0} = \frac{q_0 - q(T)}{q(T)} \tag{4.6}$$

where d_0 is the reference pore lattice parameter, defined by the value at the beginning of a cooling cycle. The diagrams in Figure 4.22 are so-called *isosteres* which visualise a thermodynamic process measured at a constant filling fraction of mesopores [Wallacher, 2005a]. In analogy to the relation between an isotherm introduced in subsection 2.2.4, and a “strain isotherm” defined in [Prass, 2009, Prass, 2011], i.e. a strain curve measured at a constant temperature, the diagram in Figure 4.22(B) is denoted as a “*strain isostere*”.

The temperature-induced pore lattice deformation shown in Figure 4.22(B) clearly

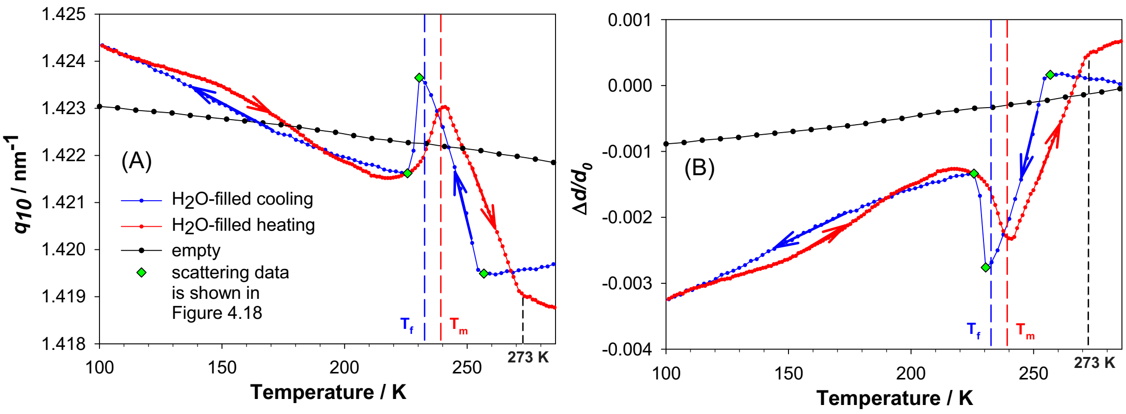

Figure 4.22: (A) Temperature development of the (10) Bragg peak position of MCM44 sample, determined from a fit by a Gaussian curve. (B) Temperature-induced strain of the pore lattice, calculated using Equation 4.6. Cooling and heating cycles of water-filled sample are shown by blue and red curves, respectively. A reference measurement of the empty MCM44 sample is shown as a black curve. The corresponding water freezing and melting temperatures, T_f and T_m from Ref. [Jahnert, 2008b], and from section 4.1 are shown together with the melting temperature for bulk water (273 K). Green diamonds indicate the temperature points for the scattering data shown in Figure 4.18. Noteworthy, a second hysteresis in the temperature region around 160 K -180 K is observed.

depends on the presence of water inside the mesopores of MCM44. The measurement of the empty sample only shows slight contraction upon cooling, and slight expansion upon heating (both curves match each other). This behaviour is understood by the thermal contraction / expansion of the silica matrix explained by $\Delta d/d_0 \propto \alpha \Delta T$, where α is the *linear contraction coefficient* of the silica matrix. The strain values remain below 0.1 % in the entire temperature region.

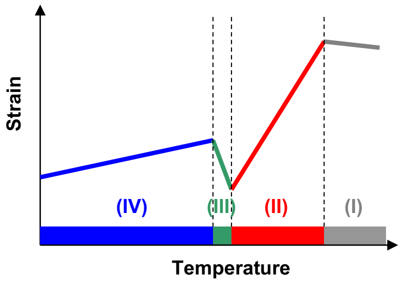

Figure 4.23: Illustration of an idealised strain isostere.

In contrast, for water-filled samples deformation of the pore lattice upon cooling and heating is non monotonous within the studied temperature region. The curves can be described by different “sub-curves”, each showing a roughly linear temperature dependence. In order to analyse these different parts of the strain curves it is helpful to divide the total experimental temperature region into sub-regions. Starting from the highest measured temperature and following the cooling branch of the strain isostere (the blue curve in Figure 4.22(B)) first the pore lattice marginally expands until the temperature of about 260 K is reached. This temperature region is denoted as region (I). Upon further cooling, the pore lattice contracts until a temperature values of slightly below $T_f = 233$ K. This temperature region is denoted as the region (II). Further cooling induces a pronounced expansion within a short temperature range, denoted as the region (III). Finally, for temperatures below $T \approx 225$ K the lattice parameter gradually decreases upon further cooling, this is the region (IV). Similar sub-regions can also be determined for the heating direction. However, the strain curve obtained for the heating cycle is shifted by around 4-5 K to higher temperatures, building a hysteresis between the cooling and the heating directions. Figure 4.23 schematically shows an idealised strain isostere with the corresponding sub-regions. Noteworthy, the dip which sets up the border between the regions (II) and (III), for both temperature directions in Figure 4.22 coincides nearly perfectly with the corresponding phase transition temperatures of water in pores of MCM44 from Ref. [Jahnert, 2008b], and from section 4.1. Another remarkable observation is that the border between the regions (I) and (II) for the heating direction, exactly coincides with the bulk water melting temperature of $T = 273$ K (see the black vertical dashed line in Figure 4.22).

A strain isostere was calculated from the scattering data of all measured Bragg peaks using Equation 2.39 with the corresponding (hk) indices. For the samples with three Bragg peaks within the measured q-region, the change of the lattice parameter with temperature is almost the same. Only slight deviations at very low temperatures (the region (IV)) are observed (see Figure 4.24).

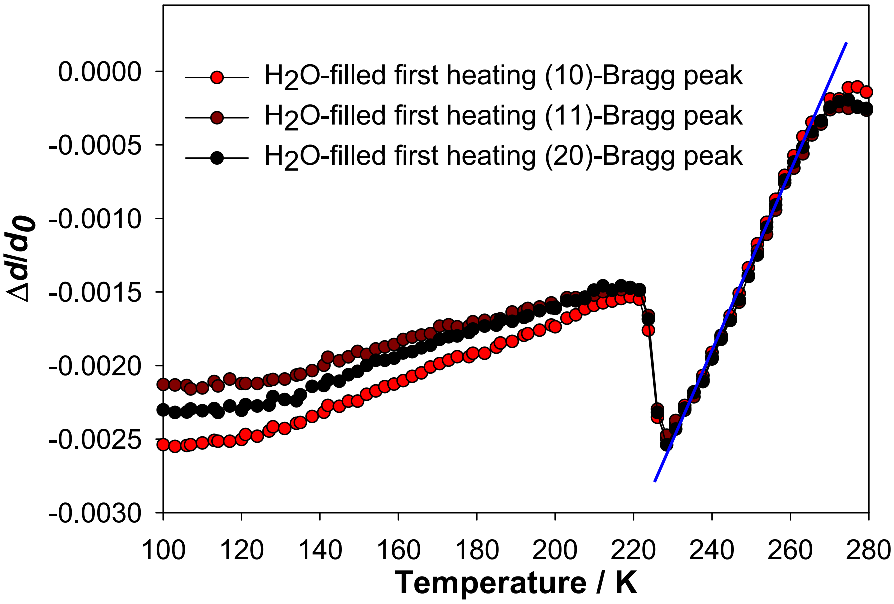

Figure 4.24: Strain isosteres obtained from the analysis of three different Bragg peaks from MCM34 using the Gaussian fit. The blue line indicates the fit of the temperature region (II) by a straight line.

4.3.2 Pore size dependence

In order to understand the observed strain effects in more detail, a systematic analysis of the scattering data for all six MCM-41 samples with different pore sizes was performed. For the sample MCM34 two cooling and two heating cycles were subsequently measured and analysed, in order to check the reproducibility of the effects. The results of the temperature-induced pore lattice deformation for all six samples are shown in Figure 4.25.

For all strain isosteres a similar characteristic temperature behaviour can be observed. Except for MCM25, four temperature sub-regions as defined in Figure 4.23 can be determined. For the different pore sizes similar contraction and expansion effects are observed within the corresponding sub-region. However, the corresponding slope values are different for different samples. All samples show a hysteresis between the cooling and the heating cycles. The two subsequently measured cycles for MCM34 nearly coincide, showing only slight deviations. The further analysis of the data was performed by calculating the slope values for the respective temperature sub-region of the strain isosteres. This slope can be understood as the linear contraction factor of the water-filled pore system. The calculation was performed by fitting a linear curve to the strain isostere within a particular temperature sub-region (e.g. see Figure 4.24 for the fit of the region (II) for MCM34). For the samples MCM30, MCM25 and MCM20, the slope within the entire particular temperature sub-region was difficult to determine. Hereby, only the isostere parts showing approximately linear temperature behaviour were used for the fit analysis. Results obtained for these samples have to be treated with care.

Sample	Empty	Region (II)	Region (III)	Region (IV)
MCM20	4.9	35.7 / 40.7	-9.5 / -7.0	13.4 / 19.4
MCM25	3.4	23.2 / 35.9	-30.1 / -40.2	-
MCM30	3.6	67.9 / 38.8	-108.1 / -105.8	17.7 / 20.5
MCM34 1st	0.7	51.2 / 60.0	-222.7 / -255.7	11.1 / 12.1
MCM34 2nd	0.7	59.3 / 61.7	-215.8 / -283.4	11.7 / 11.7
MCM39	6.0	73.4 / 63.6	-146.6 / -66.3	19.1 / 18.1
MCM44	4.6	116.6 / 93.8	-297.9 / -119.4	15.3 / 19.1

Table 4.1: Slope values of the strain isosteres in units of 10^{-6} K^{-1}, obtained for the samples in the empty state, and in the water-filled state at the different temperature regions. The different temperature directions are indicated as: cooling / heating. The two subsequent temperature cycles for MCM34 are indicated as 1st and 2nd, respectively. The values are determined by fit of the (10) Bragg-peak by a Gaussian curve.

Noteworthy, for samples with the largest pores, i.e. MCM44, MCM39 and MCM34, the border separating the sub-regions (I) and (II) in the heating direction is exactly

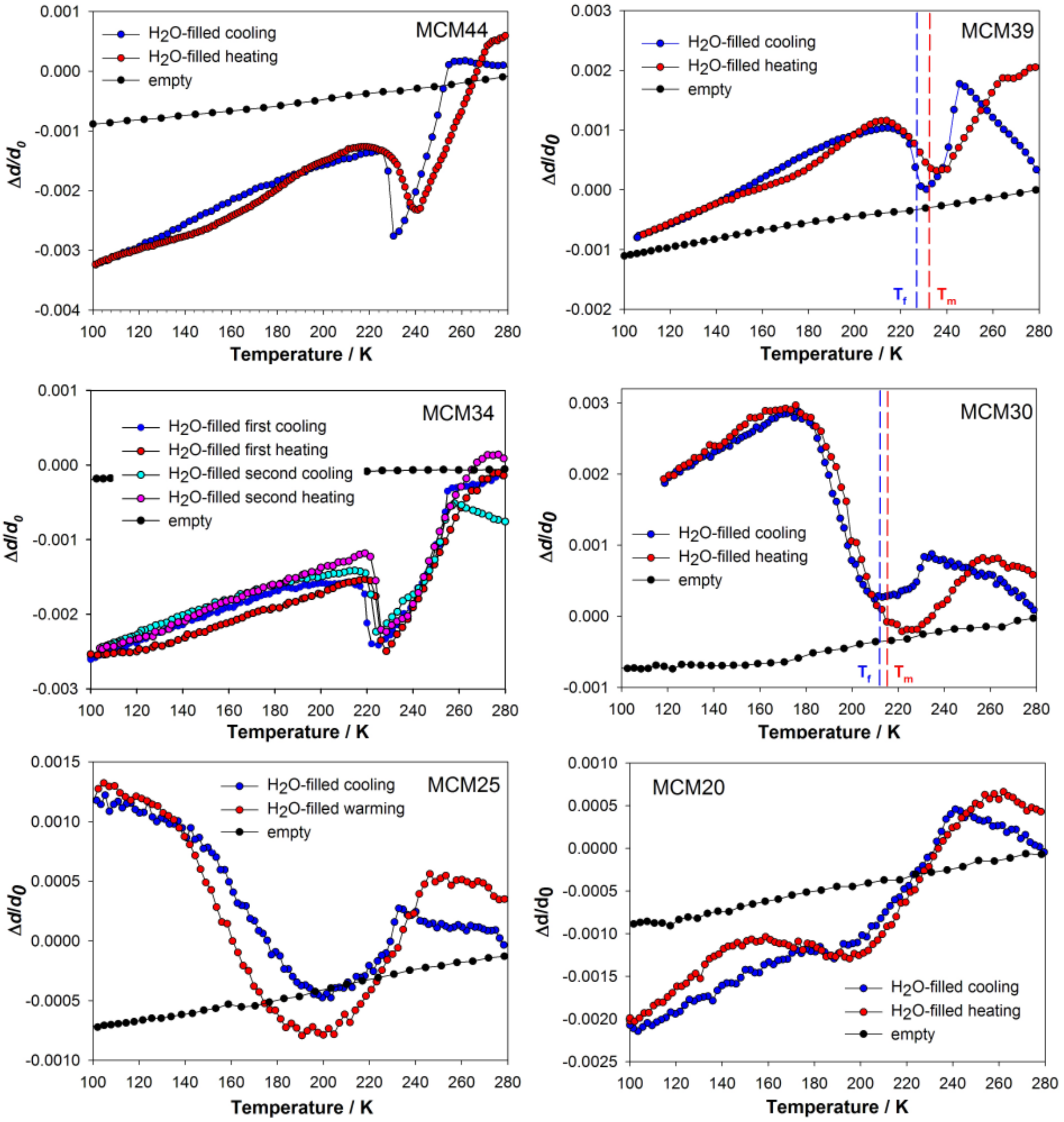

Figure 4.25: Strain isosteres for all measured samples. The calculation of the Bragg peak position was performed using the Gaussian fit method.

at the same temperature of 273 K. For samples with smaller pore sizes the corresponding border is shifted by around 10 K to lower temperatures. However, also for these samples a kink around $T = 273$ K can be observed. This effect seems to indicate melting of bulk water in the system. Therefore different pore filling fractions were investigated in order to understand this phenomenon.

4.3.3 Influence of the pore filling fraction

This sub-section aims at investigating the influence of the pore filling fraction on the shape of a strain isostere. For this purpose an additional experiment with the MCM39 sample at six different pore filling fractions was performed using the same experimental SAXS setup as in the previous sub-section. The filling fractions, chosen for this experiment are shown in Figure 4.26, indicated by red points along the water sorption isotherm of MCM39 measured by an independent gravimetric measurement.

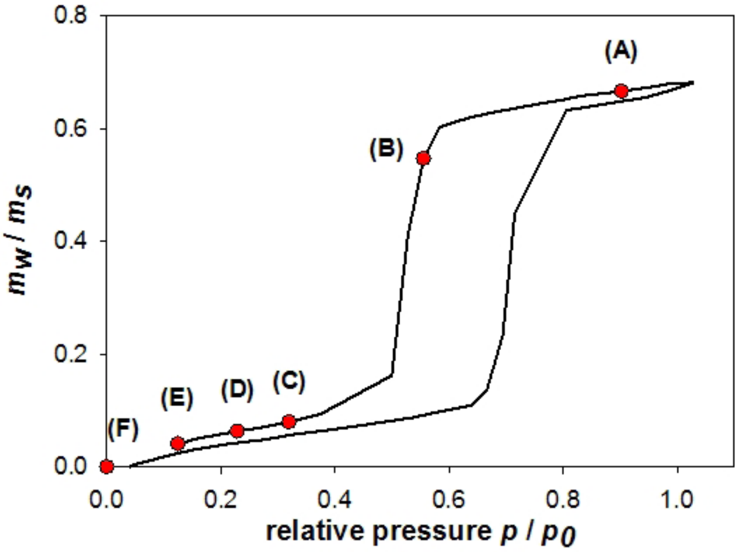

Figure 4.26: Gravimetric water sorption isotherm for the MCM39 sample obtained by an independent measurement using the laboratory micro balance stage [Morak, 2012]. The mass of adsorbed water is indicated as m_w, that of the empty silica sample is m_s. The different filling fractions are indicated by the letters (A-F).

Data collection and analysis was performed in the same manner as for the previous measurements. Strain isosteres which correspond to the different pore filling fractions are shown in Figure 4.27. One can see that the shape of the isosteres strongly depends on the amount of water in pores. Isosteres of the cooling and heating directions are shifted forming a hysteresis. Previously defined temperature regions can be distinguished at least for three measurements with the highest pore filling fractions. Again, the measurement of completely filled sample in heating direction shows a distinct kink exactly at the melting temperature of bulk water. The measurement with the second largest filling fraction (point (B) in Figure 4.26) does not posses a border between the regions (I) and (II), and the slope is much lower than for region (II) measured for the filling fraction (A). This effect is an important point of discussion (see later). In the following, the region above the phase transition temperature for the curve (B) in Figure 4.27 is denoted as region (II). The slope values for the different temperature regions were obtained in the same manner as in the previous sub-section. The results are summarised in Table 4.2.

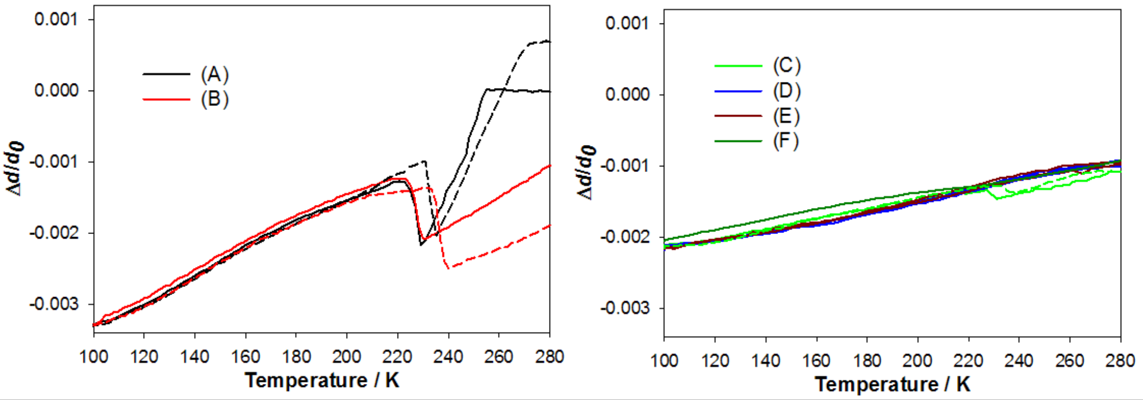

Figure 4.27: Strain isotherms calculated for MCM39 materials with six different water filling fractions. Cooling and heating directions are shown as solid and dashed lines, respectively. The letters in the legend denote the different filling fractions of the pores as shown on the gravimetric isotherm in Figure 4.26. The difference between the cooling and heating directions for (A), (B), and (C) are clearly marked by hystereses.

Filling fraction	Region (II)	Region (III)	Region (IV)
(A)	74.9 / 77.9	-242.2 / -180.8	17.2 / 18.6
(B)	20.1 / 15.5	-227.8 / -249.8	20.4 / 18.9
(C)	8.0 / 8.0	-30.6 / -33.0	6.7 / 6.7

Table 4.2: Water filling fraction analysis for MCM39 material. Slope values for the different temperature regions of the strain isosteres are in units of 10^{-6} K^{-1}. The different temperature directions are indicated as: cooling / heating. The values are determined using the fit of the (10) Bragg peak intensity by a Gaussian curve. The slope value for the three lowest filling fractions (points D, E, F in Figure 4.26) is constant for the entire temperature region, and corresponds to $6.7 \cdot 10^{-6}$ K^{-1}.

Results for the regions (II) and (IV) obtained for the complete filled sample (A) are very similar to those from the previous experiment (see Table 4.1). However, the slope of the region (III) seems to be rather different. The slope values for the second highest filling fraction (B) are very similar in the regions (I) and (IV). The slope for (B) in region (III) is similar to the completely filled sample (A). The samples with lower filling fractions show only the linear contraction coefficient of the silica matrix. Only for the filling fraction (C) a weak evidence of the region (III) can be observed.

4.3.4 Discussion

Pore lattice strain in different temperature sub-regions

The present measurements of pore lattice deformation upon cooling and heating can be divided into (at least) four different temperature regions. Each of these regions is characterised by a different dependence of the strain on temperature.

Beginning with the first sub-region, the region (I), the system is characterised by a pore filling fraction slightly below the complete filling. The different slope values for different samples, and also for different temperature directions do not show any systematic trend. This region is probably strongly affected by the fact that the pore system is open and can exchange water molecules with the environment. Lowering the temperature from the starting point may lead to further adsorption of water molecules from the vapour phase into the pores, or even on the grain surface, leading to the occurrence of bulk water in the system. Also the expansion of pore water upon cooling may lead to the water outflow from the open pores, and to the crystallisation of bulk ice outside the pores. The kink, marking the border between the regions (I) and (II), strongly indicates freezing and melting of bulk water (see Figure 4.25). The presence of bulk ice strongly influences the further shape of the strain isosteres.

The temperature behaviour in the region (II) is an important point of discussion. It is characterised by the liquid pore water being in contact with the bulk ice surrounding the pores. This region will be discussed later.

Regarding the results from independent DSC [Jahnert, 2008b] and Raman (section 4.1) measurements, the region (III) can be attributed to the temperature region of the core water phase transition. The temperature region (III) becomes strongly smeared with decreasing pore size. This trend is parallel to the previously discussed magnitude of the Raman signal shift, or the change in core water density upon phase transition. An important result is that the pore lattice of MCM25 and MCM20, in which no first-order phase transition for core water exists, shows also distinct deformation with temperature. This appears to be very important within the context of the previously discussed phenomena (see section 4.1 and section 4.2).

The gradual structural change of core water from the liquid phase at room temperature to the amorphous LDA phase at low temperatures for pores with diameters < 2.5 nm can apparently be detected by a mechanical deformation of the pore walls. It is noteworthy that for the MCM20 sample, where a water density minimum is supposed to be situated in the temperature region around 160 K - 180 K, the pore lattice deformation region (III) is observed at the same temperature. This may indicate a possible structural change of surface water within the 2.0 nm small pores. This may also explain a second hysteresis between the cooling and heating cycles observed for MCM44 and for MCM39 in Figure 4.25. While the core water phase transition is strongly dependent on the pore size, the transformation of the surface water seems to take place around 160 K - 180 K, being independent on the pore size. For other samples this effect can not be resolved, due to partially overlapping core water transition in this region.

The temperature region (IV) shows a characteristic slope as long as the mesopores are at least partially filled with water (points (A) and (B) in Figure 4.26). This contraction upon cooling can be related to the contraction of frozen pore water upon further cooling.

The effect of partial pore filling

Another important observation is that the shape of an isostere strongly depends on the filling fraction of the pores. For the partially filled sample (point (B) in Figure 4.26) similar slope values are observed for the regions (IV) and (II), while the region (I) is completely missing for this sample. This shows that the border between the regions (I) and (II) only exists if the mesopores are completely filled with water. The kink at 273 K, which is observed in the strain isosteres for the heating directions strongly indicates the presence of bulk water in the system. Since the filling process of mesopores was performed from the vapour phase below the saturation pressure of bulk water, we do not expect large amount of bulk water outside the pores. However, already a thin bulk water film covering the porous silica grains which melts at 273 K can explain the kink at this temperature. The origin of this film may be explained by previously discussed adsorption of the surrounding vapour with decreasing temperature. Our previous SAXS data analysis in section 4.2 indicates a decrease of pore water density upon cooling. Hence, the outflow of pore water on the surface of the grains would consistently explain the presence of bulk water being in direct contact with the pore water. Though, wherever this excess bulk water comes from, the slope of the isosteres in the region (II) strongly depends on its presence. This is a very important observation for the explanation of the origin of this peculiar behaviour of the pore matrix in the temperature region (II). It seems to be contradictory that mesopores filled with liquid water contract upon cooling, since the water itself expands. This phenomenon deserves a more detailed discussion, which will be performed in the following paragraphs.

For filling fractions below some “critical value” (points (C), (D), (E), and (F) in

Figure 4.26), the temperature-induced pore lattice deformation in the region (IV) coincides with that of the empty sample (see Figure 4.27). The detailed study of this “critical value”, however, demands further detailed measurements with more filling fraction points on the desorption branch of a sorption isotherm.

Literature background

Temperature-induced length changes of porous silica glass-water systems were already observed several decades ago, and reported in Refs. [Hodgson & Mcintosh, 1960, Litvan & Mcintosh, 1963, Antoniou, 1964, Litvan, 1966, Feldman, 1970]. These studies essentially aimed at studying the freezing and melting point depression of different liquids in nano-confinement. The experiments were performed by measuring the macroscopic length changes of water-filled monolithic porous silica glass (Vycor) by means of dilatometry. Interestingly, the temperature dependence of macroscopic length changes of the monolithic silica glass roughly corresponds to those observed within this thesis. Similar to our case, these references report different shapes of the strain isosteres obtained for different pore filling fractions. The strain behaviour at very low temperatures (region (IV)) was explained in terms of contraction of frozen adsorbate upon cooling. Particularly for water, the observed contractions and expansions at higher temperatures were connected to the anomalous water density behaviour with temperature. The region (III) was connected with the anomalous density change of water upon freezing. Expansion of water during freezing in region (III) was regarded to give the most plausible explanation for the observations. However, similar isosteres were also reported from independent measurements of benzene [Hodgson & Mcintosh, 1960] and xenon [Litvan & Mcintosh, 1963]. These fluids are characterised by a normal density behaviour at the liquid-solid phase transition, i.e. their density increases upon freezing. Although additional calorimetric measurements could assign the region (III) to the temperature of fluid solidification in pores, the authors could not give a plausible explanation for the observed strain effects of the pore matrix. The apparent contradictions in their arguments were referred to the necessity of further investigations of the system. Also the strain effects in the temperature region (II) remained unclear. Since liquid water expands upon freezing, no coherent picture for the observed contraction in the region (II) of the water-filled silica glass could be found. The observed contraction of the silica matrix upon cooling in region (II) was referred to the large pore size distribution in the Vycor glass. In this region “contraction is considered to be due to removal of water from the pores after ice has formed in larger pores” [Feldman, 1970]. The main conclusions of these publications presumed the applicability of capillary condensation theory to the fluid solidification in nano-pores. Hereby, the lowering of freezing and melting temperatures in confinement was explained by introducing a hemispherical meniscus for the liquid-solid interface [Litvan & Mcintosh, 1963].

To our knowledge, the next experimental study reporting similar temperature-induced strain effects on fluid-filled mesoporous silica was reported in 2000 by Faivre *et al.* [Faivre, 2000]. *In situ* measurements of dodecane confined in p^+ type porous silicon layers were performed by means of X-ray diffraction. As their confining matrix was a perfect crystal, the Bragg peak analysis could be performed measuring the change of the lattice parameter of silicon with temperature. The reported strain isosteres, again, qualitatively correspond to those observed in the present study. Dodecane is a fluid characterised by a normal density behaviour with temperature. Based on Feldman's arguments Faivre *et al.* explained their observations for the region (II) by the formation of concave liquid-vapour menisci in partially-filled pores, where the fluid was removed by the freezing process in larger pores. The negative Laplace pressure is therefore regarded to induce contraction of the porous silicon matrix in the region (II). When all pore fluid is frozen the liquid menisci disappear and the capillary stress vanishes, leading to a relaxation of the pore lattice within the region (III) [Faivre, 2000].

Model for freezing and melting in confinement

In contrast to the Vycor glass in Feldman's studies, or the porous silicon in Faivre's studies, our mesoporous systems are characterised by a very narrow pore size distribution (see [Jahnert, 2008a]). For water confined in MCM-41 materials with pore diameters larger than 2.5 nm the temperature regions where core water freezes and melts are very narrow. Taking for instance the DSC peak widths (FWHM) from Ref. [Jahnert, 2008b], and the temperature region of the spectral Raman shifts from the section 4.1, for MCM44 and MCM39 the corresponding temperature regions are around 5 K. Therefore, at least in these materials, we do not expect gradual freezing of water due to different pore sizes. Thus, Feldman's explanation for the pore lattice deformation within the region (II) can not be applied to our system. From previous experimental and theoretical studies [Scherer, 1992, Dolino, 1996, Guenther, 2008, Biener, 2009, Prass, 2009, Schoen, 2010, Gor & Neimark, 2010] it is known that filling of mesoporous materials with liquids is accompanied by sorption-induced deformation of the mesoporous materials. This deformation is understood by the negative Laplace pressure acting at capillary condensation and evaporation. Some of these previous studies were performed in the same ordered mesopores of MCM-41 materials by means of SAXS. The similarity in the shape of the strain isotherms in Ref. [Prass, 2009] and that of the strain isosteres presented in this thesis is striking. A strain isotherm implies a plot of $\Delta d/d_0$ versus $ln(p/p_0)$, a strain isostere shows $\Delta d/d_0$ versus T. This difference strongly reminds one on that between the Kelvin equation (Equation 2.13) and the Gibbs-Thomson equation (Equation 2.22). Note that the Kelvin equation was derived from the description of the Laplace pressure of a curved liquid. Thus, the Kelvin equation directly contains the Laplace pressure by $2\sigma_{lv}/R$, where σ_{lv} is the surface tension of the liquid, or in other words the liquid-vapour specific interfacial energy. The Gibbs-Thomson equation also includes a similar term, however, the corresponding specific interface energy is that for the liquid-solid interface. According to Everett's argument [Everett, 1961], both equations can be derived by calculating the reduced pressure of a pore liquid characterised by a concave hemispherical interface. The kind of interface between the liquid and the second phase is determined by their specific interfacial energy. Many authors claim that the phase transition of pore water in equilibrium with the bulk phase takes place by penetration of the bulk phase into the pores [Brun, 1977, Enustun, 1978, Handa, 1992]. Thus, pore water melting can be described in the same manner as the capillary condensation [Beurroies, 2004], i.e. the nucleation of a liquid droplet out of the solid phase, which is in contact with the wetting surface layer, and its growth until reaching the pore end. In this picture, freezing of pore water then corresponds to water evaporation from the pores (see Figure 4.28).

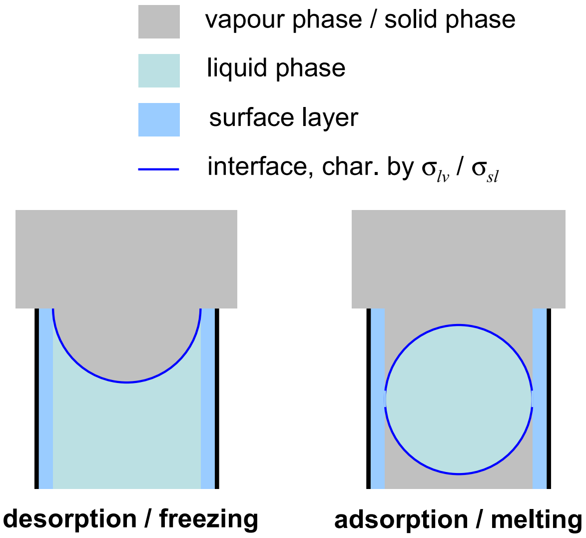

Figure 4.28: Similarity between water phase transitions in mesopores.

Consequently, $\Pi = 2\sigma/R$ can be regarded as a "generalised form of the Laplace pressure" [Everett, 1961], with σ being the specific interface energy (with $\sigma = \sigma_{lv}$ for the liquid-vapour transition, and $\sigma = \sigma_{sl}$ for the solid-liquid transition, respectively).

Similar to the mechanisms of filling and emptying [Prass, 2009], the lattice strain observed in the temperature region (II) can be explained by flattering of the menisci of the liquid-solid interface within the pores (see also Figure 2.13). The ratio between the Laplace pressure and the strain within the plane perpendicular to the cylindrical pores is given by the *effective "pore-load" elastic modulus* M_{PL}:

$$M_{PL} = \frac{\Pi}{\Delta d/d_0}. \tag{4.7}$$

Applying the Gibbs-Thomson equation (Equation 2.22) for the temperature region

(II) one has to replace $\Delta T_m = T_0 - T_m$ by $\Delta T = T_0 - T$. Combining Equation 4.7 with Equation 2.22 gives:

$$\frac{\Delta d}{d_0} = \Delta T \cdot \frac{\Delta H^M}{V^M T_0} \cdot \frac{1}{M_{PL}} \tag{4.8}$$

This equation implies that in the region where the pore liquid is in contact with bulk ice, the strain of the pore lattice scales linear with temperature. Consequently, the constant of proportionality in Equation 4.8 gives the slope of the strain isosteres in the temperature region (II). From the slope values of the isosteres in this region we are able to calculate the corresponding values for the effective pore-load modulus M_{PL}, characterising mechanical properties of the porous material. Additionally, the thermal expansion of the empty silica matrix has to be taken into account. It is rather difficult to estimate the actual influence of the silica matrix on the observed contraction and expansion effects of the water-filled samples. In a first assumption these two effects are treated separately, and the correction is performed by subtracting the slope value of the empty sample from the corresponding water-filled sample in the region (II). The results for M_{PL} for three different samples and temperature directions are summarised in Table 4.3.

Sample	slope region (II)	slope error	M_{PL} / GPa	Error(M_{PL})
MCM34	67.9 / 61.3	12 / 6	18.0 / 19.9	3 / 2
MCM39	74.6 / 73.1	2 / 6	16.4 / 16.7	0.4 / 2
MCM44	105.2 / 84.1	7 / 5	11.6 / 14.5	0.8 / 0.9

Table 4.3: Average slope values for the three samples with largest pore sizes in the temperature region (II) in units of 10^{-6} K^{-1}. The values are corrected by the slope of the empty measurement. The different temperature directions are indicated as: cooling / heating. The values for the samples MCM34 and MCM39 correspond to the average values from the two subsequent temperature cycles. The error corresponds to the standard deviation for the two different approaches of the Bragg peak position analysis. The calculation of the effective pore-load modulus values M_{PL} was performed using Equation 4.8.

The values for M_{PL} for the materials MCM34, MCM39 and MCM44 were also independently determined from the analysis of the desorption of pentane from the mesopores of the same materials [Prass, 2009] (see Table 4.4). Comparing the values for M_{PL} for the three samples with the largest pore sizes gives a similar trend between the values in Table 4.3, and those from Ref. [Prass, 2009] in Table 4.4. Since this quantity characterises mechanical properties of the silica materials, one does not expect strong influence of the used fluid. A possible explanation for the quantitative deviations should, however, be attributed to the different fluids used for their calculation.

Sample	M_{PL} / GPa
MCM34	15.8
MCM39	13.9
MCM44	11.2

Table 4.4: Values for M_{PL} taken from [Prass, 2009]

Distinct deviations of this quantity obtained from measurements with different fluids are also reported in Ref. [Prass, 2011]. This is not completely understood, since the determination of M_{PL} does not include the knowledge of the specific interface energies of the involved phases. The only used constants are the molar volume of the fluid V^M, the molar melting enthalpy ΔH^M, and the absolute temperature T. One should keep in mind that the application of Gibbs-Thomson equation (and also the Kelvin-equation) on real experimental systems has to be done with care. As shown in the basics part in section 2.2, these equations are based on a number of various assumptions. Strictly speaking, these equations are valid only for systems characterised by a "perfect wetting liquid", or by the vapour phase being an "ideal gas". The wetting behaviour of water on the silica surface was shown to change upon subsequent adsorption and desorption cycles (see section 4.4). Another question is to which extent the water vapour can be regarded as an ideal gas.

4.3.5 Conclusions

Using SAXS, we could measure temperature-induced mesopore lattice deformation on the nanometer-scale. Similar to previously reported macroscopic measurements on fluid-filled disordered porous systems, our study shows the presence of pore lattice strain during the cooling and heating of water-filled pores. This process is described in terms of formation of liquid-solid menisci in mesopores influenced by the presence of the bulk phase. The present data analysis allows an alternative determination of the effective pore-load elastic modulus for the used mesoporous materials.

An additional aspect of the present study concerns the current discussion about water phase transitions in nano-confinement. Pore lattice deformation is observed in all studied samples, even in those where no first-order phase transition for core water in the middle of the pores was found by other methods. A gradual expansion of the mesopore lattice for materials with diameters smaller than 2.5 nm, together with a second hysteresis for materials with larger pores were observed in the temperature region around 160 K - 180 K. This finding strongly supports previously suggested structural change of the surface water layer taking place at these temperatures.

4.4 Repeated water sorption in SBA-15

The effect of repeated cycles of water adsorption/desorption on the structural stability of ordered mesoporous silica SBA-15 was studied by small-angle X-ray scattering (SAXS). This chapter shows results from *in situ* sorption measurements which were conducted using a custom-built sorption apparatus in connection with a laboratory SAXS setup (COSCAD's).

4.4.1 Integrated SAXS intensity

SAXS data were measured as a function of relative water vapour pressure p/p_0, p_0 denoting the bulk water vapour pressure at the given temperature. Figure 4.29(A) shows selected scattering profiles for the sample at $p/p_0 = 0$; it is obvious from these data that the intensity levels clearly differ between the first and the fourth cycles. Although the relative height of the Bragg peaks appears to be similar for the first four cycles, the absolute value of the intensity decreases progressively from one cycle to the next. Ageing of the sample as described in subsection 3.3.2 seems to also affect the structural order of the pore lattice, since only the three leading Bragg reflections appear for the aged sample, higher order reflection no longer being visible.

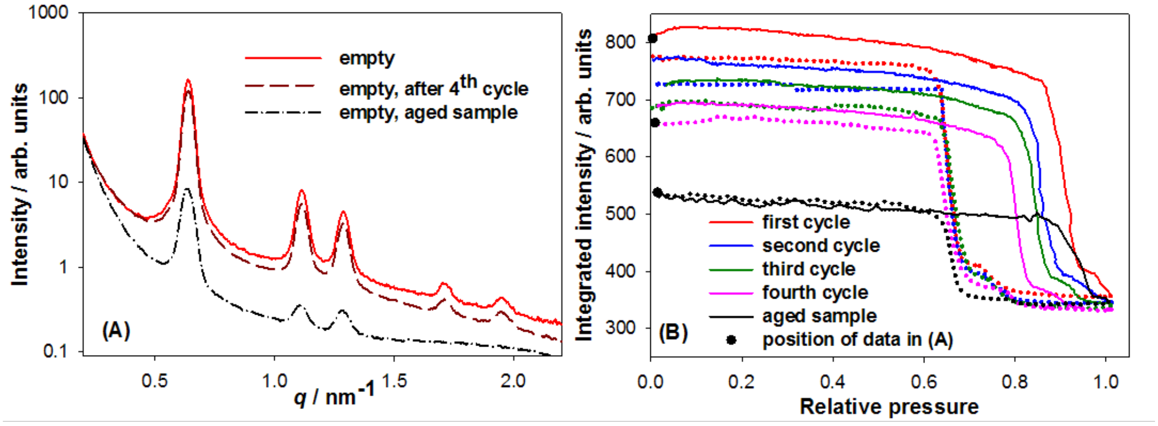

Figure 4.29: (A) SAXS patterns of the evacuated SBA-15 sample measured before the first cycle (solid), after the fourth cycle (dashed), and of the aged sample in the empty state (dashed–dotted). (B) Integrated scattering intensity for the first four sorption cycles and for the aged sample (solid/dotted lines for adsorption/desorption, respectively). The aged sample data were normalised to the previous ones at $p/p_0 \sim 1$. The black points indicate the data points shown in (A). Figure taken from [Erko, 2012b].

The integrated scattering intensity $\bar{Q}$ was calculated from the experimentally measured X-ray scattering intensity $I_s(q)$ by Equation 2.44, after subtraction of a constant background determined by applying Porod's law (Equation 2.42) as described in subsection 2.4.4. Equation 2.42 requires an extrapolation of the measured scattering intensity to low and high scattering vectors. In this work, the contribution from low scattering vectors $q < q_{min}$ was assumed by a constant scattering intensity $I_{min} = I(q_{min})$, where $q_{min}(= 0.1\ \mathrm{nm}^{-1})$ is the lower limit of the experimental q-range. The contribution from high scattering vectors $q > q_{max}$, with $q_{max} = 2.2\,\mathrm{nm}^{-1}$ was determined by extrapolation of the experimental data on the basis of Porod's law. Altogether, $\bar{Q}$ was determined using Equation 2.48 (see also Figure 2.27).

Figure 4.29(B) shows the integrated intensity as a function of relative vapour pressure for the first four sorption cycles together with those of the aged sample. To account for the changed amount of sample in the beam for this latter case, the corresponding data for the aged sample had to be normalised to the average value from the first four sorption cycles at $p/p_0 \sim 1$. Distinct changes of the integrated intensity with pressure are observed for all five sorption cycles.

For the first adsorption an increase of the integrated intensity with pressure is observed up to a relative pressure of ~ 0.1. This effect, which is observed only for the first adsorption, was found previously for other fluids in SBA-15 and is attributed to the filling of the micropores within the mesopore walls, thereby increasing the scattering contrast between the silica walls and the mesopores [Zickler, 2006, Muter, 2009, Jahnert, 2009]. A steep drop in intensity at $p/p_0 \sim 0.9$ characterises the capillary condensation process. The intensity value reached at saturation pressure remains constant at first during the desorption process followed by a steep increase in intensity at relative pressure $p/p_0 \sim 0.7$. However, the intensity does not reach the value of the preceding adsorption, not even at $p/p_0 = 0$ after evacuation for 3 h. In the subsequent adsorption process, the integrated intensity initially stays constant at the plateau of the previous desorption and falls off steeply at $p/p_0 \sim 0.85$. Hence the pore condensation pressure in the second adsorption is clearly lower than in the first adsorption. The second desorption process follows the trace of the first desorption, but again a reduced intensity level is reached at $p/p_0 = 0$. This trend of a reduced pressure value for the intensity drop for adsorption and the reduced intensity step for desorption also persists for the subsequent sorption cycles. The pressure value for the intensity step measured during the fourth desorption seems to deviate slightly from the previous ones. It should be noted that the equilibration time during the first three sorption processes was similar, and in the same order as in our previous volumetric water isotherm where equilibrium was reached [Erko, 2008, Erko, 2010]. For the fourth sorption process the filling and emptying of pores was performed almost twice as fast as in the previous ones. This may explain the slight shift in the pressure value for the fourth desorption branch. The corresponding adsorption branch, however, seems to follow the trend of the previous adsorptions, i.e. the integral intensity drops at a reduced pressure value compared to the previous adsorption, even taking into account the pressure shift of the corresponding desorption branch.

4.4.2 Filling isotherm from integrated intensities

Generally, the change of the integrated scattering intensity (Figure 4.29(B)) observed in the course of the sorption process is connected with the pore filling process which changes the scattering contrast between the pore content and the silica matrix. As outlined in more detail in Ref. [Findenegg, 2010], the present system can be regarded as a three-phase system made up of solid (S), fluid (F) and empty space/vapour (V), with X-ray scattering length densities (sld) ρ_S, ρ_F and ρ_V, respectively. The integrated intensity as defined by Equation 2.44 for a three-phase system is given by Equation 2.47. In our case it can be expressed by (note that $\rho_V = 0$):

$$\bar{Q}(\varphi_F) = K[\rho_S^2\varphi_S(1-\varphi_S) + \rho_F^2\varphi_F(1-\varphi_F) - 2\rho_S\rho_F\varphi_S\varphi_F], \tag{4.9}$$

where φ_S and φ_F are the volume fractions of solid matrix and fluid sorbate, respectively, and K is a numerical factor. Solving Equation 4.9 for the experimental data set of $\bar{Q}(p/p_0)$, the results can be expressed by the pore filling fraction $f(p/p_0) = \varphi_F/(1-\varphi_S)$. Taking into account the previously discussed effect of micropore filling at $p/p_0 < 0.1$ during the first adsorption process, the data of the first adsorption isotherm were shifted by setting $f(p/p_0) = 0$ at $p/p_0 = 0.1$, i.e. for the point with the maximal value of the integrated intensity on the first adsorption branch. The calculated filling isotherms are shown in Figure 4.30.

The isotherms of the first four sorption cycles are characterised by a systematic change of two parameters. Since the value of the integrated intensity at $p/p_0 \sim 0$ decreases from one to the next desorption process (Figure 4.29(B)), the calculated pore filling fraction at $p/p_0 = 0$ increases accordingly. This suggests an increasing amount of water remaining within the pores after each cycle. The second systematic trend is the shift in the capillary condensation pressure, which shifts to lower p/p_0 values from one to the next cycle.

Since the measurements on the aged sample were made some months later, the resulting intensity data could not be compared on an absolute scale with those of the first four cycles but were normalised to the values at $p/p_0 \sim 1$. This is motivated by the observation that for the first four cycles the same intensity level was reached at the saturation pressure.

After the fourth cycle the sample temperature was raised to 330 K under vacuum conditions and the SAXS pattern was recorded as a function of time. Figure 4.31 shows that this temperature treatment causes an increase in the integrated intensity, but the intensity levels off at about 740 intensity units after 3 h, while the initial value at the beginning of the first adsorption cycle was above 800 intensity units (see Figure 4.29(B)). This indicates that heating to a temperature of more than 50 K above the adsorption/desorption temperature is not sufficient to remove all the water from the pores.

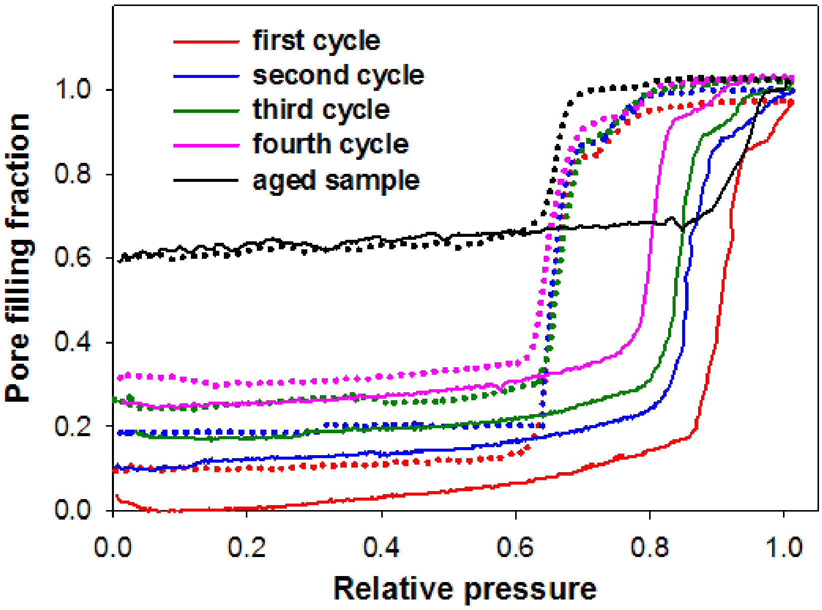

Figure 4.30: Filling isotherms derived from SAXS data by Equation 4.9 for the first four sorption cycles and for the aged sample (solid lines represent adsorption, dotted lines represent desorption). Figure taken from Ref. [Erko, 2012b].

4.4.3 Form factor analysis

In order to learn more about structural changes in the corona of the cylindrical mesopores of SBA-15 the scattering data (see Figure 4.29(A)) were analysed in more detail. Following the data analysis procedure outlined in Ref. [Findenegg, 2010], we split the integrated scattering intensity $\bar{Q}(p/p_0)$ into two parts: Bragg diffraction from the mesopore lattice $\bar{Q}_{Bragg}(p/p_0)$ and diffuse SAXS intensity arising from disordered porosity $\bar{Q}_{Diff}(p/p_0)$. Figure 4.32 shows the evolution of $\bar{Q}_{Bragg}(p/p_0)$ and $\bar{Q}_{Diff}(p/p_0)$ for the sample in its empty (A) and water-filled (B) stages within the subsequent sorption cycles.

For the evacuated sample (Figure 4.32(A)) the integrated Bragg intensity $\bar{Q}_{Bragg}$ decreases systematically from the initial state to the end of the fourth sorption cycle. On the other hand, $\bar{Q}_{Bragg}$ for the completely water-filled pores (Figure 4.32(B)) stays almost constant independent of the number of sorption cycles (note the different scales of Figure 4.32(A) and (B)). This indicates that at $p/p_0 \sim 1$ the amount of water in the pores is nearly independent of the number of sorption cycles, while Figure 4.32(A) suggests that at $p/p_0 = 0$ there is increasingly more water remaining within the pores after each desorption step. The simultaneous decrease of $\bar{Q}_{Bragg}$ for both pore filling states (red triangles in Figure 4.32) suggests a general reduction of structural disorder of the mesoporous silica matrix, perhaps due to “smoothing” of the rough pore walls.

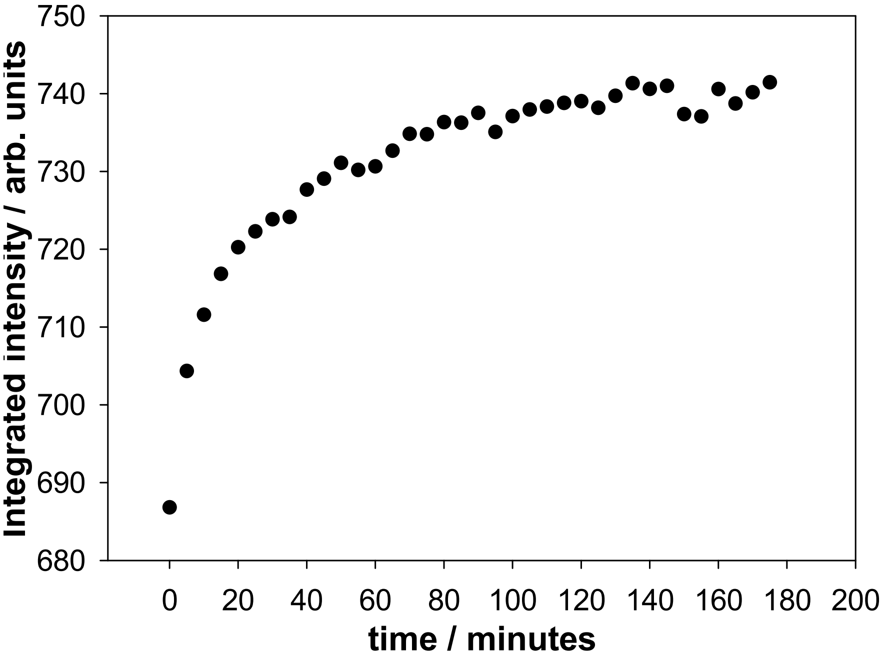

Figure 4.31: Temperature effect on the integrated intensity $\bar{Q}$ of the evacuated sample ($p/p_0 \sim 0$) after the fourth sorption cycle. Heating to 330 K is started at $t = 0$. Figure adapted from [Erko, 2012b].

It is well known that the cylindrical mesopores of SBA-15 have a complex wall structure, which has been modelled by corrugated pore walls and/or a microporous region close to the pore surface [Imperor-Clerc, 2000, Zickler, 2006, Jahnert, 2009]. Therefore, there is a region of lower density in an extended wall region close to the surface, often denoted as a *"microporous corona"*. Changes of the mesopore wall structure, either due to water remaining within the corona or irreversible changes of the thickness and microporosity of the corona itself, will affect the scattering form factor of the mesopores and can therefore be further investigated by a form factor analysis. In a previous study of perfluoropentane sorption in SBA-15 [Zickler, 2006] the form factor was modelled by a four-density step model accounting for the silica matrix, the microporous corona, the adsorbed fluid film and the vapour in the core of the pores. The measured intensity of the Bragg scattering can then be described by Equation 2.32, where the structure factor $S(q)$ has non-vanishing intensity only at the positions of the individual Bragg reflections for a perfect lattice, $F(q)$ is the form factor and K is a constant factor. For a core–shell cylinder consisting of four phases, i.e the silica matrix, the microporous corona, the fluid film, and the vapour is the core of the pores, with the respective scattering length densities ρ_0, ρ_1, ρ_2,

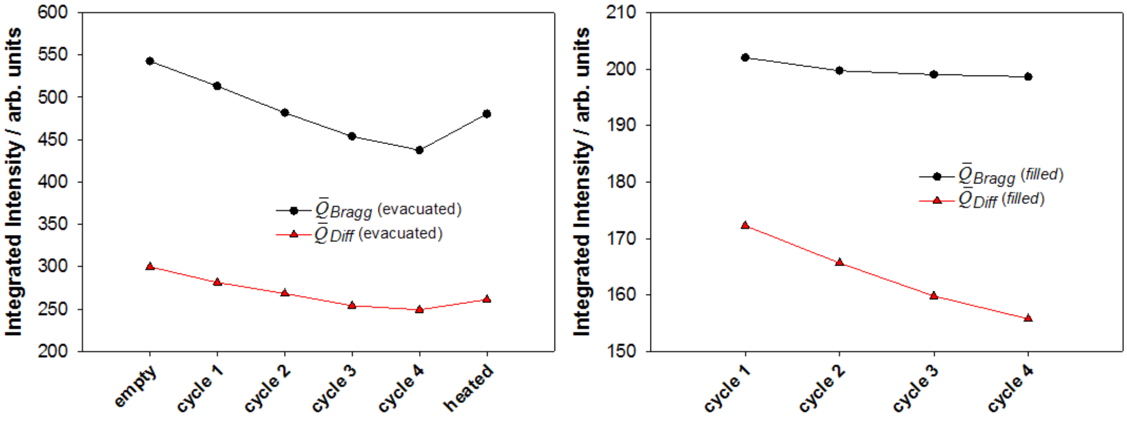

Figure 4.32: Integrated intensities $\bar{Q}_{Bragg}$ (black circles) and $\bar{Q}_{Diff}$ (red triangles) of the evacuated sample (A) and the water-filled sample (B) as a function of number of sorption cycles. Figure adapted from [Erko, 2012b].

and ρ_3 the form factor from Equation 2.30 is given by:

$$F(q) = \frac{(\rho_1 - \rho_0)R_1^2 Z(qR_1) + (\rho_2 - \rho_1)R_2^2 Z(qR_2) + (\rho_3 - \rho_2)R_3^2 Z(qR_3)}{(\rho_1 - \rho_0)R_1^2 + (\rho_2 - \rho_1)R_2^2 + (\rho_3 - \rho_2)R_3^2}, \quad (4.10)$$

the respective radii R_i define the thickness of the microporous corona, $R_1 - R_2$, and that of the fluid film, $R_2 - R_3$. Further, $Z(qR_i) = 2J_1(qR_i)/qR_i$, with $J_1(qR_i)$ being the first-order Bessel function.

In the fit procedure we fit the measured intensities of the five leading Bragg peaks of SBA-15 with Equation 2.32 and Equation 4.10 by minimising the variance. The SAXS data for the annealed empty sample measured before the first sorption cycle provides the values for the parameters K, R_1, $R_2 = R_3$ (empty pores) and ρ_1. The values for ρ_0, and ρ_2 were taken from the NIST data base (see Table 2.3). The subsequent fits were performed for the SAXS intensity measured after each sorption cycle at the nominal relative pressure value of $p/p_0 = 0$, taking ρ_1 and R_3 as the only fitting parameters, while R_1, R_2, ρ_0, ρ_2 and ρ_3 were kept constant. Possible changes of the corona thickness $(R_1 - R_2)$ were also explored as an alternative, but this showed physically unreasonable results. The fits with ρ_1 and R_3 did not show any noticeable changes of R_3 for the different cycles, indicating that no residual water film remains after each desorption process. On the other hand, the corona density ρ_1 distinctly changes from one sorption cycle to the next. The resulting values for the reduced corona density ρ_1/ρ_0 after each sorption cycle are shown in Figure 4.33.

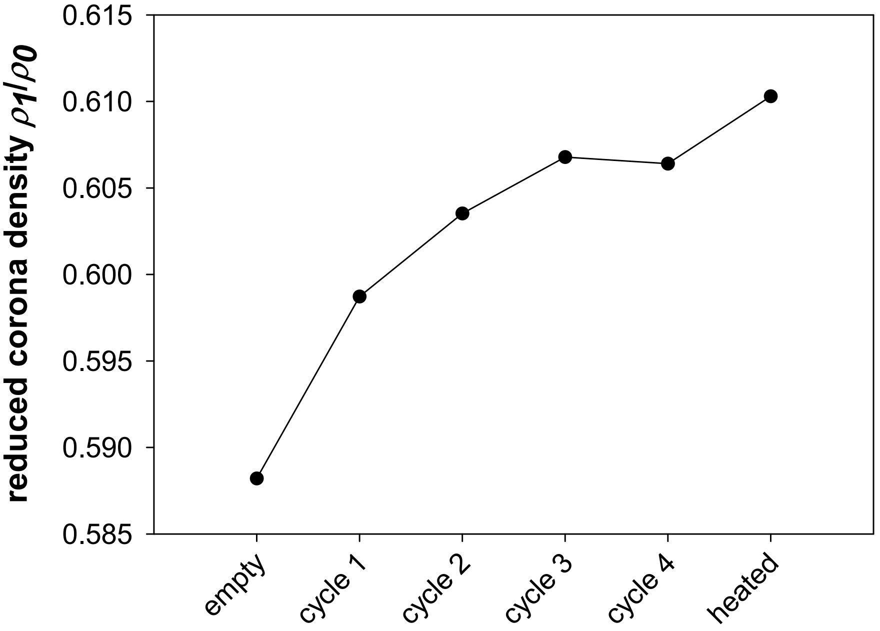

Figure 4.33: Reduced corona density ρ_1/ρ_0 derived from the measurements of the evacuated samples ($p/p_0 \sim 0$) before and after the four sorption cycles and after evacuating at 330 K (heated). Figure taken from [Erko, 2012b].

4.4.4 Discussion and conclusion

A serious point of discussion is related to the argument that not all points of the experimental isotherms may be in full equilibrium. This is always a critical issue when discussing adsorption phenomena in mesoporous materials. The total time necessary for a continuous adsorption/ desorption cycle close to equilibrium was carefully estimated from previous volumetric water sorption in the same material (see Refs. [Erko_2008], [Erko_2010]). An appropriate illustration of the systems' kinetics can be performed in terms of calculating the filling velocity of the sample shown in Figure 4.34. It demonstrates that the system is indeed always close to equilibrium, except for a small pressure regime for adsorption 4, i.e. the fastest adsorption cycle. For cycles 1-3, even in the capillary condensation regime, where kinetics becomes extremely slow, the system is always close to equilibrium.

The present *in situ* SAXS study shows that repeated adsorption and desorption of water in SBA-15 causes two major irreversible changes: first, the pressure at which capillary condensation along the adsorption branch takes place decreases systematically from one to the next cycle. This is clearly not an experimental artefact, since at the same time the capillary evaporation pressure at desorption remains constant for all cycles. The second effect is a systematic decrease of the integrated SAXS intensity at the end-point of the adsorption/desorption cycles, i.e. after a full cycle

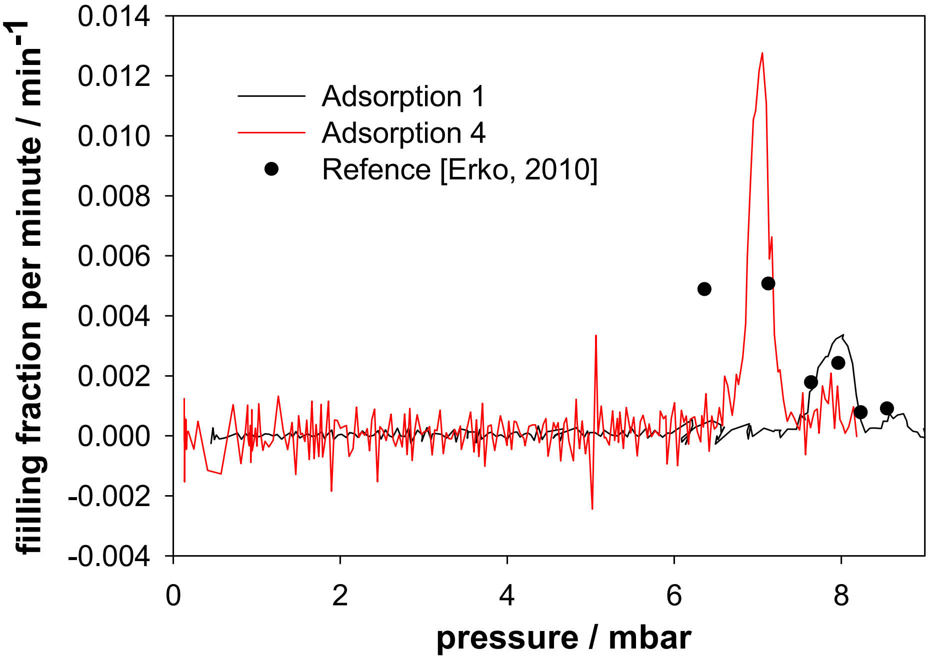

Figure 4.34: Change of the filling fraction with time. For two subsequent SAXS measurement points this quantity is calculated from the change of the integrated SAXS intensity, which corresponds to the change of the sample filling fraction described by Equation 4.9. This change of the filling fraction is divided by the time between the two SAXS measurement points (10 minutes). Black points are equilibrium points.

the intensity does not reach its original value. This suggests that progressively more water remains within the porous material. Again, experimental artefacts can be largely excluded by the observation that for the completely water-filled mesopores at the saturation pressure ($p/p_0 = 1$) the intensity always reaches the same value as in the previous cycles. Although a connection between these two experimental observations seems to be self-evident at first sight, careful consideration of several possible connections brings us to the conclusion that they are probably not, as outlined in more detail in the following discussion.

The shift of the capillary condensation pressure must be caused by a surface modification of the silica material, eventually changing the wetting angle of the fluid–solid system. Following the theory of Saam and Cole [Saam & Cole, 1975] the adsorption branch is described by a metastable pore filling process. Obviously, in the course of the first four adsorption cycles the silica surface of SBA-15 has become distinctly more hydrophilic after each sorption cycle. In terms of the Kelvin equation this causes a lowering of the water contact angle and thus a downward shift of the capillary condensation pressure. After the ill-defined ageing period the pore condensation pressure has returned to a high value similar to that of the first adsorption cycle. Further systematic studies are necessary to gain a better understanding of the water chemisorption and related changes of surface chemistry of the silica walls. In this respect, our experimental method is highly indirect and not suitable to reach conclusive results. Therefore, we will not consider the shift of the capillary condensation pressure further in this work.

The form factor fits to the SAXS data presented in subsection 4.4.3 clearly suggest some modification of the microporous corona in each water sorption cycle. A gradual increase of the corona density as suggested by this analysis can be explained by increasingly more water remaining in the corona after each cycle. This may in turn be positively correlated with the effect discussed above, i.e. a change of the water contact angles at the pore walls. However, there remains some mismatch between the result of Figure 4.33, according to which the overall increase in the corona density in the four adsorption/desorption cycles amounts to about 3%, and Figure 4.29(B), which shows that the four adsorption/desorption cycles cause an overall decrease in the integrated intensity of more than 20%. A residual water film of increased thickness after each desorption process - which is by the way not consistent with the form factor analysis - cannot explain this observation. Hence, we conclude that structural changes of the pore walls as derived from the form factor analysis cannot alone explain the observed intensity changes. To account for the rest, we infer that water is causing some irreversible modification of the silica matrix. A massive destruction of the mesopore lattice with changes of the total pore volume should also change the total uptake of water at $p/p_0 \sim 1$, and thus the corresponding values of the integrated intensity. However, the measured intensities at $p/p_0 \sim 1$ do not indicate any considerable changes of $\bar{Q}_{Bragg}$ for the first four sorption cycles (see Figure 4.32). Hence the only reasonable hypothesis to account for this dilemma is that progressively more water remains trapped within the mesopores at the end of subsequent adsorption/desorption cycles, possibly due to an irreversible closure of some parts or sections of the mesopores.

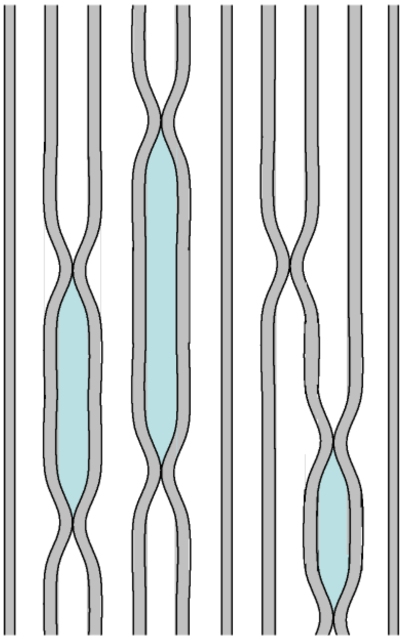

Figure 4.35: Sketch of the proposed modification of the SBA-15 mesopore network after a complete sorption cycle. Some pore wall regions have collapsed in the course of capillary condensation and evaporation. Water remains trapped within the collapsed mesopore regions. Figure taken from [Erko, 2012b].

From experimental and theoretical studies [Scherer, 1992, Dolino, 1996, Guenther, 2008, Prass, 2009, Biener, 2009, Schoen, 2010, Gor & Neimark, 2010] it is known that filling of mesoporous materials with liquids is accompanied by sorption-induced deformation of the mesoporous materials. This deformation is caused at least in part by the Laplace pressure acting at capillary condensation and evaporation. As a rough approximation, the magnitude of the circumferential (hoop) stress σ_H exerted on the cylindrical pore walls of radius R and wall thickness $2w$ is given by $\sigma_H = \Pi R/t = 2\sigma_{lv}/w$ [Prass, 2009], where Π is the Young-Laplace pressure and σ_{lv} the surface tension of the fluid (note the difference between the quantities σ_{lv} and σ_H, which are occasionally denoted by the same symbol). The contact angle is set to be zero for this simple consideration. For water with its high surface tension ($\sigma_{lv} \sim 70$ mJ m^{-2}) and a wall thickness of about 3 nm for the present SBA-15 samples [Jahnert, 2009], $\sigma_H \sim 90$ MPa. This is a remarkably high stress given the fact that it exceeds the tensile strength of (bulk) vitreous silica (50 MPa [Gretarsson, 2002]) by almost a factor of two. Therefore it is reasonable to infer that an irreversible deformation of the silica walls in SBA-15 may occur due to the capillary pressure of water. Depending on the local structure and geometry of the pore walls, this deformation may result in a local collapse of mesopore walls at mechanically weak points in the course of the sorption process. As a consequence, water would remain trapped inside closed cavities, providing a possible explanation for the observed effect. A simple sketch of the proposed scenario, visualizing the modification of the SBA-15 pore network upon repeated water sorption, is shown in Figure 4.35.

In conclusion, we have presented some new insights into the peculiarities of water sorption in silica-based ordered mesoporous materials. Repeated filling and emptying of SBA-15 mesopores with water distinctly modifies both the pore surface and the accessible pore volume of the sorbent. The density of the microporous corona increases from one sorption cycle to the next, indicating that residual water is remaining in micropores and/or some irreversible modification of the corrugated pore surface is occurring. In addition, it is proposed that sorption–strain induced irreversible pore wall deformation can lead to a local collapse of pores and trapping of water in pores between two such constrictions. Finally, our results demonstrate the importance of the sample history and ageing effects, which in the present case of water sorption in SBA-15 silica materials is causing major changes in the uptake of the liquid.

5 Conclusions and outlook

The findings of the present thesis give a new insight into the effects of confinement on the low-temperature properties of water. Moreover, an influence of water on the structural stability of confining material upon repeated adsorption and desorption cycles was found. This thesis has demonstrated that experimental studies of confined water are very complex.

- Water confined in a mesopore, previously described only by two phases, i.e. water and solid wall, was shown to be strongly dependent on the density distribution of water within the confinement volume. Confirming previously reported differential scanning calorimetry (DSC) [Schreiber, 2001, Jahnert, 2008b, Findenegg, 2008], the pore water was found to consist of at least two distinct regions. The separation of the pore water was performed by introducing the surface water, a layer closest to the pore walls with a constant thickness of around two monolayers of water molecules, and the core water in the inner part of the pores. Moreover, the core water structure was found to change systematically with confinement dimensions.

Our Raman scattering study with six different pore sizes ranging between 2.0 – 8.9 nm showed a systematic change of the core water structure with the pore size. In the weakest confinement (8.9 nm pore diameter), the core water at low temperatures was shown to be compatible with crystalline ice with a spectral fingerprint similar to bulk ice. As opposed to this, in the strongest investigated confinement (2.0 nm pore diameter) the core water was shown to transform gradually into (low-density) amorphous ice (LDA), and there is a gradual transition between these two extremes. An indication of this phenomenon was previously reported from X-ray diffraction measurements [Morishige & Kawano, 1999]. However, Bragg-peak broadening in small pores was claimed to be strongly influenced by the reduced crystal size, which would lead to similar experimental observations [Mancinelli, 2010a]. The present Raman scattering analysis should not be affected by the size of the crystal, since structural information about confined water was deduced from the position and width of the OH-stretching (OHS) mode, and therefore from the dynamical interaction of strongly hydrogen-bonded water molecules. It could further be shown that the analysis of the HOH-bending mode does not give an unambiguous information about the state of water within mesopores. A signal of this mode has been observed in the entire temperature region in all samples, even in those where core water was clearly shown to freeze.

Hence, the presence of the this signal cannot be taken as evidence for the liquid state of water in pores as it was suggested in earlier studies, e.g. in Ref. [Mallamace, 2007b].

- The two sections of pore water were found to be characterised by different density values, and were shown to develop different intermolecular structures upon cooling. This could be attributed to the different degree of development of the hydrogen bond network between water molecules in the two spacial pore regions. A distinct tetrahedral hydrogen-bonded water network was found only in the core part of the pores, and no hydrogen-bonded water network was found for the layer closest to the pore surface. The different temperature behaviour of these two sub-sections of pore water was not considered in previous analyses of our and other similar systems (see e.g. Refs. [Liu, 2007, Kamitakahara, 2012]).

The temperature behaviour of the density of confined water was studied by means of combined *in situ* small-angle scattering of X-rays (SAXS) and neutrons (SANS), and corroborated by additional wide-angle X-ray scattering (WAXS). Building on our Raman results, a two-step density model was applied for the description of water confined in silica mesopores. This approach revealed the surface water to have a higher density than the residual core water in the central part of the pores. The average density of pore water systematically changes with temperature, showing a minimum at different temperatures, which depend on the pore size. In contrast to previous interpretations of this effect [Liu, 2007, Zhang, 2009, Kamitakahara, 2012], the temperature of this minimum was shown to be connected to the core water phase transition point. The density model consistently connects the scattering signal from both X-rays and neutrons with the average pore water density. It shows further that during cooling and heating the changes of the core water density exceed the corresponding density changes of the surface water by several times. It has to be noted that changes of water density are usually induced by a modification of water hydrogen bond network. Our Raman results show that the surface water does not develop a strong hydrogen bond network upon cooling. Therefore, the observed changes of the surface water density are attributed to the restrictions of the two-step SAXS model.

The present study might be improved by high-accuracy measurements of more than just three Bragg-reflections from the mesoporous pore lattice. A more detailed structure of the surface water layer and also that of the core water could then be obtained by an advanced modelling of higher-order reflections. Unfortunately, for MCM-41-type materials usually only three (or even less) diffraction orders can be observed [Jahnert, 2008a, Prass, 2011]. From our selection, the only suitable material for these purposes is SBA89, showing up to ten Bragg peak orders [Jahnert, 2008a]. However, the fraction of surface water in this material is very low, giving only about 2 % of the entire pore water fraction. Moreover, the complex wall structure of SBA89, including the microporous corona represents an extra parameter which would make the analysis more difficult.

- The thickness of the surface water layer was found to be independent on the pore size and showed only small changes with temperature. A structural change of the surface layer is found to be independent on the pore size, taking place in the temperature region around 160 K - 180 K.

The average water density minimum observed for the sample with smallest pores (2.0 nm diameter) around 180 K is attributed to a different phenomenon than the core water phase transition. Unfortunately, due to low pore ordering of this sample, only scattering from a single Bragg peak could be observed in the experiments. Therefore it was not possible to unambiguously distinguish between the signal from the core water and that from the surface water. However, the scattering signal should mainly originate from surface water, since its fraction within the pores of 2.0 nm size was estimated to be around 84 %. Four arguments support the suggestion that the observed pore water density minimum around 180 K can be attributed to a structural change of the surface water:

1. Recently reported dynamical transition of the surface layer in MCM-41-S materials with similar size was found to take place in the temperature region around 180 K [Bruni, 2011].
2. Pore lattice deformation, indicating a water phase transition, is extracted from our SAXS measurements of water-filled MCM20 in the same temperature region.
3. Data from our Raman scattering experiments and DSC studies [Jahnert, 2008b, Findenegg, 2008] show no freezing point of core water inside pores with diameters smaller than 2.5 nm.
4. Measurements of water confined in hydrophobic confinement of similar size, where no surface water layer exists, show no water density minimum in the entire temperature region [Zhang, 2009].

An extension of this study should include materials with a similar pore size of around 2.0 nm, however, with higher pore ordering, for which more than only one Bragg peak can be analysed. Detailed information about the temperature behaviour of the different pore water regions could then be obtained by applying an advanced form factor model including more than just two pore water phases. Studies reported in Refs. [Mancinelli, 2009, Mancinelli, 2010b, Mancinelli, 2010a, Mancinelli, 2011] seem to use such materials. The detailed properties of MCM-41 are determined by number of parameters depending on their synthesis.

The surface water layer may be further studied by means of polarised Raman scattering. Different mutual orientations of water molecules lead to a modified polarisation of the Raman signal [Masic, 2011]. Consequently, polarisation analysis of the Raman signal from partially filled samples can give detailed information about the structure of the surface layer. A systematic study of the temperature behaviour of the Raman signal including different polarisation angles would show possible temperature-induced reorientation of water molecules closest to the silica surface. Similar information can be obtained from Raman scattering experiments using partially deuterated water, instead of pure H_2O. Different network structure of HOD molecules give sufficiently different Raman signal in the OHS spectral region [Fecko, 2003, Dellago, 2011, Weinwurm & Dellago, 2011]. The analysis of Raman spectra from oriented HDO molecules would be even supported by existing theoretical models of such systems [Kofinger, 2008, Kofinger & Dellago, 2010]. Here, the main challenge involves the finding of mesorporous materials with similar properties like MCM-41 or SBA-15 (i.e. small hydrophilic cylindrical pores with a narrow size distribution), however, with a macroscopically oriented pore structure.

- The present thesis demonstrates an alternative determination of water liquid-solid phase transition temperatures in confinement. It is performed by a new analysis of the water OHS region of the Raman spectrum. Hereby, the phase transition of water in pores is characterised by a shift of the OHS signal.

For bulk water, and for water in largest investigated confinement of 8.9 nm the spectral shift of the Raman OHS signal is clear and discontinuous. The magnitude of this shift decreases with decreasing pore size. Water phase transition temperatures obtained by this method are in excellent agreement with those from DSC measurements performed independently on the same samples [Schreiber, 2001, Jahnert, 2008b, Findenegg, 2008]. Hence, our study shows that for pore sizes down to 3 nm, the freezing/melting point depression with decreasing pore size can be consistently described by a modified Gibbs-Thomson equation, with a nonfreezable water layer of about two monolayers close to the pore walls. It is a remarkable finding, since it shows that the thermodynamic Gibbs-Thomson equation is applicable down to the nanometer scale. For smallest investigated confinement with pore sizes < 2.5 nm the OHS signal changes gradually within the entire investigated temperature region. This shows essentially the same trend as the exothermic/endothermic heat transfer in DSC measurements. Hence, in agreement to these previous DCS studies, our Raman study shows no indication for a first-order phase transition for water in such small pores.

- Studying the pore lattice deformation upon cooling and heating of water-filled mesopores, a new interpretation for the strain-temperature behaviour for temperatures above the core water phase transition point is given. Hereby, the similarity between the liquid-vapour and the solid-liquid phase transitions of water in confinement, was studied.

The description of the observed pore lattice deformation taking place during capillary condensation and evaporation in mesopores [Prass, 2011] could be successfully applied for the description of similar observations during freezing and melting of core water. Formation of a curved liquid-solid interface, leading to a negative Young-Laplace pressure, was shown to give an appropriate explanation for the observed effects. Thus, contraction of the pore lattice upon cooling was shown to be explained in a similar way as that observed during fluid desorption from mesopores, namely by the growth of a liquid meniscus. It has to be noted, however, that the effects are not necessarily restricted to the presence of a curved surface. Both, Kelvin equation and Gibbs-Thomson equation can be also derived without using the effect of curvature [Schoen, 2010]. The most important aspect is the surface/volume ratio, giving the term $1/R$ in both equations. The magnitude of pore lattice deformation is determined by the specific interface energy of the two interacting phases. For water ad- and desorption this quantity is the surface tension σ_{lv}, for water melting and freezing it is the liquid-solid specific interaction energy σ_{sl}. The calculated values for the effective pore-load elastic modulus of the three MCM-41 type materials with the largest pore sizes are in good agreement with those reported in [Prass, 2009] from the desoprtion data of pentane.

The water freezing model from the present study can also be applied for studies of liquid-solid transitions of other confined fluids. However, further analyses are required in order to understand the influence of the different approaches used for determining the Bragg peak position of the mesoposous lattice. In the present study, results obtained from fitting the Bragg peak intensity by a Gaussian curve showed almost negligible deviations from those using the centre of mass of the peak. Hereby, the difference in density of the two interacting phases hast to be taken into account. This density change of the sorbate upon adsorption and desorption is regarded to strongly influence the symmetry of the Bragg peak. The contrast change of the pore walls upon micropore filling and emptying is suggested to distinctly modify the form factor of the cylindrical mesopores [Prass, 2011]. Thus, in such studies the choice of the “correct” determination of the lattice parameter is more critical than in studies of freezing and melting processes, where the changes in density are relatively small. However, more studies are required in order to understand this effect.

- An *in situ* sorption apparatus was developed for studies of phase transition processes in ordered mesoporous materials using a laboratory small-angle X-ray scattering device. A first application of this new instrument revealed irreversible changes of SBA-15 material upon repeated water sorption cycles.

Capillary condensation pressure of water in SBA-15 was shown to shift progressively to lower relative pressure values with increasing number of sorption cycles. This effect could be attributed to chemisorption of water at the silica walls, resulting in a change of the fluid–wall interaction. The study further showed that progressively more water remains trapped within the porous material after each cycle. This effect is interpreted to be the result of an irreversible collapse of parts of mesopores, originating from pore wall deformation due to the large Young-Laplace pressure of water acting on the pore walls at capillary condensation and capillary evaporation. Future studies along these lines should include repeated cooling and heating cycles of both, water-filled and empty samples. From subsequently performed cycles of water-filled samples frost damages of the mesoporous structure can be investigated in detail. Since pore lattice deformation during freezing and melting was shown to be in the same order of magnitude as those for capillary condensation and evaporation, similar destructions of the pore matrix can be expected.

Cooling and heating of an “aged” sample in its empty state can give important information about the water trapped within collapsed mesopore regions. The amount if this water can even be calculated quantitatively by analysing the sample contrast change upon cooling and heating. Strain isosteres of aged samples can further provide information about the mechanical properties of collapsed pore regions.

•

Finally at the end of this thesis I want to come back to the general question, i.e. to which extent the “trick” of confining water into pores of only few nanometers really opens new possibilities to experimentally extract information for bulk water in the “no-man’s land”. In particular, the question was if there is an influence of confinement other than the stabilisation of the liquid phase at very low temperatures, and whether results obtained from experiments with similar confining systems can truly validate computer simulation results for bulk water?

The results of this thesis strongly question this, providing very strong evidence that confinement effects on water structure become increasingly more important as pore size decreases. The temperature dependence of water confined in ordered cylindrical mesopores of MCM-41 and SBA-15 materials was shown to be sufficiently different from pure bulk water. Thus, the present work demonstrates the relevance of studies of confined systems. Investigating the water properties in confinement is fundamentally important to many different fields. While bulk liquid water cannot exist at low temperatures, it certainly can be observed in nanoporous rocks and on their surfaces, in small droplets and as thin layers on proteins in the atmosphere distinctly below the bulk water freezing point. Hence, studying water properties in strong confinement provides important insights into the life mechanisms in nature. However, there are still many open questions giving the basis for future works aiming at the development of a coherent picture about the properties of water.

6 Acknowledgments

First of all, I would like to thank my supervisor, Prof. Oskar Paris for his support throughout the entire five years that I worked with him. I am most grateful for the opportunity he provided me to take part in starting up a new working group, and in developing a new X-ray laboratory within my PhD study at the University in Leoben. He helped me a lot and was always able to give a good advise in scientific matters, as well as in personal questions.

I would like to thank the entire Institute of Physics, including the colleagues from the working groups around Prof. Teichert, Prof. Meisels, and Prof. Oswald, and especially the secretary's office, Heide Kirchberger and Magdalena Ottrin for their advising on organisation matters. I would like to thank Heinz Pirker and Peter Moharitsch for their technical support and particularly Christian Stecher for his effort in software development. I would also like to thank Roland Morak for his help during the experiments performed at the laboratory and at the large-scale facilities.

I appreciate the help of my colleagues Markus Hartmann, Rainer Lechner and Gerhard Popovski throughout the entire duration of my PhD, and particularly their support while I was writing my thesis.

I am deeply grateful to Prof. Findenegg for fruitful discussions, and to Dirk Wallacher for his support in technical questions. I would like to thank Johannes Prass for his help throughout the entire time we worked together. I owe my deepest gratitude to Alan Michette for organising the experiment in London.

Finally, I would like to express my gratitude to my family. Their enormous support helped me to achieve these results so far. Especially, my wife Irina is my strongest support.

Bibliography

[Akcakayiran, 2008] Akcakayiran, D. (2008). *Pure and acid-functionalized ordered mesoporous silicas: Hosts for metallo-supramolecular coordination polymers.* PhD thesis, Berlin.

[Akcakayiran, 2005] Akcakayiran, D., Kurth, D. G., Rohrs, S., Rupprechter, G., & Findenegg, G. H. (2005). Self-assembly of a metallosupramolecular coordination polyelectrolyte in the pores of SBA-15 and MCM-41 silica. *Langmuir*, 21(16), 7501–7506.

[Alba-Simionesco, 2006] Alba-Simionesco, C., Coasne, B., Dosseh, G., Dudziak, G., Gubbins, K. E., Radhakrishnan, R., & Sliwinska-Bartkowiak, M. (2006). Effects of confinement on freezing and melting. *Journal of Physics: Condensed Matter*, 18(6), R15–R68.

[Angell, 2002] Angell, C. A. (2002). Liquid fragility and the glass transition in water and aqueous solutions. *Chemical Reviews*, 102(8), 2627–2649.

[Angell, 2008] Angell, C. A. (2008). Insights into phases of liquid water from study of its unusual glass-forming properties. *Science*, 319(5863), 582–587.

[Angell, 1982] Angell, C. A., Oguni, M., & Sichina, W. J. (1982). Heat-Capacity of Water at Extremes of Supercooling and Superheating. *Journal of Physical Chemistry*, 86(6), 998–1002.

[Antoniou, 1964] Antoniou, A. A. (1964). Phase Transformations of Water in Porous Glass. *Journal of Physical Chemistry*, 68(10), 2754.

[Antonow, 1907] Antonow, G. (1907). Surface tension at the limit of two layers. *Journal de Chimie Physique*, 5, 372–385.

[Batchelor & Foster, 1944] Batchelor, R. W. & Foster, A. G. (1944). The freezing point of adsorbed liquids. *Transactions of the Faraday Society*, 40, 0300–0305.

[Bates, 2008] Bates, B., Kundzewicz, Z., Wu, S., & Palutikof, J. (2008). *Climate Change and Water. Technical Paper of the Intergovernmental Panel on Climate Change.* Geneva: IPCC Secretariat.

[Beck, 1992] Beck, J. S., Vartuli, J. C., Roth, W. J., Leonowicz, M. E., Kresge, C. T., Schmitt, K. D., Chu, C. T. W., Olson, D. H., Sheppard, E. W., Mccullen, S. B., Higgins, J. B., & Schlenker, J. L. (1992). A New Family of Mesoporous Molecular-Sieves Prepared with Liquid-Crystal Templates. *Journal of the American Chemical Society*, 114(27), 10834–10843.

[Bellissent-Funel, 1993] Bellissent-Funel, M. C., Lal, J., & Bosio, L. (1993). Structural Study of Water Confined in Porous-Glass by Neutron-Scattering. *Journal of Chemical Physics*, 98(5), 4246–4252.

[Bellissent-Funel, 2000] Bellissent-Funel, M. C., Longeville, S., Zanotti, J. M., & Chen, S. H. (2000). Experimental observation of the a relaxation in supercooled water. *Physical Review Letters*, 85(17), 3644–3647.

[Bellissent-Funel, 1996] Bellissent-Funel, M. C., Sridi-Dorbez, R., & Bosio, L. (1996). X-ray and neutron scattering studies of the structure of water at a hydrophobic surface. *Journal of Chemical Physics*, 104(24), 10023–10029.

[Berendsen, 1987] Berendsen, H. J. C., Grigera, J. R., & Straatsma, T. P. (1987). The Missing Term in Effective Pair Potentials. *Journal of Physical Chemistry*, 91(24), 6269–6271.

[Bernal & Fowler, 1933] Bernal, J. D. & Fowler, R. H. (1933). A theory of water and ionic solution, with particular reference to hydrogen and hydroxyl ions. *Journal of Chemical Physics*, 1(8), 515–548.

[Bertie & Whalley, 1964] Bertie, J. E. & Whalley, E. (1964). Infrared Spectra of Ices Ih + Ic in Range 4000 to 350 Cm Minus 1. *Journal of Chemical Physics*, 40(6), 1637–.

[Beurroies, 2004] Beurroies, I., Denoyel, R., Llewellyn, P., & Rouquerol, J. (2004). A comparison between melting-solidification and capillary condensation hysteresis in mesoporous materials: application to the interpretation of thermoporometry data. *Thermochimica Acta*, 421(1-2), 11–18.

[Biener, 2009] Biener, J., Wittstock, A., Zepeda-Ruiz, L. A., Biener, M. M., Zielasek, V., Kramer, D., Viswanath, R. N., Weissmuller, J., Baumer, M., & Hamza, A. V. (2009). Surface-chemistry-driven actuation in nanoporous gold. *Nature Materials*, 8(1), 47–51.

[Blin & Carteret, 2007] Blin, J. L. & Carteret, C. (2007). Investigation of the silanols groups of mesostructured silica prepared using a fluorinated surfactant: Influence of the hydrothermal temperature. *Journal of Physical Chemistry C*, 111(39), 14380–14388.

[Boissiere, 2005] Boissiere, C., Grosso, D., Lepoutre, S., Nicole, L., Bruneau, A. B., & Sanchez, C. (2005). Porosity and mechanical properties of mesoporous thin films assessed by environmental ellipsometric porosimetry. *Langmuir*, 21(26), 12362–12371.

[Borick, 1995] Borick, S. S., Debenedetti, P. G., & Sastry, S. (1995). A Lattice Model of Network-Forming Fluids with Orientation-Dependent Bonding - Equilibrium, Stability, and Implications for the Phase-Behavior of Supercooled Water. *Journal of Physical Chemistry*, 99(11), 3781–3792.

[Brovchenko & Oleinikova, 2008] Brovchenko, I. & Oleinikova, A. (2008). *Interfacial and confined water*. Amsterdam: Elsevier.

[Broyer, 2002] Broyer, M., Valange, S., Bellat, J. P., Bertrand, O., Weber, G., & Gabelica, Z. (2002). Influence of aging, thermal, hydrothermal, and mechanical treatments on the porosity of MCM-41 mesoporous silica. *Langmuir*, 18(13), 5083–5091.

[Brubach, 2005] Brubach, J. B., Mermet, A., Filabozzi, A., Gerschel, A., & Roy, P. (2005). Signatures of the hydrogen bonding in the infrared bands of water. *Journal of Chemical Physics*, 122(18).

[Brumberger, 1995] Brumberger, H. (1995). *Modern Aspects of Small-Angle Scattering*. Dordrecht: Kluwer Academic Publishers.

[Brun, 1977] Brun, M., Lallemand, A., Quinson, J. F., & Eyraud, C. (1977). New Method for Simultaneous Determination of Size and Shape of Pores - Thermoporometry. *Thermochimica Acta*, 21(1), 59–88.

[Bruni, 2011] Bruni, F., Mancinelli, R., & Ricci, M. A. (2011). Multiple relaxation processes versus the fragile-to-strong transition in confined water. *Physical Chemistry Chemical Physics*, 13(44), 19773–19779.

[Burgess, 1989] Burgess, C. G. V., Everett, D. H., & Nuttall, S. (1989). Adsorption Hysteresis in Porous Materials. *Pure and Applied Chemistry*, 61(11), 1845–1852.

[Burton & Oliver, 1936] Burton, E. & Oliver, W. (1936). The crystal structure of ice at low temperatures. *Proc. R. Soc. Lond. A*, 153, 166–172.

[Cai, 1999] Cai, Q., Lin, W. Y., Xiao, F. S., Pang, W. Q., Chen, X. H., & Zou, B. S. (1999). The preparation of highly ordered MCM-41 with extremely low surfactant concentration. *Microporous and Mesoporous Materials*, 32(1-2), 1–15.

[Chemgapedia, 2011] Chemgapedia (2011). http://www.chemgapedia.de/.

[Chen, 2006a] Chen, S. H., Liu, L., Fratini, E., Baglioni, P., Faraone, A., & Mamontov, E. (2006a). Observation of fragile-to-strong dynamic crossover in protein hydration water. *Proceedings of the National Academy of Sciences of the United States of America*, 103(24), 9012–9016.

[Chen, 2006b] Chen, S. H., Mallamace, F., Mou, C. Y., Broccio, M., Corsaro, C., Faraone, A., & Liu, L. (2006b). The violation of the Stokes-Einstein relation in supercooled water. *Proceedings of the National Academy of Sciences of the United States of America*, 103(35), 12974–12978.

[Christenson, 2001] Christenson, H. K. (2001). Confinement effects on freezing and melting. *Journal of Physics-Condensed Matter*, 13(11), R95–R133.

[Ciccariello & Benedetti, 1985] Ciccariello, S. & Benedetti, A. (1985). Parameterizations of Scattering Intensities and Values of the Angularities and of the Interphase Surfaces for 3-Component Amorphous Samples. *Journal of Applied Crystallography*, 18(Aug), 219–229.

[Ciesla & Schuth, 1999] Ciesla, U. & Schuth, F. (1999). Ordered mesoporous materials. *Microporous and Mesoporous Materials*, 27(2-3), 131–149.

[Cohan, 1938] Cohan, L. H. (1938). Sorption hysteresis and the vapor pressure of concave surfaces. *Journal of the American Chemical Society*, 60, 433–435.

[CSRRI, 2012] CSRRI (2012). http://csrri.iit.edu/periodic-table.

[Czihak, 2000] Czihak, C., Muller, M., Schober, H., & Vogl, G. (2000). Ice formation in amorphous cellulose. *Physica B*, 276, 286–287.

[D'Arrigo, 1981] D'Arrigo, G., Maisano, G., Mallamace, F., Migliardo, P., & Wanderlingh, F. (1981). Raman-Scattering and Structure of Normal and Supercooled Water. *Journal of Chemical Physics*, 75(9), 4264–4270.

[Davis, 1988] Davis, M. E., Saldarriaga, C., Montes, C., Garces, J., & Crowder, C. (1988). A Molecular-Sieve with 18-Membered Rings. *Nature*, 331(6158), 698–699.

[Debenedetti, 1996] Debenedetti, P., Poole, P. H., Sastry, S., Sciortino, F., & Stanley, H. E. (1996). Physics of supercooled water. *Abstracts of Papers of the American Chemical Society*, 212, 209.

[Debenedetti & Stanley, 2003] Debenedetti, P. G. & Stanley, H. E. (2003). Supercooled and glassy water. *Physics Today*, 56(6), 40–46.

[Debenedetti & Stillinger, 2001] Debenedetti, P. G. & Stillinger, F. H. (2001). Supercooled liquids and the glass transition. *Nature*, 410(6825), 259–267.

[Dellago, 2011] Dellago, C. (2011). Personal communication.

[Denoyel & Pellenq, 2002] Denoyel, R. & Pellenq, R. J. M. (2002). Simple phenomenological models for phase transitions in a confined geometry. 1: Melting and solidification in a cylindrical pore. *Langmuir*, 18(7), 2710–2716.

[Dill & Bromberg, 2011] Dill, K. A. & Bromberg, S. (2011). *Molecular Driving Forces*. New Your: Garland Science.

[Dolino, 1996] Dolino, G., Bellet, D., & Faivre, C. (1996). Adsorption strains in porous silicon. *Physical Review B*, 54(24), 17919–17929.

[Dowell & Rinfret, 1960] Dowell, L. G. & Rinfret, A. P. (1960). Low-Temperature Forms of Ice as Studied by X-Ray Diffraction. *Nature*, 188(4757), 1144–1148.

[Edler & White, 1997] Edler, K. J. & White, J. W. (1997). Further improvements in the long-range order of MCM-41 materials. *Chemistry of Materials*, 9(5), 1226–1233.

[EET, 2012] EET (2012). Environmental Engineering Technology at Three Rivers Community College.

[Eisenberg & Kauzmann, 1969] Eisenberg, D. & Kauzmann, W. (1969). *The Structure and Properties of Water*. New York: Oxford University Press.

[Engemann, 2004] Engemann, S., Reichert, H., Dosch, H., Bilgram, J., Honkimaki, V., & Snigirev, A. (2004). Interfacial melting of ice in contact with SiO2. *Physical Review Letters*, 92(20), 205701.

[Enustun, 1978] Enustun, B. V., Senturk, H. S., & Yurdakul, O. (1978). Capillary Freezing and Melting. *Journal of Colloid and Interface Science*, 65(3), 509–516.

[Erko, 2000] Erko, A., Packe, I., Hellwig, C., Fieber-Erdmann, M., Pawlitzki, O., Veldkamp, M., & Gudat, W. (2000). KMC-2: the new X-ray beamline at BESSY II. *AIP Conference Proceedings*, 521, 415–418.

[Erko, 2008] Erko, M. (2008). Untersuchung der Domaenenbildung bei der Kondensation und der Verdampfung von Fluessigkeiten in mesoporoesem Silika-Material SBA-15 mittels Neutronen-Kleinwinkelstreuung (SANS). Master's thesis, Freie Universitaet Berlin, Fachbereich Physik, Berlin.

[Erko, 2010] Erko, M., Brandt, A., Wallacher, D., & Paris, O. (2010). In-situ small-angle neutron scattering study of pore filling and pore emptying in ordered mesoporous silica. *Journal of Applied Crystallography*, 43, 1–7.

[Erko, 2011] Erko, M., Findenegg, G. H., Cade, N., Michette, A. G., & Paris, O. (2011). Confinement-induced structural changes of water studied by Raman scattering. *Physical Review B*, 84, 104205.

[Erko, 2012a] Erko, M., Hoell, A., Wallacher, D., Hauss, T., Zizak, I., & Paris, O. (2012a). Density minimum of confined water at low temperatures: a combined study by small-angle scattering of X-rays and neutrons. *Physical Chemistry Chemical Physics*, 14, 3852–3858.

[Erko, 2012b] Erko, M., Wallacher, D., Findenegg, G. H., & Paris, O. (2012b). Repeated sorption of water in SBA-15 investigated by means of in situ small-angle X-ray scattering. *Journal of Physics: Condensed Matter*, 24, accepted.

[Everett, 1961] Everett, D. H. (1961). Thermodynamics of Frost Damage to Porous Solids. *Transactions of the Faraday Society*, 57(9), 1541.

[Faivre, 2000] Faivre, C., Bellet, D., & Dolino, G. (2000). In situ X-ray diffraction investigation of porous silicon strains induced by the freezing of a confined organic fluid. *European Physical Journal B*, 16(3), 447–454.

[Fan, 2007] Fan, H. Y., Hartshorn, C., Buchheit, T., Tallant, D., Assink, R., Simpson, R., Kisse, D. J., Lacks, D. J., Torquato, S., & Brinker, C. J. (2007). Modulus-density scaling behaviour and framework architecture of nanoporous self-assembled silicas. *Nature Materials*, 6(6), 418–423.

[Faraone, 2003a] Faraone, A., Liu, L., Mou, C. Y., Shih, P. C., Brown, C., Copley, J. R. D., Dimeo, R. M., & Chen, S. H. (2003a). Dynamics of supercooled water in mesoporous silica matrix MCM-48-S. *European Physical Journal E*, 12, S59–S62.

[Faraone, 2003b] Faraone, A., Liu, L., Mou, C. Y., Shih, P. C., Copley, J. R. D., & Chen, S. H. (2003b). Translational and rotational dynamics of water in mesoporous silica materials: MCM-41-S and MCM-48-S. *Journal of Chemical Physics*, 119(7), 3963–3971.

[Fecko, 2003] Fecko, C. J., Eaves, J. D., Loparo, J. J., Tokmakoff, A., & Geissler, P. L. (2003). Ultrafast hydrogen-bond dynamics in the infrared spectroscopy of water. *Science*, 301(5640), 1698–1702.

[Feldman, 1970] Feldman, R. F. (1970). Length Change-Adsorption Relations for Water-Porous Glass System to-40 Degrees C. *Canadian Journal of Chemistry*, 48(2), 287.

[Findenegg, 2008] Findenegg, G. H., Jahnert, S., Akcakayiran, D., & Schreiber, A. (2008). Freezing and Melting of Water Confined in Silica Nanopores. *Chemphyschem*, 9(18), 2651–2659.

[Findenegg, 2010] Findenegg, G. H., Jahnert, S., Muter, D., Prass, J., & Paris, O. (2010). Fluid adsorption in ordered mesoporous solids determined by in situ small-angle X-ray scattering. *Physical Chemistry Chemical Physics*, 12(26), 7211–7220.

[Finney, 2002] Finney, J. L., Bowron, D. T., Soper, A. K., Loerting, T., Mayer, E., & Hallbrucker, A. (2002). Structure of a new dense amorphous ice. *Physical Review Letters*, 89(20).

[Franks, 1975] Franks, F. (1975). *Water: A Comprehensive Treatise*. New York: Springer.

[Franks, 2000] Franks, F. (2000). *Water: A Matrix of Life*, volume 2nd ed. Cambridge UK: Royal Society of Chemistry.

[Franzese & Stanley, 2007] Franzese, G. & Stanley, H. E. (2007). The Widom line of supercooled water. *Journal of Physics-Condensed Matter*, 19(20), 205126.

[Furic & Volovsek, 2010] Furic, K. & Volovsek, V. (2010). Water ice at low temperatures and pressures: New Raman results. *Journal of Molecular Structure*, 976(1-3), 174–180.

[Galarneau, 2003] Galarneau, A., Cambon, N., Di Renzo, F., Ryoo, R., Choi, M., & Fajula, F. (2003). Microporosity and connections between pores in SBA-15 mesostructured silicas as a function of the temperature of synthesis. *New Journal of Chemistry*, 27(1), 73–79.

[Gallo & Rovere, 2007] Gallo, P. & Rovere, M. (2007). Structural properties and liquid spinodal of water confined in a hydrophobic environment. *Physical Review E*, 76(6), 061202.

[Gallo, 2010a] Gallo, P., Rovere, M., & Chen, S. H. (2010a). Anomalous dynamics of water confined in MCM-41 at different hydrations. *Journal of Physics-Condensed Matter*, 22(28), 284102.

[Gallo, 2010b] Gallo, P., Rovere, M., & Chen, S. H. (2010b). Dynamic Crossover in Supercooled Confined Water: Understanding Bulk Properties through Confinement. *Journal of Physical Chemistry Letters*, 1(4), 729–733.

[Geiger & Stanley, 1982] Geiger, A. & Stanley, H. E. (1982). Low-Density Patches in the Hydrogen-Bond Network of Liquid Water - Evidence from Molecular-Dynamics Computer-Simulations. *Physical Review Letters*, 49(24), 1749–1752.

[Glatter & O.Kratky, 1982] Glatter, O. & O.Kratky (1982). *Small Angle X-ray Scattering*. London: Academic Press.

[Gor & Neimark, 2010] Gor, G. Y. & Neimark, A. V. (2010). Adsorption-Induced Deformation of Mesoporous Solids. *Langmuir*, 26(16), 13021–13027.

[Gretarsson, 2002] Gretarsson, A. (2002). Referenes for tensile strength of vitreous silica at room temperature.

[Grün, 1997] Grün, M., Unger, K., Matsumoto, A., & Tsutsumi, K. (1997). *Characterisation of Porous Solids (COPS) IV*. London: The Royal Society of Chemistry.

[Gruener, 2009] Gruener, S., Hofmann, T., Wallacher, D., Kityk, A. V., & Huber, P. (2009). Capillary rise of water in hydrophilic nanopores. *Physical Review E*, 79(6), 067301.

[Grunberg, 2004] Grunberg, B., Emmler, T., Gedat, E., Shenderovich, J., Findenegg, G. H., Limbach, H. H., & Buntkowsky, G. (2004). Hydrogen bonding of water confined in mesoporous silica MCM-41 and SBA-15 studied by H-1 solid-state NMR. *Chemistry-a European Journal*, 10(22), 5689–5696.

[Guenther, 2008] Guenther, G., Prass, J., Paris, O., & Schoen, M. (2008). Novel insights into nanopore deformation caused by capillary condensation. *Physical Review Letters*, 101(8).

[Guinier, 1994] Guinier, A. (1994). *X-ray Diffraction*. New York: Dover Publications Inc.

[Handa & Klug, 1988] Handa, Y. P. & Klug, D. D. (1988). Heat-Capacity and Glass-Transition Behavior of Amorphous Ice. *Journal of Physical Chemistry*, 92(12), 3323–3325.

[Handa, 1992] Handa, Y. P., Zakrzewski, M., & Fairbridge, C. (1992). Effect of Restricted Geometries on the Structure and Thermodynamic Properties of Ice. *Journal of Physical Chemistry*, 96(21), 8594–8599.

[Hare & Sorensen, 1987] Hare, D. E. & Sorensen, C. M. (1987). The Density of Supercooled Water .2. Bulk Samples Cooled to the Homogeneous Nucleation Limit. *Journal of Chemical Physics*, 87(8), 4840–4845.

[Hedstrom, 2007] Hedstrom, J., Swenson, J., Bergman, R., Jansson, H., & Kittaka, S. (2007). Does confined water exhibit a fragile-to-strong transition? *European Physical Journal-Special Topics*, 141, 53–56.

[Heide, 1984] Heide, H. G. (1984). Observations on Ice Layers. *Ultramicroscopy*, 14(3), 271–278.

[Hesse, 1991] Hesse, M., Meier, H., & Zeeh, B. (1991). *Spektroskopische Methoden in der organischen Chemie*. Stuttgart: Georg Thieme Verlag.

[Hodgson & Mcintosh, 1960] Hodgson, C. & Mcintosh, R. (1960). The Freezing of Water and Benzene in Porous Vycor Glass. *Canadian Journal of Chemistry-Revue Canadienne De Chimie*, 38(6), 958–971.

[Hofer, 1991] Hofer, K., Astl, G., Mayer, E., & Johari, G. P. (1991). Vitrified Dilute Aqueous-Solutions. 4. Effects of Electrolytes and Polyhydric Alcohols on the Glass-Transition Features of Hyperquenched Aqueous-Solutions. *Journal of Physical Chemistry*, 95(26), 10777–10781.

[Hoffmann, 2006] Hoffmann, F., Cornelius, M., Morell, J., & Froba, M. (2006). Silica-based mesoporous organic-inorganic hybrid materials. *Angewandte Chemie-International Edition*, 45(20), 3216–3251.

[Hofmann, 2005] Hofmann, T., Wallacher, D., Huber, P., Birringer, R., Knorr, K., Schreiber, A., & Findenegg, G. H. (2005). Small-angle x-ray diffraction of Kr in mesoporous silica: Effects of microporosity and surface roughness. *Physical Review B*, 72(6).

[Hunter, 2001] Hunter, R. J. (2001). *Foundations of Colloid Science*. New York: Oxford University Press Inc.

[Imperor-Clerc, 2000] Imperor-Clerc, M., Davidson, P., & Davidson, A. (2000). Existence of a microporous corona around the mesopores of silica-based SBA-15 materials templated by triblock copolymers. *Journal of the American Chemical Society*, 122(48), 11925–11933.

[Impey, 2011] Impey, C. (2011). *The Living Cosmos*. New York: Cambridge University Press.

[Jahnert, 2008a] Jahnert, S. (2008a). *Untersuchung von reinen Stoffen in periodisch mesoporösen Silikamaterialien mit thermophysikalischen Methoden und in-situ Röntgenkleinwinkelstreuung*. PhD thesis, TU Berlin, Fakultät II Mathematik und Naturwissenschaften, Berlin.

[Jahnert, 2008b] Jahnert, S., Chavez, F. V., Schaumann, G. E., Schreiber, A., Schonhoff, M., & Findenegg, G. H. (2008b). Melting and freezing of water in cylindrical silica nanopores. *Physical Chemistry Chemical Physics*, 10(39), 6039–6051.

[Jahnert, 2009] Jahnert, S., Muter, D., Prass, J., Zickler, G. A., Paris, O., & Findenegg, G. H. (2009). Pore Structure and Fluid Sorption in Ordered Mesoporous Silica. I. Experimental Study by in situ Small-Angle X-ray Scattering. *Journal of Physical Chemistry C*, 113(34), 15201–15210.

[Jaroniec & Solovyov, 2006] Jaroniec, M. & Solovyov, L. A. (2006). Improvement of the Kruk-Jaroniec-Sayari method for pore size analysis of ordered silicas with cylindrical mesopores. *Langmuir*, 22(16), 6757–6760.

[Jenniskens & Blake, 1994] Jenniskens, P. & Blake, D. F. (1994). Structural Transitions in Amorphous Water Ice and Astrophysical Implications. *Science*, 265(5173), 753–756.

[Johari, 2009] Johari, G. P. (2009). Origin of the enthalpy features of water in 1.8 nm pores of MCM-41 and the large C(p) increase at 210 K. *Journal of Chemical Physics*, 130(12).

[Jorgensen, 1983] Jorgensen, W. L., Chandrasekhar, J., Madura, J. D., Impey, R. W., & Klein, M. L. (1983). Comparison of Simple Potential Functions for Simulating Liquid Water. *Journal of Chemical Physics*, 79(2), 926–935.

[Kamitakahara, 2012] Kamitakahara, W. A., Faraone, A., Liu, K. H., & Mou, C. (2012). Temperature dependence of structure and density for D2O confined in MCM-41-S. *Journal of Physics: Condensed Matter*, 24(064106).

[Khodakov, 2005] Khodakov, A. Y., Zholobenko, V. L., Imperor-Clerc, M., & Durand, D. (2005). Characterization of the initial stages of SBA-15 synthesis by in situ time-resolved small-angle X-ray scattering. *Journal of Physical Chemistry B*, 109(48), 22780–22790.

[Kikkinides, 2003] Kikkinides, E. S., Kainourgiakis, M. E., & Stubos, A. K. (2003). Origin of hysteresis of gas adsorption in disordered porous media: Lattice gas model versus percolation theory. *Langmuir*, 19(8), 3338–3344.

[Knorr, 2008] Knorr, K., Huber, P., & Wallacher, D. (2008). Thermodynamic and structural investigations of condensates of small molecules in mesopores. *Zeitschrift Fur Physikalische Chemie-International Journal of Research in Physical Chemistry & Chemical Physics*, 222(2-3), 257–285.

[Koenigsberger & Prins, 1988] Koenigsberger, P. & Prins, R. (1988). *X-ray Absorption, Principle, Technique, Application of EXAFS, XANES, SEXAFS*. New York: Wiley.

[Kofinger & Dellago, 2010] Kofinger, J. & Dellago, C. (2010). Single-file water as a one-dimensional Ising model. *New Journal of Physics*, 12.

[Kofinger, 2008] Kofinger, J., Hummer, G., & Dellago, C. (2008). Macroscopically ordered water in nanopores.

[Kohl, 2005] Kohl, I., Bachmann, L., Mayer, E., Hallbrucker, A., & Loerting, T. (2005). Water behaviour - Glass transition in hyperquenched water? *Nature*, 435(7041), E1–E1.

[Kresge, 1992] Kresge, C., Leonowicz, M., Roth, W., Vartuli, J., & Beck, J. (1992). Ordered Mesoporous Molecular-Sieves Syntesized By A Liquid-Crystal Template Mechanism. *Nature*, 359, 710–712.

[Kruk, 2000] Kruk, M., Jaroniec, M., Sakamoto, Y., Terasaki, O., Ryoo, R., & Ko, C. H. (2000). Determination of pore size and pore wall structure of MCM-41 by using nitrogen adsorption, transmission electron microscopy, and X-ray diffraction. *Journal of Physical Chemistry B*, 104(2), 292–301.

[Kumar, 2005] Kumar, P., Buldyrev, S. V., Starr, F. W., Giovambattista, N., & Stanley, H. E. (2005). Thermodynamics, structure, and dynamics of water confined between hydrophobic plates. *Physical Review E*, 72(5), 051503.

[Landolt & Boernstein, 1977] Landolt, H. & Boernstein, R. (1977). *Thermodynamische Tabellen.* DÃŒsseldorf: VDI-Verlag.

[Lennard-Jones & Pople, 1951] Lennard-Jones, J. & Pople, J. A. (1951). Molecular Association in Liquids .1. Molecular Association Due to Lone-Pair Electrons. *Proceedings of the Royal Society of London Series a-Mathematical and Physical Sciences*, 205(1081), 155–162.

[Li & Skinner, 2010] Li, F. & Skinner, J. L. (2010). Infrared and Raman line shapes for ice Ih. I. Dilute HOD in H(2)O and D(2)O. *Journal of Chemical Physics*, 132(20).

[Lide, 1992] Lide, D. (1992). *CRC Handbook of Chemistry and Physics*. Boca Raton, Florida: CRC Press, Inc.

[Lindner & Zemb, 2002] Lindner, P. & Zemb, T. (2002). *Neutrons, X-rays and light*. Amsterdam: Elsevier Science B.V.

[Litvan & Mcintosh, 1963] Litvan, G. & Mcintosh, R. (1963). Phase Transitions of Water and Xenon Adsorbed in Porous Vycor Glass. *Canadian Journal of Chemistry-Revue Canadienne De Chimie*, 41(12), 3095.

[Litvan, 1966] Litvan, G. G. (1966). Phase Transitions of Adsorbates .I. Specific Heat and Dimensional Changes of Porous Glass-Water System. *Canadian Journal of Chemistry*, 44(22), 2617.

[Liu, 2007] Liu, D. Z., Zhang, Y., Chen, C. C., Mou, C. Y., Poole, P. H., & Chen, S. H. (2007). Observation of the density minimum in deeply supercooled confined water. *Proceedings of the National Academy of Sciences of the United States of America*, 104(23), 9570–9574.

[Liu, 2008] Liu, D. Z., Zhang, Y., Liu, Y., Wu, J. L., Chen, C. C., Mou, C. Y., & Chen, S. H. (2008). Density measurement of 1-D confined water by small angle neutron scattering method: Pore size and hydration level dependences. *Journal of Physical Chemistry B*, 112(14), 4309–4312.

[Liu, 2006] Liu, E., Dore, J. C., Webber, J. B. W., Khushalani, D., Jahnert, S., Findenegg, G. H., & Hansen, T. (2006). Neutron diffraction and NMR relaxation studies of structural variation and phase transformations for water/ice in SBA-15 silica: I. The over-filled case. *Journal of Physics-Condensed Matter*, 18(44), 10009–10028.

[Liu, 2005] Liu, L., Chen, S. H., Faraone, A., Yen, C. W., & Mou, C. Y. (2005). Pressure dependence of fragile-to-strong transition and a possible second critical point in supercooled confined water. *Physical Review Letters*, 95(11), 117802.

[Liu, 2004] Liu, L., Faraone, A., Mou, C., Yen, C. W., & Chen, S. H. (2004). Slow dynamics of supercooled water confined in nanoporous silica materials. *Journal of Physics-Condensed Matter*, 16(45), S5403–S5436.

[Loerting, 2001] Loerting, T., Salzmann, C., Kohl, I., Mayer, E., & Hallbrucker, A. (2001). A second distinct structural "state" of high-density amorphous ice at 77 K and 1 bar. *Physical Chemistry Chemical Physics*, 3(24), 5355–5357.

[Lombardo, 2008] Lombardo, T. G., Giovambattista, N., & Debenedetti, P. G. (2008). Structural and mechanical properties of glassy water in nanoscale confinemet. *Faraday Discussions*, 141, 359–376.

[Lund-University, 2011] Lund-University (2011). http://www.atom.fysik.lth.se. *Lund-University.*

[Mahoney & Jorgensen, 2000] Mahoney, M. W. & Jorgensen, W. L. (2000). A five-site model for liquid water and the reproduction of the density anomaly by rigid, nonpolarizable potential functions. *Journal of Chemical Physics*, 112(20), 8910–8922.

[Mallamace, 2007a] Mallamace, F., Branca, C., Broccio, M., Corsaro, C., Mou, C. Y., & Chen, S. H. (2007a). The anomalous behavior of the density of water in the range 30K $<$ T $<$ 373K. *Proceedings of the National Academy of Sciences of the United States of America*, 104(47), 18387–18391.

[Mallamace, 2006] Mallamace, F., Broccio, M., Corsaro, C., Faraone, A., Liu, L., Mou, C. Y., & Chen, S. H. (2006). Dynamical properties of confined supercooled water: an NMR study. *Journal of Physics-Condensed Matter*, 18(36), S2285–S2297.

[Mallamace, 2007b] Mallamace, F., Broccio, M., Corsaro, C., Faraone, A., Majolino, D., Venuti, V., Liu, L., Mou, C. Y., & Chen, S. H. (2007b). Evidence of the existence of the low-density liquid phase in supercooled, confined water. *Proceedings of the National Academy of Sciences of the United States of America*, 104(2), 424–428.

[Mallamace, 2008] Mallamace, F., Corsaro, C., Broccio, M., Branca, C., Gonzalez-Segredo, N., Spooren, J., Chen, S. H., & Stanley, H. E. (2008). NMR evidence of a sharp change in a measure of local order in deeply supercooled confined water. *Proceedings of the National Academy of Sciences of the United States of America*, 105(35), 12725–12729.

[Mamontov, 2006] Mamontov, E., Burnham, C. J., Chen, S. H., Moravsky, A. P., Loong, C. K., de Souza, N. R., & Kolesnikov, A. I. (2006). Dynamics of water confined in single- and double-wall carbon nanotubes. *Journal of Chemical Physics*, 124(19).

[Mancinelli, 2010a] Mancinelli, R. (2010a). The effect of confinement on water structure. *Journal of Physics-Condensed Matter*, 22(40), 404213.

[Mancinelli, 2010b] Mancinelli, R., Bruni, F., & Ricci, M. A. (2010b). Controversial Evidence on the Point of Minimum Density in Deeply Supercooled Confined Water. *Journal of Physical Chemistry Letters*, 1(8), 1277–1282.

[Mancinelli, 2011] Mancinelli, R., Bruni, F., & Ricci, M. A. (2011). Structural studies of confined liquids: The case of water confined in MCM-41. *Journal of Molecular Liquids*, 159(1), 42–46.

[Mancinelli, 2009] Mancinelli, R., Imberti, S., Soper, A. K., Liu, K. H., Mou, C. Y., Bruni, F., & Ricci, M. A. (2009). Multiscale Approach to the Structural Study of Water Confined in MCM41. *Journal of Physical Chemistry B*, 113(50), 16169–16177.

[Masic, 2010] Masic, A. (2010). Spectroscopy / Raman / IR, Biological vibrational imaging.

[Masic, 2011] Masic, A. (2011). Personal communication. *7th European Winterschool on Neutron and Synchrotron Radiation.*

[McGraw-Hill, 2005] McGraw-Hill (2005). *Concise Encyclopedia of Science & Technology.* New York: Companies, Inc.

[Merzel & Smith, 2002] Merzel, F. & Smith, J. C. (2002). Is the first hydration shell of lysozyme of higher density than bulk water? *Proceedings of the National Academy of Sciences of the United States of America*, 99(8), 5378–5383.

[Mezei, 1972] Mezei, F. (1972). Neutron Spin-Echo - New Concept in Polarized Thermal-Neutron Techniques. *Zeitschrift Fur Physik*, 255(2), 146.

[Mishima, 1994] Mishima, O. (1994). Reversible 1st-Order Transition between 2 H2o Amorphs at Similar-to-0.2 Gpa and Similar-to-135-K. *Journal of Chemical Physics*, 100(8), 5910–5912.

[Mishima, 1984] Mishima, O., Calvert, L. D., & Whalley, E. (1984). Melting Ice-I at 77-K and 10-Kbar - a New Method of Making Amorphous Solids. *Nature*, 310(5976), 393–395.

[Mishima, 1985] Mishima, O., Calvert, L. D., & Whalley, E. (1985). An Apparently 1st-Order Transition between 2 Amorphous Phases of Ice Induced by Pressure. *Nature*, 314(6006), 76–78.

[Mishima & Stanley, 1998] Mishima, O. & Stanley, H. E. (1998). The relationship between liquid, supercooled and glassy water. *Nature*, 396(6709), 329–335.

[Molinero & Moore, 2009] Molinero, V. & Moore, E. B. (2009). Water Modeled As an Intermediate Element between Carbon and Silicon. *Journal of Physical Chemistry B*, 113(13), 4008–4016.

[Morak, 2012] Morak, R. (2012). Gravimetric sorption isotherm of MCM44, measured on 16.04.2011 at the Montanuniversitaet Leoben.

[Morishige & Kawano, 1999] Morishige, K. & Kawano, K. (1999). Freezing and melting of water in a single cylindrical pore: The pore-size dependence of freezing and melting behavior. *Journal of Chemical Physics*, 110(10), 4867–4872.

[Morishige & Nobuoka, 1997] Morishige, K. & Nobuoka, K. (1997). X-ray diffraction studies of freezing and melting of water confined in a mesoporous adsorbent (MCM-41). *Journal of Chemical Physics*, 107(17), 6965–6969.

[Moynihan, 1997] Moynihan, C. T. (1997). Two species nonideal solution model for amorphous amorphous phase transitions. *Structure and Dynamics of Glasses and Glass Formers*, 455, 411–425.

[Murray, 2005] Murray, B. J., Knopf, D. A., & Bertram, A. K. (2005). The formation of cubic ice under conditions relevant to Earth's atmosphere. *Nature*, 434(7030), 202–205.

[Muter, 2009] Muter, D., Jahnert, S., Dunlop, J. W. C., Findenegg, G. H., & Paris, O. (2009). Pore Structure and Fluid Sorption in Ordered Mesoporous Silica. II. Modeling. *Journal of Physical Chemistry C*, 113(34), 15211–15217.

[NIST, 2011] NIST (2011). Neutron scattering lengths and cross sections.

[Oguni, 2007] Oguni, M., Maruyama, S., Wakabayashi, K., & Nagoe, A. (2007). Glass transitions of ordinary and heavy water within silica-gel nanopores. *Chemistry-an Asian Journal*, 2(4), 514–520.

[Palmqvist, 2003] Palmqvist, A. E. C. (2003). Synthesis of ordered mesoporous materials using surfactant liquid crystals or micellar solutions. *Current Opinion in Colloid & Interface Science*, 8(2), 145–155.

[Paschek, 2005] Paschek, D. (2005). How the liquid-liquid transition affects hydrophobic hydration in deeply supercooled water. *Physical Review Letters*, 94(21), 217802.

[Pecharsky & Zavalij, 2009] Pecharsky, V. & Zavalij, P. (2009). *Fundamentals of Powder Diffraction and Structural Characterization of Material*. New York: Springer Science and Business.

[Pedersen, 1997] Pedersen, J. S. (1997). Analysis of small-angle scattering data from colloids and polymer solutions: modeling and least-squares fitting. *Advances in Colloid and Interface Science*, 70, 171–210.

[Peterlin, 1965] Peterlin, A. (1965). Small Angle Scattering by a 3 Component System. *Makromolekulare Chemie*, 87(Oct), 152.

[Petrenko & Whitworth, 1999] Petrenko, V. & Whitworth, R. (1999). *Physics Of Ice*. Oxford: Oxford University Press.

[Pineri, 2007] Pineri, M., Gebel, G., Davies, R. J., & Diat, O. (2007). Water sorption-desorption in Nafion (R) membranes at low temperature, probed by micro X-ray diffraction. *Journal of Power Sources*, 172(2), 587–596.

[Ponyatovskii, 1994] Ponyatovskii, E. G., Sinand, V. V., & Pozdnyakova, T. A. (1994). 2nd Critical-Point and Low-Temperature Anomalies in the Physical-Properties of Water. *Jetp Letters*, 60(5), 360–364.

[Poole, 1995] Poole, P. H., Grande, T., Sciortino, F., Stanley, H. E., & Angell, C. A. (1995). Amorphous Polymorphism. *Computational Materials Science*, 4(4), 373–382.

[Poole, 2005] Poole, P. H., Saika-Voivod, I., & Sciortino, F. (2005). Density minimum and liquid-liquid phase transition. *Journal of Physics-Condensed Matter*, 17(43), L431–L437.

[Poole, 1992] Poole, P. H., Sciortino, F., Essmann, U., & Stanley, H. E. (1992). Phase-Behavior of Metastable Water. *Nature*, 360(6402), 324–328.

[Poole, 1994] Poole, P. H., Sciortino, F., Grande, T., Stanley, H. E., & Angell, C. A. (1994). Effect of Hydrogen-Bonds on the Thermodynamic Behavior of Liquid Water. *Physical Review Letters*, 73(12), 1632–1635.

[Porod, 1951] Porod, G. (1951). Die Rontgenkleinwinkelstreuung Von Dichtgepackten Kolloiden Systemen .1. *Kolloid-Zeitschrift and Zeitschrift Fur Polymere*, 124(2), 83–114.

[Powles, 1985] Powles, J. G. (1985). On the Validity of the Kelvin Equation. *Journal of Physics a-Mathematical and General*, 18(9), 1551–1560.

[Prass, 2011] Prass, J. (2011). *Verformung hexagonal geordneter, mesoporöser Materialien durch die Wechselwirkung mit Fluiden.* PhD thesis, Humboldt Universität, Fakultät I Mathematik und Naturwissenschaften, Berlin.

[Prass, 2009] Prass, J., Muter, D., Fratzl, P., & Paris, O. (2009). Capillarity-driven deformation of ordered nanoporous silica. *Applied Physics Letters*, 95(8).

[Ratcliffe & Irish, 1982] Ratcliffe, C. I. & Irish, D. E. (1982). Vibrational Spectral Studies of Solutions at Elevated-Temperatures and Pressures .5. Raman Studies of Liquid Water up to 300-Degrees-C. *Journal of Physical Chemistry*, 86(25), 4897–4905.

[Ravikovitch & Neimark, 2001] Ravikovitch, P. I. & Neimark, A. V. (2001). Characterization of micro- and mesoporosity in SBA-15 materials from adsorption data by the NLDFT method. *Journal of Physical Chemistry B*, 105(29), 6817–6823.

[Rennie & Clifford, 1977] Rennie, G. K. & Clifford, J. (1977). Melting of Ice in Porous Solids. *Journal of the Chemical Society-Faraday Transactions I*, 73, 680–689.

[Rice & Sceats, 1981] Rice, S. A. & Sceats, M. G. (1981). A Random Network Model for Water. *Journal of Physical Chemistry*, 85(9), 1108–1119.

[Rigby & Fletcher, 2004] Rigby, S. P. & Fletcher, R. S. (2004). Experimental evidence for pore blocking as the mechanism for nitrogen sorption hysteresis in a mesoporous material. *Journal of Physical Chemistry B*, 108(15), 4690–4695.

[Roentgen, 1892] Roentgen, W. (1892). Ueber die Konstitutions des fluessigen Wassers. *Ann. Phys. Chem.*, 45, 7–91.

[Rouquerol, 1999] Rouquerol, F., Rouquerol, J., & Sing, K. S. W. (1999). *Adsorption by powders & porous solids: principles, methodology and applications.* London: Academic Press.

[Ruppweb, 2012] Ruppweb (2012). http://ruppweb.org/xray/comp/scatfac.htm.

[Ryoo, 2001] Ryoo, R., Joo, S. H., Kruk, M., & Jaroniec, M. (2001). Ordered mesoporous carbons. *Advanced Materials*, 13(9), 677–681.

[Saam & Cole, 1975] Saam, W. F. & Cole, M. W. (1975). Excitations and Thermodynamics for Liquid-Helium Films. *Physical Review B*, 11(3), 1086–1105.

[Sastry, 1996] Sastry, S., Debenedetti, P. G., Sciortino, F., & Stanley, H. E. (1996). Singularity-free interpretation of the thermodynamics of supercooled water. *Physical Review E*, 53(6), 6144–6154.

[Sayari, 1999] Sayari, A., Yang, Y., Kruk, M., & Jaroniec, M. (1999). Expanding the pore size of MCM-41 silicas: Use of amines as expanders in direct synthesis and postsynthesis procedures. *Journal of Physical Chemistry B*, 103(18), 3651–3658.

[Scherer, 1992] Scherer, G. W. (1992). Recent Progress in Drying of Gels. *Journal of Non-Crystalline Solids*, 147, 363–374.

[Schmelzer, 2005] Schmelzer, J. (2005). *Nucleation Theory and Applications*. Rostock: Wiley-VCH Verlag GmbH & Co. KGaA.

[Schoen, 2010] Schoen, M., Paris, O., Gunther, G., Muter, D., Prass, J., & Fratzl, P. (2010). Pore-lattice deformations in ordered mesoporous matrices: experimental studies and theoretical analysis. *Physical Chemistry Chemical Physics*, 12(37), 11267–11279.

[Schreiber, 2002] Schreiber, A. (2002). *Phasenverhalten reiner Stoffe in mesoporösen Silika-Materialien*. PhD thesis, TU Berlin, Fakultät II Mathematik und Naturwissenschaften, Berlin.

[Schreiber, 2001] Schreiber, A., Ketelsen, I., & Findenegg, G. H. (2001). Melting and freezing of water in ordered mesoporous silica materials. *Physical Chemistry Chemical Physics*, 3(7), 1185–1195.

[Schulson, 1999] Schulson, E. M. (1999). The structure and mechanical behavior of ice. *Jom-Journal of the Minerals Metals & Materials Society*, 51(2), 21–27.

[Shin, 2001] Shin, H. J., Ryoo, R., Kruk, M., & Jaroniec, M. (2001). Modification of SBA-15 pore connectivity by high-temperature calcination investigated by carbon inverse replication. *Chemical Communications*, (4), 349–350.

[Shull & Smart, 1949] Shull, C. G. & Smart, J. S. (1949). Detection of Antiferromagnetism by Neutron Diffraction. *Physical Review*, 76(8), 1256–1257.

[Sing, 1985] Sing, K. S. W., Everett, D. H., Haul, R. A. W., Moscou, L., Pierotti, R. A., Rouquerol, J., & Siemieniewska, T. (1985). Reporting Physisorption Data for Gas Solid Systems with Special Reference to the Determination of Surface-Area and Porosity (Recommendations 1984). *Pure and Applied Chemistry*, 57(4), 603–619.

[Sivakumar, 1978a] Sivakumar, T. C., Chew, H. A. M., & Johari, G. P. (1978a). Effect of Pressure on Raman-Spectrum of Ice. *Nature*, 275(5680), 524–525.

[Sivakumar, 1978b] Sivakumar, T. C., Rice, S. A., & Sceats, M. G. (1978b). Raman-Spectroscopic Studies of Oh Stretching Region of Low-Density Amorphous Solid Water and of Polycrystalline Ice Ih. *Journal of Chemical Physics*, 69(8), 3468–3476.

[Sivakumar, 1977] Sivakumar, T. C., Schuh, D., Sceats, M. G., & Rice, S. A. (1977). 2500-4000 Cm-1 Raman and Ir-Spectra of Low-Density Amorphous Solid Water and of Polycrystalline Ice-1. *Chemical Physics Letters*, 48(2), 212–218.

[Soper, 2008] Soper, A. K. (2008). Structural transformations in amorphous ice and supercooled water and their relevance to the phase diagram of water. *Molecular Physics*, 106(16-18), 2053–2076.

[Sorenson, 2000] Sorenson, J. M., Hura, G., Glaeser, R. M., & Head-Gordon, T. (2000). What can x-ray scattering tell us about the radial distribution functions of water? *Journal of Chemical Physics*, 113(20), 9149–9161.

[Speedy, 1982] Speedy, R. J. (1982). Stability-Limit Conjecture - an Interpretation of the Properties of Water. *Journal of Physical Chemistry*, 86(6), 982–991.

[Stanley, 2011] Stanley, H. E., Buldyrev, S. V., Kumar, P., Mallamace, F., Mazza, M. G., Stokely, K., Xu, L., & Franzese, G. (2011). Water in nanoconfined and biological environments (Plenary Talk, Ngai-Ruocco 2009 IDMRCS Conf.). *Journal of Non-Crystalline Solids*, 357(2), 629–640.

[Stanley, 2009] Stanley, H. E., Kumar, P., Han, S., Mazza, M. G., Stokely, K., Buldyrev, S. V., Franzese, G., Mallamace, F., & Xu, L. (2009). Heterogeneities in confined water and protein hydration water. *Journal of Physics-Condensed Matter*, 21(50), 504105.

[Stanley & Teixeira, 1980] Stanley, H. E. & Teixeira, J. (1980). Interpretation of the Unusual Behavior of H2o and D2o at Low-Temperatures - Tests of a Percolation Model. *Journal of Chemical Physics*, 73(7), 3404–3422.

[Stapleton, 1988] Stapleton, M. R., Tildesley, D. J., Sluckin, T. J., & Quirke, N. (1988). Computer-Simulation of Polydisperse Liquids with Density-Dependent and Temperature-Dependent Distributions. *Journal of Physical Chemistry*, 92(16), 4788–4796.

[Starr, 2003] Starr, F. W., Angell, C. A., & Stanley, H. E. (2003). Prediction of entropy and dynamic properties of water below the homogeneous nucleation temperature. *Physica a-Statistical Mechanics and Its Applications*, 323, 51–66.

[Stillinger & Rahman, 1974] Stillinger, F. H. & Rahman, A. (1974). Molecular-Dynamics Study of Liquid Water under High Compression. *Journal of Chemical Physics*, 61(12), 4973–4980.

[Stuart & Klages, 1992] Stuart, H. & Klages, G. (1992). *Kurzes Lehrbuch der Physik*. Berlin: Springer Verlag.

[Stuhrmann, 1985] Stuhrmann, H. B. (1985). Resonance Scattering in Macromolecular Structure Research. *Advances in Polymer Science*, 67, 123–163.

[Sun, 2009] Sun, Q. (2009). The Raman OH stretching bands of liquid water. *Vibrational Spectroscopy*, 51(2), 213–217.

[Sun & Zheng, 2009] Sun, Q. & Zheng, H. F. (2009). Raman OH stretching vibration of ice I-h. *Progress in Natural Science*, 19(11), 1651–1654.

[Svergun, 1998] Svergun, D. I., Richard, S., Koch, M. H. J., Sayers, Z., Kuprin, S., & Zaccai, G. (1998). Protein hydration in solution: Experimental observation by x-ray and neutron scattering. *Proceedings of the National Academy of Sciences of the United States of America*, 95(5), 2267–2272.

[Swenson, 2001] Swenson, J., Bergman, R., & Longeville, S. (2001). A neutron spin-echo study of confined water. *Journal of Chemical Physics*, 115(24), 11299–11305.

[Swenson, 2006] Swenson, J., Jansson, H., & Bergman, R. (2006). Relaxation processes in supercooled confined water and implications for protein dynamics. *Physical Review Letters*, 96(24).

[Swenson, 2005] Swenson, J., Jansson, H., Howells, W. S., & Longeville, S. (2005). Dynamics of water in a molecular sieve by quasielastic neutron scattering. *Journal of Chemical Physics*, 122(8).

[Taschin, 2010] Taschin, A., Cucini, R., Bartolini, P., & Torre, R. (2010). Temperature of maximum density of water in hydrophilic confinement measured by transient grating spectroscopy. *Epl*, 92(2), 26005.

[Tejero & Baus, 1998] Tejero, C. F. & Baus, M. (1998). Liquid polymorphism of simple fluids within a van der Waals theory. *Physical Review E*, 57(4), 4821–4823.

[Thommes, 2006] Thommes, M., Smarsly, B., Groenewolt, M., Ravikovitch, P. I., & Neimark, A. V. (2006). Adsorption hysteresis of nitrogen and argon in pore networks and characterization of novel micro- and mesoporous silicas. *Langmuir*, 22(2), 756–764.

[Tipler, 1994] Tipler, P. (1994). *Physik*. Berlin: Spektrum Akademischer Verlag.

[Tombari, 1999] Tombari, E., Ferrari, C., & Salvetti, G. (1999). Heat capacity anomaly in a large sample of supercooled water. *Chemical Physics Letters*, 300(5-6), 749–751.

[Tse, 1992] Tse, J. S. (1992). Mechanical Instability in Ice Ih - a Mechanism for Pressure-Induced Amorphization. *Journal of Chemical Physics*, 96(7), 5482–5487.

[Velikov, 2001] Velikov, V., Borick, S., & Angell, C. A. (2001). The glass transition of water, based on hyperquenching experiments. *Science*, 294(5550), 2335–2338.

[Venkatesh, 1975] Venkatesh, C. G., Rice, S. A., & Bates, J. B. (1975). Raman Spectral Study of Amorphous Solid Water. *Journal of Chemical Physics*, 63(3), 1065–1071.

[Volmer & Weber, 1926] Volmer, M. & Weber, A. (1926). Germ-formation in oversaturated figures. *Zeitschrift Fur Physikalische Chemie–Stochiometrie Und Verwandtschaftslehre*, 119(3/4), 277–301.

[Wallacher, 2005a] Wallacher, D. (2005a). *Porenkondensierte Materiein der Naehe des Fest-Fluessig-Dampf-Tripelpunktes*. PhD thesis, Universitaet des Saarlandes, Saarbruecken.

[Wallacher, 2005b] Wallacher, D., Soprunyuk, V. P., Kityk, A. V., Huber, P., & Knorr, K. (2005b). Capillary sublimation of Ar in mesoporous glass. *Physical Review B*, 71(5).

[Walrafen, 1964] Walrafen, G. E. (1964). Raman Spectral Studies of Water Structure. *Journal of Chemical Physics*, 40(11), 3249.

[Walrafen, 1967] Walrafen, G. E. (1967). Raman Spectral Studies of Effects of Temperature on Water Structure. *Journal of Chemical Physics*, 47(1), 114.

[Walrafen, 1986] Walrafen, G. E., Hokmabadi, M. S., & Yang, W. H. (1986). Raman Isosbestic Points from Liquid Water. *Journal of Chemical Physics*, 85(12), 6964–6969.

[Webber, 2010] Webber, J. B. W. (2010). Studies of nano-structured liquids in confined geometries and at surfaces. *Progress in Nuclear Magnetic Resonance Spectroscopy*, 56(1), 78–93.

[Webber, 2007] Webber, J. B. W., Dore, J. C., Strange, J. H., Anderson, R., & Tohidi, B. (2007). Plastic ice in confined geometry: the evidence from neutron diffraction and NMR relaxation. *Journal of Physics-Condensed Matter*, 19(41), 415117.

[Webber, 2008] Webber, J. B. W., Strange, J. H., Bland, P. A., Anderson, R., & Tohidi, B. (2008). Dynamics at Surfaces : Probing the dynamics of polar and a-polar liquids at silica and vapour surfaces. *American Institute of Physics (AIP) Conference Proceedings Series*, 51(MAGNETIC RESONANCE IN POROUS MEDIA: Proceedings of the 9th International Bologna Conference on Magnetic Resonance in Porous Media (MRPM9).), 1081.

[Weinwurm & Dellago, 2011] Weinwurm, M. & Dellago, C. (2011). Vibrational Spectroscopy of Water in Narrow Nanopores. *Journal of Physical Chemistry B*, 115(18), 5268–5277.

[Xia, 2006] Xia, Y. D., Dosseh, G., Morineau, D., & Alba-Simionesco, C. (2006). Phase diagram and glass transition of confined benzene. *Journal of Physical Chemistry B*, 110(39), 19735–19744.

[Xu, 2005] Xu, L. M., Kumar, P., Buldyrev, S. V., Chen, S. H., Poole, P. H., Sciortino, F., & Stanley, H. E. (2005). Relation between the Widom line and the dynamic crossover in systems with a liquid-liquid phase transition. *Proceedings of the National Academy of Sciences of the United States of America*, 102(46), 16558–16562.

[Xu, 2009] Xu, L. M., Mallamace, F., Yan, Z. Y., Starr, F. W., Buldyrev, S. V., & Stanley, H. E. (2009). Appearance of a fractional Stokes-Einstein relation in water and a structural interpretation of its onset. *Nature Physics*, 5(8), 565–569.

[Yamaguchi, 2006] Yamaguchi, T., Hashi, H., & Kittaka, S. (2006). X-ray diffraction study of water confined in activated carbon pores over a temperature range of 228-298 K. *Journal of Molecular Liquids*, 129(1-2), 57–62.

[Yoshida, 2008] Yoshida, K., Yamaguchi, T., Kittaka, S., Bellissent-Funel, M. C., & Fouquet, P. (2008). Thermodynamic, structural, and dynamic properties of supercooled water confined in mesoporous MCM-41 studied with calorimetric, neutron diffraction, and neutron spin echo measurements. *Journal of Chemical Physics*, 129(5).

[Zanotti, 2005] Zanotti, J. M., Bellissent-Funel, M. C., & Chen, S. H. (2005). Experimental evidence of a liquid-liquid transition in interfacial water. *Europhysics Letters*, 71(1), 91–97.

[Zhang, 2009] Zhang, Y., Chen, S. H., Liu, K. H., Lagi, M., Liu, D., Littrell, K. C., & Mou, C. Y. (2009). Absence of the Density Minimum of Supercooled Water in Hydrophobic Confinement. *Journal of Physical Chemistry B*, 113(15), 5007–5010.

[Zhao, 1998] Zhao, D. Y., Feng, J. L., Huo, Q. S., Melosh, N., Fredrickson, G. H., Chmelka, B. F., & Stucky, G. D. (1998). Triblock copolymer syntheses of mesoporous silica with periodic 50 to 300 angstrom pores. *Science*, 279, 548–552.

[Zickler, 2006] Zickler, G. A., Jahnert, S., Wagermaier, W., Funari, S. S., Findenegg, G. H., & Paris, O. (2006). Physisorbed films in periodic mesoporous silica studied by in situ synchrotron small-angle diffraction. *Physical Review B*, 73(18), 184109.

[Zwick & Landa, 1994] Zwick, A. & Landa, G. (1994). Low Wave-Number Raman-Scattering in Viscous-Liquids. *Journal of Raman Spectroscopy*, 25(11), 849–854.

[Zyubin, 2002] Zyubin, A. S., Mebel, A. M., Lin, S. H., & Glinka, Y. D. (2002). Photoluminescence of silanone and dioxasilyrane groups in silicon oxides: A theoretical study. *Journal of Chemical Physics*, 116(22), 9889–9896–.